MUON PAIRS AND ASSOCIATED HADRONS IN PION-NUCLEON INTERACTIONS

JAN STEPHEN WIEJAK

A Thesis submitted for the Degree of
Doctor of Philosophy in the University of London
and for the Diploma of Membership of Imperial College

Department of Physics
Imperial College, London

July 1981

ABSTRACT

Muon Pairs and Associated Hadrons in Pion-Nucleon Interactions

This thesis is an account of the WA11 experiment performed at the CERN SPS in order to study the production mechanisms of muon pairs and associated hadrons. Pion-nucleon interactions, with beam momenta between 175 and 197.5 GeV/c, were detected in a large acceptance magnetic spectrometer. The apparatus and triggers and their performance are described.

The kinematical distributions of the muon pairs are presented and discussed in the context of parton models. A comparison is made between the production of the muon pairs from ψ decay and those of the continuum. Results on the multiplicity, kinematical distributions and quantum numbers of the associated hadrons are also used to provide information on the production mechanisms. A study of the transverse momentum structure of the events is used to investigate the origin of the transverse momentum of the muon pairs.

PREFACE

The WA11 Experiment was performed by a collaboration of physicists from Saclay, Imperial College, Indiana and Southampton Universities. Data taking began in September 1977 and ended in June 1980. The author became a research student in the High Energy Nuclear Physics group at Imperial College in October 1978, and then worked in the WA11 Collaboration at CERN from February 1979, returning to Imperial College in April 1980 to analyse the data.

Chapter 1 of this thesis contains a review of the physics involved in the experiment. In Chapter 2, the WA11 apparatus is described, although obviously the author was not involved in its planning or setting up. Chapter 3 contains a brief description of the data reduction procedure which was the work of the Saclay group and CERN. The author's contribution starts with the work on the apparatus and trigger performance discussed in chapter 3. The analysis discussed in chapters 4-6 is entirely the work of the author (except where otherwise stated in the text).

During Summer 1979, the author was also responsible for tests of an electromagnetic calorimeter in an electron beam at CERN, and the subsequent analysis and writing of a report. This work, which was done in preparation for the NA14 photon experiment at CERN, is not described in this thesis.

CONTENTS

CHAPTER 1

REVIEW OF LEPTON PAIR PRODUCTION

1.0 INTRODUCTION

There are good theoretical reasons for studying the production of massive lepton pairs in high energy collisions of hadrons:

(i) Information on the constituents of the hadrons and their interactions can be extracted, complementing other approaches such as deep inelastic lepton scattering.

(ii) The ψ ($c\bar{c}$ bound state) was discovered [1.1] in $pN \to \psi \to e^+e^-$, and the Υ ($b\bar{b}$ bound state) [1.2] in $pN \to \Upsilon \to \mu^+\mu^-$. Bound states of new heavier quarks may similarly be observed at higher energies. Such an observation would provide a useful starting point for a further investigation of the resonance using e^+e^- machines.

(iii) The neutral vector boson Z^o of the weak interaction should be observed in the lepton pair mass spectrum. Also, the production at higher energies of the charged vector bosons $W^{\pm}$ can be estimated from lepton pair data.

On the experimental side, the leptons e, μ have properties which allow them to be seen against a large hadronic background.

Models and existing data for the lepton pair continuum and the ψ and Υ resonances are discussed in this chapter.

1.1 LEPTON PAIR CONTINUUM

1.1.1 Drell-Yan Parton Model

To explain the observed production of massive lepton pairs in high energy collisions of hadrons [1.3], Drell and Yan proposed a parton model approach [1.4]. In their model, when two hadrons h_1, h_2 collide, a quark constituent from one annihilates with a corresponding antiquark from the other to produce a virtual photon, γ^*, of mass m and four-momentum Q^μ, which subsequently decays into a lepton pair $\ell^+\ell^-$, as illustrated in fig 1.1. The probability that a quark (or antiquark) has a longitudinal momentum fraction x of its parent hadron's momentum, is expressed as a function $q(x)$ (or $\bar{q}(x)$). These parton probability distribution functions (PDF) $q(x)$, $\bar{q}(x)$, were assumed to be the same as those derived via a similar parton model approach from deep inelastic lepton scattering experiments, and to be similarly independent of Q^2, the large momentum scale involved in the parton subprocess. (This property of the PDF was known as "scaling"). For the model to apply, the kinematic region must be such that the partons involved in the annihilation are instantaneously free; that is, during the interaction, their binding inside the hadrons can be neglected.

In the overall centre of mass (CM) frame , the hadron four-momenta can be written:

$$h_1^\mu = (\tfrac{1}{2}\sqrt{s},\ \tfrac{1}{2}\sqrt{s},\ 0,\ 0), \quad h_2^\mu = (\tfrac{1}{2}\sqrt{s},\ -\tfrac{1}{2}\sqrt{s},\ 0,\ 0) \qquad (1.1)$$

having neglected the masses of the hadrons compared to the total CM energy $\sqrt{s}$. In this frame, if the partons have negligible transverse momentum and are massless, and have longitudinal momentum fractions x_1, x_2, their four-momenta are:

$$\bar{q}^{\mu} = (\tfrac{1}{2}\sqrt{s}\ x_1,\ \tfrac{1}{2}\sqrt{s}\ x_1,\ 0,\ 0), \quad q^{\mu} = (\tfrac{1}{2}\sqrt{s}\ x_2,\ -\tfrac{1}{2}\sqrt{s}\ x_2, 0, 0) \qquad (1.2)$$

The mass m and longitudinal momentum p_L of the lepton pair in this frame are given by:

$$m^2 = x_1\ x_2\ s, \quad p_L = \tfrac{1}{2}\sqrt{s}\ (x_1 - x_2) \qquad (1.3)$$

It is convenient to use the dimensionless variables x_L and τ defined by:

$$x_L \equiv \frac{p_L}{\frac{1}{2}\sqrt{s}}\ (= x_1 - x_2), \quad \tau \equiv \frac{m^2}{s}\ (= x_1\ x_2) \qquad (1.4)$$

The parton variables can be expressed in terms of the lepton pair quantities as:

$$x_{1,2} = \tfrac{1}{2}(\sqrt{x_L^2 + 4\tau} \pm x_L) \qquad (1.5)$$

In the region m^2, s large, and m^2/s finite, where the masses of the partons and hadrons and the transverse momenta of the partons can be neglected, and the partons have large values of x, the model predicts:

$$\frac{d^2\sigma(h_1h_2 \to \ell^+\ell^- + x)}{dx_1dx_2} = \sum_i \{q_i(x_1)\bar{q}_i(x_2) + \bar{q}_i(x_1)q_i(x_2)\}\ \frac{4\pi\alpha^2}{3m^2}\ e_i^2\ \frac{1}{N_c} \qquad (1.6)$$

The sum is over the different quark flavours i = u, d, s, ..., and $\frac{4\pi\alpha^2}{3m^2}\ e_i^2$ is just the total cross-section for the electromagnetic process of quark-antiquark annihilation into a lepton pair of mass m, where e_i is the quark charge and α the electromagnetic coupling strength. The factor $\frac{1}{N_c}$, where N_c is the number of quark colours, occurs because the quark and antiquark must be able to annihilate to produce a virtual photon, which of course carries no colour. From equation 1.6 (setting $N_c = 3$), two other useful forms of differential cross-section can be obtained:

$$\frac{d^2\sigma}{dmdx_L} = \frac{8\pi\alpha^2}{9m^3} \sum_i e_i^2 \frac{x_1 x_2}{x_1+x_2} \{q_i(x_1)\bar{q}_i(x_2)+\bar{q}_i(x_1)q_i(x_2)\} \quad (1.7)$$

$$m^3 \frac{d\sigma}{dm} = \frac{8\pi\alpha^2}{9} \sum_i e_i^2 \iint dx_1 dx_2 \; x_1 x_2 \{q_i(x_1)\bar{q}_i(x_2)+\bar{q}_i(x_1)q_i(x_2)\}\delta(x_1 x_2 - \frac{m^2}{s}) \quad (1.8)$$

1.2 PREDICTIONS AND DATA

To assess the Drell-Yan (DY) parton model, its predictions are compared with the data which existed from the following lepton pair production (LPP) experiments:

(i) CERN-College de France-Orsay-Saclay (NA3) [1.5]
150, 200, 280 GeV/c π, K, p beams H_2, Pt targets

(ii) Chicago-Illinois-Princeton (CIP) [1.6]
225 GeV/c π, K, p beams C, Cu, W targets

(iii) Birmingham-CERN-Ecole Polytechnique (Ω) [1.7]
39.5 GeV/c π, K, p beams W target

(iv) Saclay-Imperial College-Indiana-Southampton (WA11) [1.8]
150, 175 GeV/c π beams Be target.

Emphasis is given to those aspects which will not be discussed later in the chapters dealing with the results of the analysis.

1.2.1 Scaling

If the parton probability distribution functions (PDF) depend only on x_1, x_2, then the differential cross-section in equation 1.8 depends only on the variable $\tau(\equiv \frac{m^2}{s})$, that is:

$$m^3 \frac{d\sigma}{dm} = F(\tau) \qquad (1.9)$$

To test this scaling prediction, data are needed at several different values of $\sqrt{s}$, and for ranges of m which exclude the ψ and Υ resonances, where other processes may be involved.

The prediction is verified by comparing NA3 data at 150, 200, 280 GeV/c, to within the level of the experimental accuracy of $\pm$ 15%. It is also supported by a comparison of the WA11 data at 150, 175 GeV/c. Further, on a plot of $m^3 \frac{d\sigma}{dm}$ vs τ, the data of these two experiments agree well with each other, over this rather limited range of s. However, the Ω data at 39.5 GeV/c are 20% higher (although their errors are consistent with this discrepancy). Also, the CIP data at 225 GeV/c are rather lower than the NA3 and WA11 data. It should be noted that such a comparison between experiments using different targets and working in different kinematical regions is rather difficult.

1.2.2 Beam Particle Dependence

The ratios of cross-sections for different beams and targets are predicted simply in terms of the charges and PDF of the annihilating quark and antiquark constituents, as seen from equation 1.6. For the ratio of lepton pair production (LPP) by π^+ to that by π^- at large enough $\frac{m^2}{s}$ (= $x_1 x_2$), where annihilation of a valence antiquark from the pion beam and a valence quark from the isoscalar target N dominates, the prediction is:

$$\frac{\sigma(\pi^+ N \to \ell^+ \ell^-)}{\sigma(\pi^- N \to \ell^+ \ell^-)} = \frac{e_d^{\,2}\ \bar{d}^{\pi^+}(x_1) d^N(x_2)}{e_u^{\,2}\ \bar{u}^{\pi^-}(x_1) u^N(x_2)} = \frac{1}{4} \qquad (1.10)$$

where $e_d^{\,2}$, $\bar{d}^{\pi^+}(x_1)$, $d^N(x_2)$ are the charge squared and PDF of the $\bar{d}$

antiquark in the π^+ and d quark in N,respectively. (The relations $\bar{d}^{\pi^+}(x_1) = \bar{u}^{\pi^-}(x_1)$, $d^N(x_2) = u^N(x_2)$, which follow from isospin invariance, have been used). A rapid decrease in the ratio $\frac{\sigma(pN \to \ell^+\bar{\ell})}{\sigma(\pi N \to \ell^+\bar{\ell})}$ is also expected as $\frac{m^2}{s}$ $(= x_1 x_2)$ increases, since the pion has a valence antiquark,while an antiquark from the proton must come from the much smaller sea contribution.

Both these fundamental predictions of the DY parton model are well supported by the NA3, CIP, Ω data. This is the most important piece of evidence in favour of the electromagnetic nature of the subprocess at the centre of the DY mechanism.

1.2.3 Target 'A' Dependence

Since the model is based on the incoherent interaction of the hard partons within the incident hadrons, the cross-section should vary linearly with A, the number of nucleons within a nucleus of the target. Thus $\sigma \sim A^{\alpha}$ with $\alpha \simeq 1$ is expected, in contrast to soft hadronic reactions where $\alpha \simeq 2/3$. The NA3 data using H_2 and Pt targets simultaneously support this prediction very well. However, the CIP data with C,Cu, W targets give $\alpha = 1.12 \pm .05$. This deviation from linearity leads to the discrepancy between the CIP data and the NA3 and WA11 data as discussed in section 1.2.1, where comparison is made between cross-sections per nucleon,calculated via the A dependence, from cross-sections measured on heavy nuclei.

1.2.4 Transverse Momentum

Using the model, the only source of transverse momentum p_T, for the

lepton pair is the intrinsic transverse momentum k_T of the annihilating partons, associated with their confinement within the parent hadron. The average value of the transverse momentum of particles produced in the bulk of ordinary high energy hadron collisions is≈350MeV/c, and this value is used as a simple estimate of $\langle k_T \rangle$. The uncertainty principle, applied to the size of a hadron gives a similar estimate. These estimates, however, are not necessarily appropriate to hard-scattering processes.

The data give a value of $\langle p_T \rangle$ which increases with lepton pair mass up to a mass of≈4GeV/c^2, reaching a plateau of 1.0GeV/c for 200GeV/c proton collisions and 1.2GeV/c for 200GeV/c pion collisions, and these plateau values increase approximately linearly with $\sqrt{s}$. The model,including intrinsic transverse momentum,appears not to account naturally for these large values or for their energy dependence.

1.2.5 Angular Distribution

When the on-shell spin$\frac{1}{2}$ quark and antiquark of mass m_q annihilate via a virtual photon to produce a lepton pair of invariant mass m, the polar angle θ distribution of a lepton in the quark-antiquark CM frame (which is also the lepton pair CM frame) has the form, given by quantum electrodynamics:

$$\frac{d\sigma}{d(\cos\theta)} \sim 1 + \lambda\cos^2\theta, \quad \lambda = \frac{1 - 4m_q^2/m^2}{1 + 4m_q^2/m^2} \qquad (1.11)$$

having neglected the lepton mass. Assuming the quarks which contribute have $m_q \ll m$, gives $\lambda \simeq 1$. Also, the azimuthal angle φ distribution of a lepton around the annihilation axis is expected to be flat.

1.2.6 Parton Probability Distribution Functions

Lepton pair production (LPP) can be used to determine the parton PDF of hadrons (for example π, K) which are inaccessible otherwise, essentially by analysing the data in terms of the DY differential cross-section $\frac{d^2\sigma}{dx_1 dx_2}$. For example, the NA3 result for a fit of the shape of the PDF of the valence quarks in pions is:

$$x_1 q^{\pi}_{valence}(x_1) \sim x_1^{0.40\pm.06} (1-x_1)^{0.90\pm.06}$$

This is obtained by a subtraction of the π^+ data from the π^- data, which removes any effect of the sea quarks in the pion. The normalisation is then obtained by requiring $\int_0^1 q^{\pi}_{valence}(x_1)\, dx_1 = 1$; that is, exactly one valence quark in the pion (and one valence antiquark). Similar shapes are found by the other experiments. Having found the valence quark contribution, NA3 then extract the sea component and find $x_1 q^{\pi}_{sea}(x_1) \sim (1-x_1)^{4.4\pm1.9}$. The nucleon PDF are also measured, and are similar in shape to those obtained independently in deep inelastic lepton scattering experiments.

1.2.7 Absolute Normalisation

The differential cross-sections for LPP by the DY mechanism (equations 1.6-1.8) are determined in shape and amplitude once the parton PDF are known. For the case of pN and $\bar{p}$N collisions, these parton PDF are measured in deep inelastic lepton scattering (DILS) as well as in LPP. The NA3, WA11, Ω experiments all find that the data fall above the expected value by a factor between two and three. NA3 investigate this factor further, eliminating any possible purely hadronic process which would contribute equally to π^+ and π^- cross-sections, by using the difference between these two sets of data.

They also eliminate the possibility of having calculated with the wrong A dependence, by using their small amount of data on a H_2 target.

1.2.8 Associated Hadrons

The DY process involves the annihilation of a quark from one hadron with an antiquark from the other. The remaining constituents of the initial hadrons continue to travel essentially along the original beam and target directions, but must somehow rearrange themselves into the hadrons observed in the final state. For example, in collisions of a π^- beam with a nucleon target, a $\bar{u}$ valence antiquark is removed from the π^-, and the final-state hadrons travelling along the original beam direction should reflect this fact. Additionally, the transverse momentum of the lepton pair must be balanced by the other final state particles, whose configuration may thus give some hint as to the origin of such transverse momentum.

Thus, a study of the associated hadrons could give important information on the process of LPP, complementing that obtained directly from the lepton pair. The NA3, CIP, Ω experiments are unable to investigate this important aspect of LPP since they do not detect the associated hadrons in the final state. The WA11 experiment, on the other hand, does have the ability to perform this analysis of associated hadrons, and much of the work described later in this thesis is concerned with this previously unexplored approach to the subject.

1.3 BEYOND THE DRELL-YAN MODEL

As discussed above, although the DY parton model successfully predicts many features of the data on LPP, it has several problems, mainly those of the transverse momentum of the lepton pair and the absolute normalisation of the cross-section. Some attempts to obtain a further understanding of LPP in high energy collisions of hadrons have been made [1.9 - 1.11] by extending the DY model in the framework of quantum chromodynamics (QCD).

1.3.1 Higher Order Terms

Quantum chromodynamics (QCD) is an attempt to describe the interaction of the hadronic constituents, quarks and gluons, in terms of a gauge theory. Each parton subprocess is considered as a term in a perturbation expansion involving the lagrangian which describes the interaction. The annihilation subprocess of the DY parton model (fig 1.1) is considered as the term of zeroth order in α_s, the strength of the coupling between quarks and gluons. Some parton subprocesses involving a gluon, which lead to contributions of higher order in α_s, are illustrated in figs 1.2 - 1.4, (the leptons are also shown).

This approach follows the one applied to deep inelastic electron and muon scattering, which also involve a massive virtual photon of four momentum Q^μ, but which is spacelike; that is, $Q^2 < 0$. In this QCD approach to deep inelastic lepton scattering (DILS), as well as the subprocess of the original parton model description illustrated in fig 1.5, higher order terms are also included such as those illustrated in figs 1.6 - 1.8, (the leptons are also shown).

Considering all the contributions of first order in α_s, there are "leading logarithmic terms" of the form $\sim \alpha_s \ln Q^2/m_q^2$, associated with divergences as the quark mass $m_q \to 0$. These leading logarithmic terms can be absorbed into the parton PDF, which then become Q^2 dependent ("scaling violation"), but the original form of the parton model description is restored. This result holds to all orders of α_s.

Returning to the case of LPP, a similar result holds, as might be expected from the similarity between the diagrams for LPP (figs 1.1 - 1.4) and for DILS (figs 1.5 - 1.8). In this case, the leading logarithmic terms can be absorbed, part into the parton PDF of each hadron, and the original form of the DY parton model description is restored, but with PDF which are now $Q^2(=m^2)$ dependent, and moreover are exactly the same as in DILS.

1.3.2 Reassessment of Predictions

The extension of the DY parton model in the framework of QCD leads to modifications of its predictions. As discussed above, the parton PDF become $Q^2(=m^2)$ dependent and so equation 1.9 is replaced by:

$$m^3 \frac{d\sigma}{dm} = F(\tau, m^2) \qquad (1.12)$$

The parton PDF $q(x, Q^2)$ measured in DILS show only slight Q^2 dependence near $x \simeq 0.2$. For the ranges of τ and Q^2 over which scaling is so far tested in LPP, the scaling violations are expected to be small, and would be smaller than the uncertainties in the present data.

The most appealing modification is that transverse momentum for

the lepton pair arises naturally from the parton subprocesses of figs 1.2, 1.3. In addition to any contribution from the intrinsic k_T of the partons, these first order terms give:

$$\langle p_T^2 \rangle_{QCD} \sim \alpha_s \cdot s \cdot f(\frac{m^2}{s}) \qquad (1.13)$$

which follows the observed energy dependence of the $\langle p_T^2 \rangle$, but does not account entirely for its magnitude [1.12], large values of $\langle k_T \rangle$ still being required.

Having absorbed the leading logarithmic terms into the parton PDF, there are still "next-to-leading logarithmic terms" of the form $\sim \alpha_s \cdot C$, where C is independent of Q^2, which are thus down by a factor $\ln Q^2$. These contributions are different for DILS and for LPP because in DILS $Q^2 < 0$ and the massive γ^* is in the initial state of the parton subprocess, while in LPP $Q^2 > 0$ and the massive γ^* is in the final state, and this difference is numerically large for present values of Q^2 and s. As a result, the LPP cross-section $m^3 \frac{d\sigma}{dm}$ is a factor $K \simeq 2$ larger than that simply calculated using the DY prescription with Q^2 dependent parton PDF. This factor K depends on τ , but is almost constant over the present range of τ covered. Of course, when trying to use a perturbation expansion, it is rather unsatisfactory that the first order terms produce a result as large as the zeroth order, especially as the effect of even higher order terms is still not clear.

In the subprocesses of figs 1.2, 1.3, the transverse momentum of the lepton pair is balanced by a recoiling gluon or quark, whose subsequent evolution may produce an observable "jet" of hadrons in the final state.

1.4 ψ AND Υ RESONANCES

1.4.1 Parton Models

Present models [1.13 - 1.19] for the production of the ψ and Υ resonances in high energy collisions of hadrons, attempt to describe the process in terms of an interaction between constituent partons, one from each of the hadrons. The resonance can then decay, via its coupling to a virtual photon, into a lepton pair. This approach is similar to that of the DY parton model for the lepton pair continuum, and so the kinematics and differential cross-section formulae look similar, although the mass of the lepton pair, which now results from the $\psi(\Upsilon)$ decay, is fixed. The resulting differential cross-section for the x_L-distribution of the $\psi(\Upsilon)$ has the form:

$$\frac{d\sigma(h_1 h_2 \to \psi(\Upsilon)+x)}{dx_L} \sim \frac{1}{m^2} \cdot \frac{g^2}{4\pi} \sum_i \frac{x_1 x_2}{x_1+x_2} \{q_i(x_1) q_i(x_2)\} \quad (1.14)$$

where g is the strength of the coupling of the partons to the $\psi(\Upsilon)$, and $q_i(x_j)$ is the PDF for each type of parton i (quark or gluon) within the hadron h_j which contributes to the process. Other notation is the same as for the DY model (section 1.1.1).

The various parton models are described below with reference to ψ ($c\bar{c}$ bound state) production, but can be extended [1.18, 1.19] to cover the heavier Υ ($b\bar{b}$ bound state) production.

1.4.2 Charmed Quark Model

An obvious choice for the partons taking part in the process, is the charmed c quarks in the sea of each hadron, which fuse to form a ψ, as illustrated in fig 1.9. In this model [1.13, 1.14, 1.16]

the coupling strength $\frac{g^2(c\bar{c}\ \psi)}{4\pi}$ is expected to be large (of order 1, from a comparison with coupling of ρ to light quarks), but the measured PDF for c quarks in the sea is very small and falls off very rapidly like a large power of (1-x) as $x \to 1$. In the $c\bar{c}$ fusion mechanism the remnants of each hadron would contain non-zero charm quantum numbers, and it might be expected that associated charmed particles (e.g. D-mesons) are produced, unless the final state rearrangement which produces the observed hadrons also neutralises this free charm in some way.

1.4.3 Valence Quark Models

In these models, the light valence quarks u, d produce a ψ either directly [1.13, 1.14, 1.17], as in fig 1.10, or via an intermediate χ (charge conjugation C = +1) state [1.18] which subsequently decays to $\psi\gamma$, as in fig 1.11. Since the ψ and χ are colourless, charge conjugation C = -1, +1 states, respectively, the couplings $g(q\bar{q}\ \psi)$ and $g(q\bar{q}\ \chi)$, are presumably provided by three gluons and two gluons respectively and are thus much smaller than in the charmed quark case. On the other hand, the PDF for these light valence quarks are much larger.

There is also the possibility of electromagnetic ψ production via a virtual photon, as illustrated in fig 1.12.

1.4.4 Gluon Models

In these models, since the ψ (C = - 1) cannot couple directly to two gluons (from charge conjugation considerations), it is either produced along with a soft gluon [1.17], as in fig 1.13, or via an

intermediate $\chi(C = +1)$ state [1.15, 1.18], as in fig 1.14. Furthermore, the gluons carry a substantial fraction of the momentum of the hadrons, although their PDF still fall off more rapidly than those of the light valence quarks.

1.5 PREDICTIONS AND DATA

The predictions of the parton models described above are compared with the data which existed from the following experiments:

(i) CERN-College de France-Orsay-Saclay (NA3) [1.20]
150, 200, 280 GeV/c π, K, p beams H_2, Pt targets

(ii) Chicago-Illinois-Princeton (CIP) [1.21]
225 GeV/c π, K, p beams C, Cu, W targets

(iii) Birmingham-CERN-Ecole Polytechnique (Ω) [1.22]
39.5 GeV/c π, K, p beams W target

(iv) Saclay-Imperial College-Indiana-Southampton (WA11) [1.23]
150, 175, 185 GeV/c π beams Be target.

Due to the common parton model approach, the discussion of ψ production data below uses many of the basic ideas involved in the discussion of the lepton pair continuum in section 1.2. Emphasis is again given to those aspects which will not be discussed later in the chapters dealing with the results of the analysis.

1.5.1 Ratios of Cross-Sections

From the observation that the ratio of ψ resonance to background

lepton pair production in hadronic interactions is about a factor 100 greater than that in e^+e^- collisions, it may be concluded that the ψ is produced via a strong interaction process, rather than electromagnetically, in hadronic collisions. A similar conclusion may be drawn from the result that the ratio $\frac{\sigma(\pi^+ N \to \psi)}{\sigma(\pi^- N \to \psi)}$ is very close to unity, compared with $\frac{1}{4}$ for the lepton pair continuum (section 1.2.2).

Measurements of an upper limit for the production of associated charm by searching for extra leptons from semi-leptonic decays of charmed particles give $\frac{\sigma(\psi D\bar{D})}{\sigma(\psi)} < 0.01$. Searches in the WA11 experiment for D decays into hadrons (K, π) give $\frac{\sigma(\psi D\bar{D})}{\sigma(\psi)} < 0.15$. These upper limits, and the smallness of the charmed quark sea measured in deep inelastic lepton scattering, suggest that the charmed quark process is not an important contribution to ψ production.

Another important measurement is the ratio of ψ production by protons to that by antiprotons. The valence quark model predicts a very small value since the proton has no valence antiquarks, whereas the gluon model predicts a value of unity. The measured values for $\frac{\sigma(pN \to \psi)}{\sigma(\bar{p}N \to \psi)}$ are :

$0.19 \pm .03$ at 39.5GeV/c, $0.50 \pm .08$ at 150 GeV/c, $0.71 \pm .16$ at 200GeV/c .

These values suggest that both mechanisms contribute over this energy range, the quark mechanism being more important at lower energies, and the gluon mechanism dominating at higher energies.

There are results from different kinematical regions on the proportion of ψ produced via an intermediate χ state, WA11 finding a value of $0.36 \pm .05$, from a search for photons accompanying the ψ.

References

1.1 J.Aubert et al., Phys. Rev. Lett. 33 (1974) 1404.

1.2 S.Herb et al., Phys. Rev. Lett. 39 (1977) 252.

1.3 J.Christenson et al., Phys. Rev. Lett. 25 (1970) 1523.

1.4 S.Drell, T.Yan, Phys. Rev. Lett. 25 (1970) 316.

1.5 J.Badier et al.,CERN EP 79-67,68,137,147,80-150.

1.6 K.Anderson et al., Phys. Rev. Lett. 42 (1979) 944,948,951.

1.7 M.Corden et al., CERN EP 80-152.

1.8 R.Barate et al., Phys. Rev. Lett. 43 (1979)1541,
CERN EP 79-69.

1.9 H.Politzer, Nucl. Phys. B129 (1977) 301.

1.10 G.Altarelli, R.Ellis, G.Martinelli,Nucl. Phys. B157 (1979) 461.

1.11 J.Kubar-Andre, F.Paige, Phys. Rev. D19 (1979) 221.

1.12 F.Halzen, D.Scott, DAMTP 81/12.

1.13 M.Green, M.Jacob, P.Landshoff, Nuovo Cimento 29A (1975) 123.

1.14 J.Gunion, Phys. Rev. D11 (1975) 1796.

1.15 S.Ellis, M.Einhorn, C.Quigg, Phys. Rev. Lett. 36 (1976) 1263.

1.16 A.Donnachie, P.Landshoff, Nucl. Phys. B112 (1976) 233.

1.17 M.Gluck, J.Owens, E.Reya, Phys. Rev. D17 (1978) 2324.

1.18 C.Carlson, R.Suaya, Phys. Rev. D18 (1978) 760.

1.19 J.Owens, E.Reya, Phys. Rev. D17 (1978) 3003.

References (cont'd)

1.20 J.Badier et al., CERN EP 79-61, 80-149,
Phys. Lett. 86B (1979) 98.

1.21 J.Branson et al., Phys. Rev. Lett. 38 (1977) 580, 1331,1334,
42 (1979) 944, 948.

1.22 M.Corden et al., CERN EP 80-140.

1.23 R.Barate et al., Phys. Lett. 82B (1979) 145, Papers submitted to:
Rencontre de Moriond, Les Arcs (1980),
Int. Conf. on High-Energy Physics, Madison (1980).

Figures

LEPTON PAIR CONTINUUM PRODUCTION.

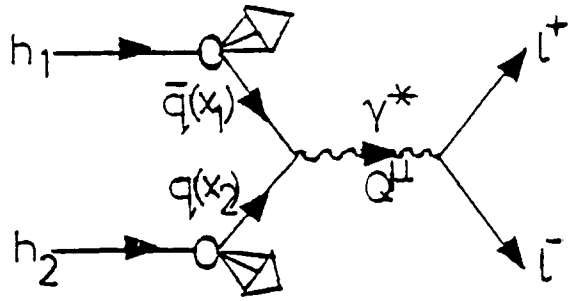

1.1

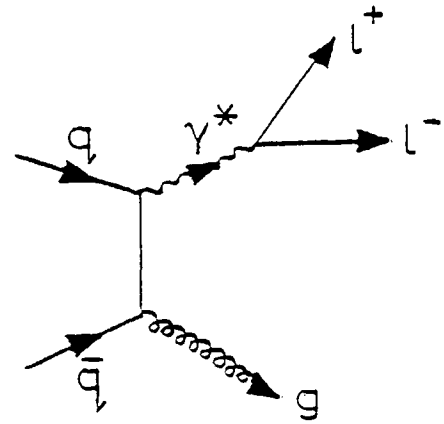

1.2

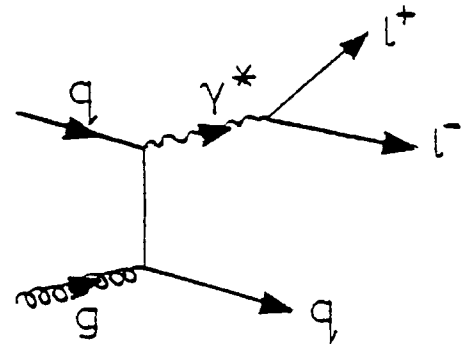

1.3

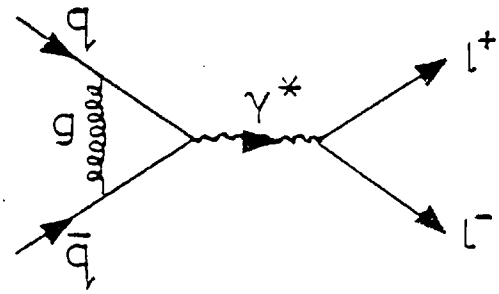

1.4

DEEP INELASTIC LEPTON SCATTERING.

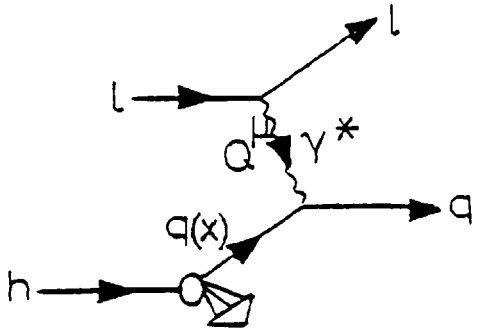

1.5

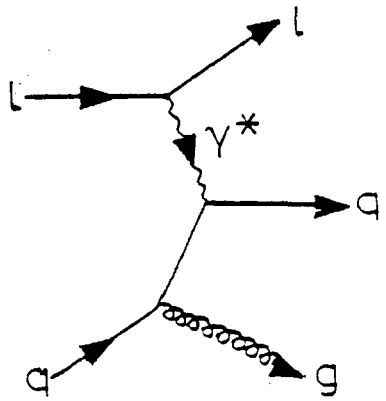

1.6

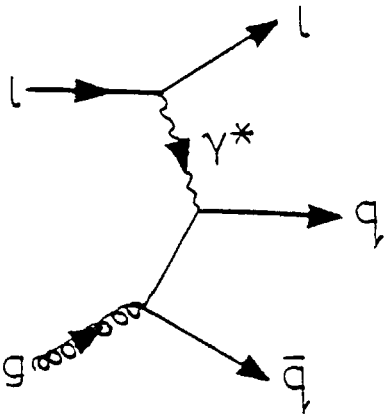

1.7

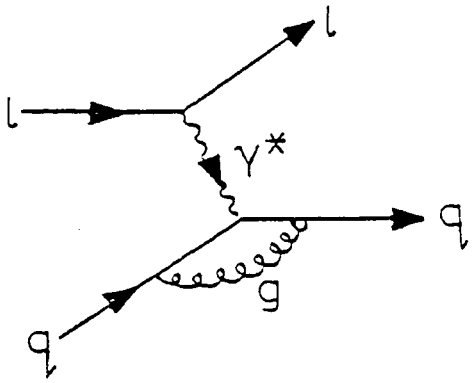

1.8

ψ PRODUCTION.

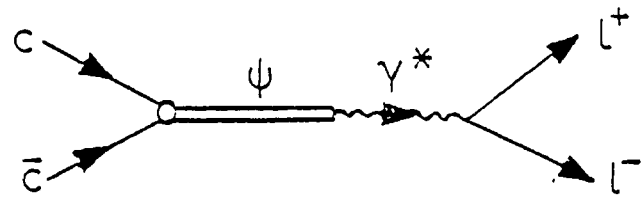

1.9

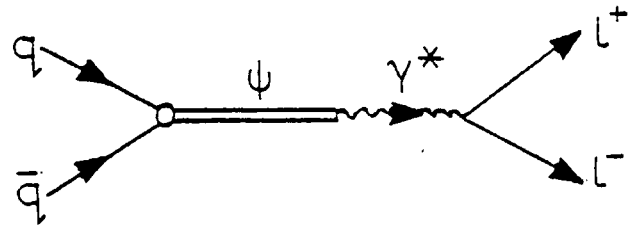

1.10

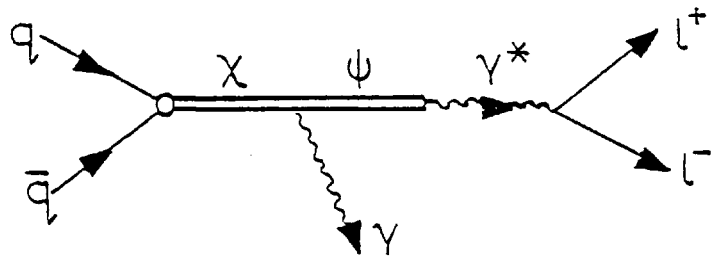

1.11

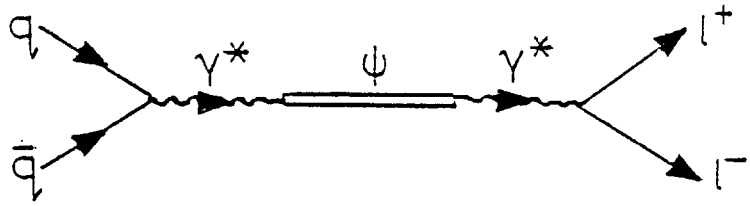

1.12

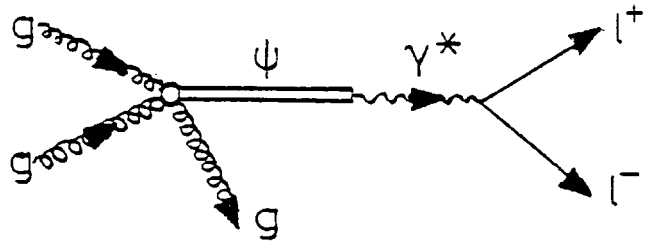

1.13

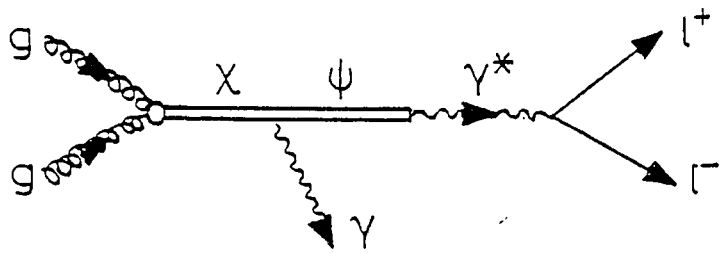

1.14

CHAPTER 2

THE WA11 EXPERIMENT

2.0 INTRODUCTION

In this chapter, a general discussion of the method of detecting lepton pairs in high energy collisions of hadrons is followed by a detailed description of the CERN WA11 experiment, the data of which is discussed later in this thesis.

2.1 EXPERIMENTAL METHOD

2.1.1 Electron or Muon Pairs

Lepton pair experiments can be performed looking for either electron or muon pairs, since both have properties which allow their observation against the large hadronic background produced in hadronic interactions.

For the case of electron pairs, the energy of the electrons is measured as they produce electro-magnetic showers in a calorimeter. The energy resolution is typically $\frac{\Delta E}{E} \sim \frac{R}{\sqrt{E}}$, thus improving as the energy E increases. The factor R depends on the characteristics of the calorimeter, improving with the quality of the sampling of the shower, typical values being 10% - 50% (FWHM) . The main backgrounds are electrons from conversions of photons from π^0 and η decays, and hadrons misidentified as electrons. The first source is reduced by minimising the amount of material between target and detector, while separation of electrons from hadrons is usually assisted by Cerenkov information.

For the case of muon pairs, the momentum of the muons is measured by the curvature of their trajectories in a magnetic field. The momentum resolution is typically $\frac{\Delta p}{p} \sim Rp$, thus deteriorating as the momentum p increases. The factor R depends on the characteristics of the magnetic spectrometer, improving with magnetic field strength and length of measured trajectory. The identification of muons is obtained by filtering out the hadrons with a suitable absorber.

2.1.2 Beam-Dump or Open-Spectrometer

A further choice available to muon pair experiments is whether to use a "beam-dump" or "open-spectrometer" set-up.

In a beam-dump experiment, an absorber (typically iron with a core of a heavy material such as tungsten or uranium) is placed just downstream of the target, to filter out the secondary hadrons and to stop the non-interacting beam particles. This results in a clean trigger, since the only particles detected are muons produced either directly in the primary interaction or from particles which decay upstream of the absorber. Consequently a high luminosity can be achieved. It also allows the possibility of searching for extra muons from decays of very short-lived particles. However, the muon pair mass resolution is seriously deteriorated by the multiple coulomb scattering of the muons in the heavy absorber, which occurs before the measurement of the muon momentum. The standard deviation of the roughly gaussian-distribution of net deflection angles resulting from small-angle multiple coulomb scattering is $\theta_{rms} \simeq 7$ mrad for a 25 GeV/c muon passing through 1.5m of iron (these are typical values). This gives a mass resolution of typically $\frac{\Delta m}{m} \simeq 5\%$, or $\Delta m \simeq 150$ MeV/c^2 at the ψ mass. The NA3, CIP, Ω experiments, whose results were discussed in chapter 1, all used this

beam-dump design.

In contrast, an open-spectrometer experiment attempts to measure and identify as much of the final state as possible. The muon filter is now placed downstream of the spectrometer and so the mass resolution is very much improved. However, since all interactions can now produce particles which enter the spectrometer, the luminosity of the experiment (which is limited by the rate of particles in the detector) is much lower. Unfortunately, in the space required for the spectrometer (typically several metres), secondary hadrons may decay, producing additional muons which contribute to the trigger. For example, $K \rightarrow \mu\nu$ (mean life $c\tau = 3.7$m) and $\pi \rightarrow \mu\nu$ (mean life $c\tau = 7.8$m).

2.1.3 The WA11 Proposal

The proposal by a collaboration of CEN Saclay and Indiana University, for an experiment to "search for high mass states produced with the ψ (3.1)", in the West Area of the CERN SPS [2.1], was accepted in February 1976, and became the WA11 experiment. The original aim of this experiment was to achieve an understanding of the production mechanism of the recently discovered ψ. The ψ was to be detected by its decay to a muon pair. In order to look for hadrons from decays of any high mass states produced with the ψ, (for example, the charmed hadrons expected in the charmed quark model (section 1.4.2)) detection of as much of the final state as possible was required. This was to be achieved with an open-spectrometer set-up.

Imperial College then joined the collaboration, providing an electro-magnetic calorimeter for the set-up [2.2]. Electron detection would allow a search for leptons from decays of any high mass states

produced with the ψ, while photon detection would allow an investigation of χ production and decay to $\psi\gamma$. The possibility of detecting the ψ by its decay to an electron pair was also provided. Data taking began in September 1977.

2.2 APPARATUS

The WA11 apparatus as used during the final year of running (August 1979-June 1980) is shown in fig 2.1,and described in this section.

2.2.1 Beam

A negative pion beam was used at momenta 175, 185, 192.5, 195, 197.5 GeV/c. A schematic layout of the H3 beam line in the West Area of the CERN SPS is shown in fig 2.2, and a description can be found in ref [2.3]. A pulse of 3×10^{12} protons yielded a pion intensity of 10^7 during a 1.5 second spill. The momentum acceptance was $\pm$ 1%. The fraction of contamination from other negative hadrons was negligible (4×10^{-3} for K^-, 5×10^{-4} for $\bar{p}$); a good reason for using a negative pion beam. Thin scintillator-strip horizontal and vertical hodoscopes T0, T1 helped steer the beam onto the target, and were used in the data analysis to help measure the beam trajectory. Veto counters AMU1, AMU2 helped reject the μ-halo accompanying the beam ($0.2 \times 10^6 \mu/m^2$).

2.2.2 Target

A target of beryllium (A = 9, Z = 4) was used. This target, of total length 18.8 $g.cm^{-2}$, was divided into three separate small blocks

in order to reduce secondary interactions, especially photon conversions, and to help check the vertex location.

This beam and target arrangement gave an event rate per pulse of 10^7 . 18.8 . 6.02 x 10^{23} . σ = 1.1 x 10^{32} . σ, where σ is the relevant cross-section (in cm^2). The total $\pi^- p$ cross-section at these energies is $\simeq$24 x $10^{-27} cm^2$, giving a total of $\simeq$2.6 x 10^6 interactions in the target per pulse.

2.2.3 Magnetic Spectrometer

The unique feature of WA11 compared to other lepton pair experiments was to be its ability to measure and identify as much of the final state as possible, and so no absorber was placed between the target and the magnetic spectrometer.

The magnetic spectrometer, providing momentum measurement, consisted of 13 multiwire proportional chambers (MWPC) inside the "Goliath" magnet, and 3 following it. The two smaller MWPC D14, D15 (of size 0.62 x 0.22 m^2) each had three planes of sense wires; one vertical (1mm pitch) and two tilted (2mm pitch). The other MWPC in Goliath D3-D13 (1.80 x 0.74m^2) each had four planes; vertical,horizontal and two tilted (all 2mm pitch). Each of the three larger MWPC DO-D2 (3.1 x 2.1 m^2) following Goliath also had four planes, similarly arranged, but with 3mm pitch. To protect the beam zone of the MWPC, thin mylar foils ("beam killers") were placed on each side of the sense wire plane. These also killed some secondary tracks passing close to the beam path and corrections had to be applied for this effect, (section 5.1.1). The Goliath magnet had a vertical magnetic field of 1.5T, coil diameter 2m and gap 1.05m.

These parameters of the spectrometer gave momentum and angular resolutions for a muon track of momentum $\gtrsim$ 5 GeV/c (neglecting multiple coulomb scattering which dominates at lower momenta) $\frac{\Delta p}{p} \simeq 0.9 \times 10^{-3}$ p (in GeV/c) and $\Delta\theta \simeq 1.2$ mrad. A ψ which is produced at rest in the centre of mass system by a 185 GeV/c beam, and then decays symmetrically, gives muons of laboratory momenta p = 15.4 GeV/c and opening angle θ = 200 mrad. The calculated mass resolution in this case is $\frac{\Delta m}{m} \simeq 1.5\%$.

The 4 x 7 cell threshold Cerenkov counter, for particle identification, was filled with CO_2 at atmospheric pressure. The condition for emission of Cerenkov radiation when a particle passes through a medium is $\beta n > 1$, where β is the velocity of the particle and n is the refractive index of the medium. This can be rewritten as $p > \frac{m}{\sqrt{2\varepsilon}}$, where m, p are the mass and momentum of the particle, and $\varepsilon = n - 1$, ($\varepsilon \ll 1$). For CO_2 at 1 atmos., $\varepsilon = 410 \times 10^{-6}$, giving thresholds of 5, 17, 33 GeV/c for π, K, p respectively.

2.2.4 Muon Filter

The filter for the detection of muons and for the muon pair trigger was composed of 2380 g.cm^{-2} of iron preceded by a horizontal hodoscope H1H, and followed by horizontal and vertical hodoscopes H3H, H3V. Each horizontal hodoscope was divided into four quadrants around the beam axis, and had a central horizontal gap subtending $\pm$ 20 mrad at the target. The horizontal scintillator counters were arranged so that the edges of corresponding strips in H1H, H3H pointed back to the target in the vertical plane. After this filter came a wall of concrete blocks, and another hodoscope PAPILLON, providing further filtering. The outer limits of the hodoscopes subtended angles of $\pm$ 250 mrad

horizontally and $\pm$ 160 mrad vertically at the target.

2.2.5 Calorimeter

The electromagnetic calorimeter was composed essentially of lead - scintillator - sandwich modules for energy measurement, and used the MWPC DO as a shower position detector. Horizontal strips of scintillator sampled the shower after 2.9, 6.6, 35.2 radiation lengths, while vertical lead-scintillator-sandwich modules summed the energy deposited by the shower between 2.9 and 17.3 radiation lengths. The energy resolution achieved with this calorimeter was $\frac{\Delta E}{E} \simeq \frac{50\%}{\sqrt{E}}$ (FWHM). The calorimeter is described fully elsewhere [2.4].

2.3 TRIGGERS

2.3.1 Interaction Trigger

A beam particle signal "PINC" (Pion INCident) was given by a coincidence of signals in the beam hodoscopes T0, T1 and the beam defining counter S1 and no signal in either of the muon-halo veto counters AMU1, AMU2 upstream of the target:

$$PINC = T0.T1.S1.\overline{AMU1}.\overline{AMU2} \qquad (2.1)$$

An interaction trigger "DIF" (DIFfusion) was given by a coincidence between the beam particle signal, and a signal in each of the interaction counters W1, W2 placed above and below the beam at the entrance to Goliath:

$$DIF = W1.W2.PINC \qquad (2.2)$$

2.3.2 Muon Pair Trigger

This trigger attempted to enhance the signal of muons resulting from ψ decays, relative to the background from other sources. These background sources included:

(i) The decays in the 8m between the target and muon filter, of some of the particles produced in the interaction, mainly pions and kaons.

(ii) The considerable flux of halo muons accompanying the beam.

(iii) The "punch-through" of high energy hadrons reaching the downstream muon hodoscopes.

The $\mu^+\mu^-$ invariant mass $m_{\mu^+\mu^-}$ is given approximately by

$$m^2_{\mu^+\mu^-} \simeq P_{\mu^+}.P_{\mu^-}.\theta^2_{\mu^+\mu^-} \qquad (2.3)$$

where $P_{\mu^+}(P_{\mu^-})$ is the momentum of the $\mu^+(\mu^-)$ and $\theta_{\mu^+\mu^-}$ is the opening angle between them. Thus a high invariant mass, such as that of the ψ, leads to high momentum muons with a large opening angle.

The trigger principle, illustrated in fig 2.3, combined the following factors:

(i) Most muons of low momentum ($\lesssim$ 5 GeV/c) were bent out of the apparatus by the magnetic field of Goliath or failed to penetrate the iron. Since the number of muons from pion and kaon decays decreases as the momentum of the parent increases (due to the Lorentz γ-factor in the mean lifetime) this momentum cut-off rejects mainly background muons.

(ii) A single muon track was required to pass through corresponding horizontal strips of H1H, H3H and hence point to the target in the vertical plane (the vertical component of momentum being parallel to, and hence unaffected by, the magnetic field). This

requirement, along with that of the veto counters in the interaction trigger, helped reject the muon-halo.

(iii) H3V was used to require the pair of muons to be in diagonally opposite quadrants and, because of the gaps in H1H, H3H, to have a minimum opening angle of 40 mrad. This favoured pairs of muons of opposite sign with large invariant mass. (PAPILLON was used to select muons of higher transverse momentum, and provided an additional filter).

A resulting average trigger rate of 5×10^{-6} per incident pion was obtained, leading to 50 triggers per pulse. Comparing this to the total number of interactions in the target (2.6×10^{6}), gives one trigger per 50,000 interactions, showing the excellent selectivity which can be achieved with a muon pair trigger, even in this open-spectrometer configuration.

2.3.3 Electron Pair Trigger

An attempt to select electron pairs resulting from ψ decays was made using the calorimeter and Cerenkov counter. A large background of electrons came from photon conversions and hadrons misidentified as electrons. The resulting trigger rate was about three times the muon pair rate, and was used only for a limited period. The electron pair trigger is described fully elsewhere [2.5].

2.4 DATA ACQUISITION

Signals from the counters and chambers were read, via a CAMAC interface, into the PDP 11/45 on-line computer, whenever the hardware trigger was satisfied. As well as writing the data to magnetic tape,

the computer provided information, including event displays, for monitoring and checking the apparatus. During the period August 1979-June 1980, approximately 3000 raw data tapes, containing 40 million triggers were written by the data acquisition system.

References

2.1 Proposal 58, CERN SPSC 76-3.

2.2 Proposal 175, RL PPESP 76-1.

2.3 D.Plane, CERN SPS EA 78-7.

2.4 A.Wylie, PhD Thesis, London (1979).

2.5 G.King, PhD Thesis, London (1980).

Figures

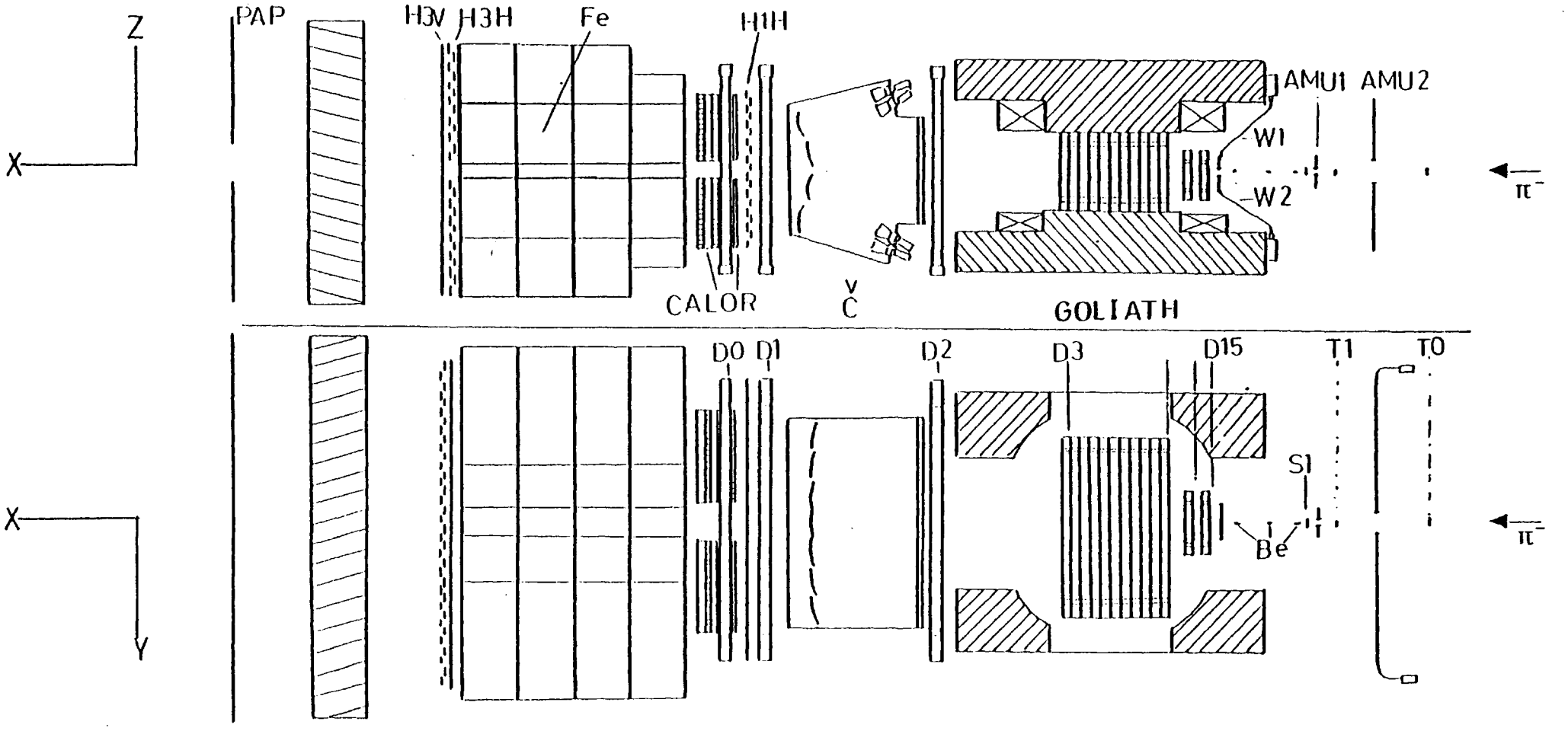
Z
X
PAP
H3V
H3H
Fe
H1H
CALOR
C
AMU1
AMU2
W1
W2
π⁻
GOLIATH
X
Y
D0
D1
D2
D3
D15
T1
T0
S1
Be
π⁻
1m

2.1 WA11.

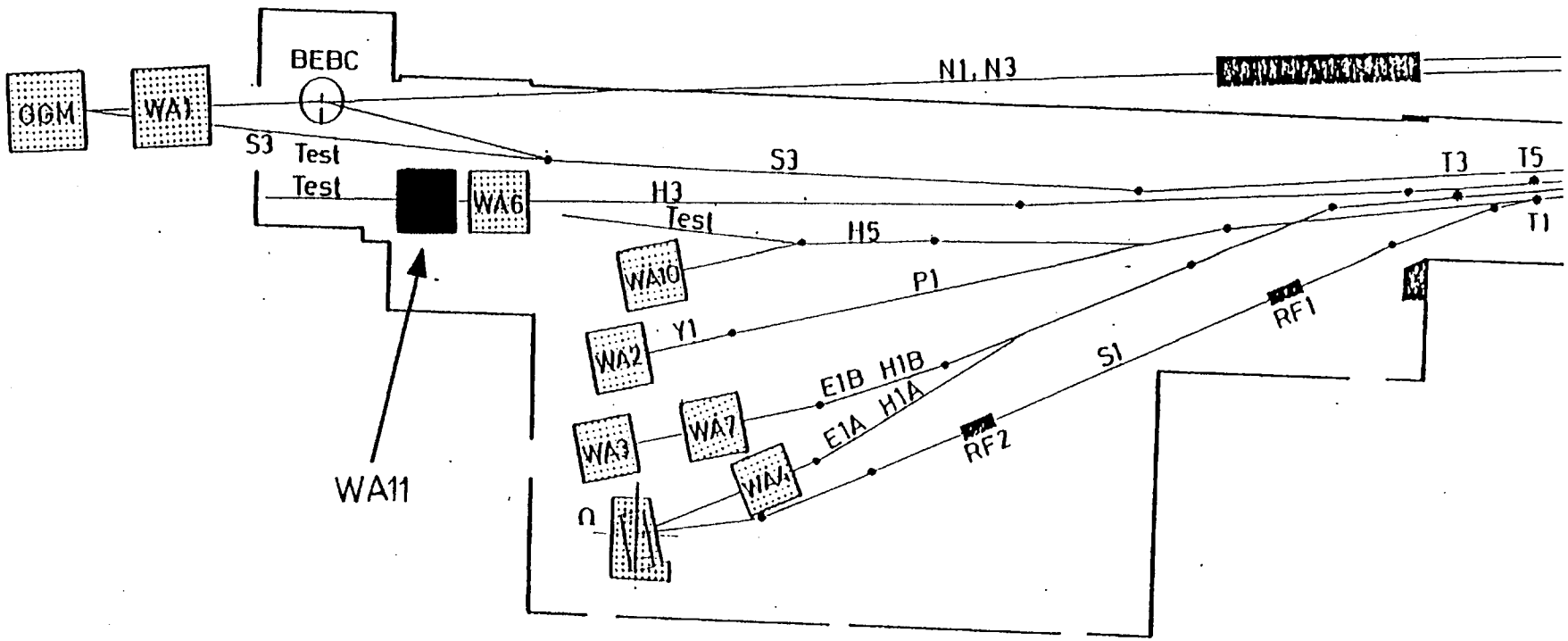

2.2 CERN WEST AREA.

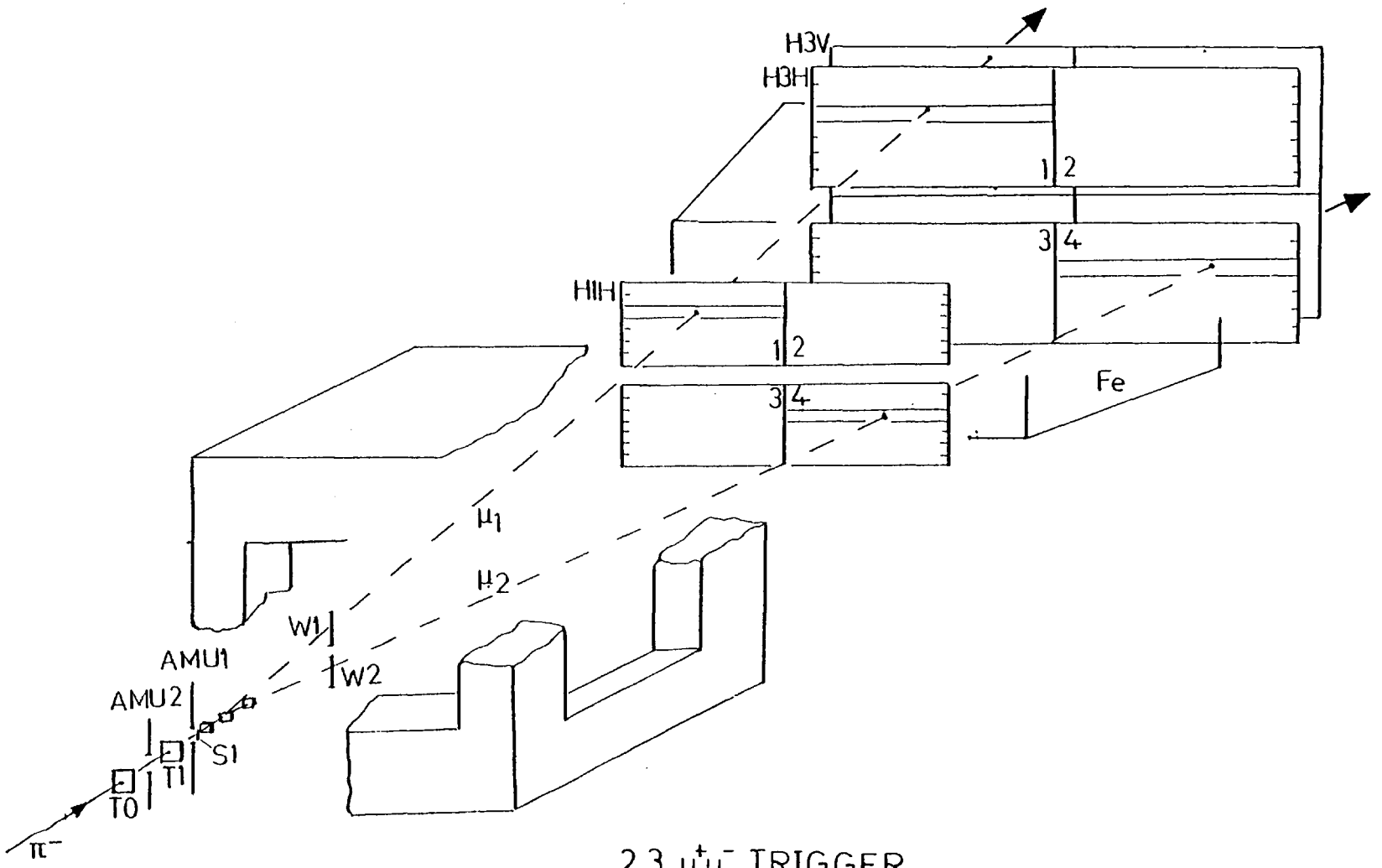

2.3 $\mu^+\mu^-$ TRIGGER.

CHAPTER 3

DATA PROCESSING

3.0 INTRODUCTION

The data reduction procedure, and performance of the WA11 apparatus and trigger as calculated by monte-carlo techniques are described in this chapter.

3.1 DATA REDUCTION PROCEDURE

3.1.1 Strategy

From the appropriate cross-section for ψ production and branching ratio for decay to a muon pair, and the acceptance of the WA11 experiment, the expected number of $\psi \rightarrow \mu^+\mu^-$ events was 0.1 per pulse of 10^7 pions. Since the trigger rate was 50 per pulse, this means that only one in 500 triggers was from a genuine $\psi \rightarrow \mu^+\mu^-$ event.

Due to the complexity of the pattern recognition, reconstruction for all of the large number of triggers written to tape would have taken too much computer time, and so the raw data tapes were first passed through a fast filter to improve the signal to background ratio. Those triggers which survived this fast filter were then passed through the reconstruction program. Finally, a special program used the Cerenkov information for secondary particle identification.

The three stages of the data reduction process are illustrated in fig 3.1, and described below.

3.1.2 Fast Filter

The fast filter program analysed the raw data tapes on which the triggers had been written by the data acquisition system. It checked the hardware trigger logic and then, using the hit counters of the muon hodoscopes, defined regions in the large MWPC D1, D2 through which the muons should have passed. In these regions of the "lever-arm" MWPC D1, D2, the program then searched for "points"; that is, where a track had passed through the chamber producing signals on clusters of wires. Using these points and a simple approximation for the magnetic field, the program then attempted to construct muon trajectories passing through the target and having momentum > 3 GeV/c. A trigger was then rejected unless a pair of muons was found with invariant mass $\geq$ 2 GeV/c^2, as calculated from this rough procedure. This stage of the data reduction process took 20 ms/trigger (on a CDC 7600) and reduced the number of triggers by a factor of 25.

3.1.3 Reconstruction of Charged Tracks

The program "TRIDENT" (TRack IDENTification) analysed the tapes written by the fast filter program, performing reconstruction of charged tracks. It created tracks from the lever-arm MWPC D1, D2 and followed them back towards the target, through the MWPC inside Goliath. The resulting tracks were then fitted to a primary vertex and up to five secondary V-zero vertices from decays of neutrals. This complex stage of the data reduction process took 200ms/trigger.

The total computer time required by these first two stages of the data reduction process was thus $20 + \frac{1}{25} \times 200 = 28$ ms/trigger, (that is, 300 hours for 40 million triggers), a factor 7 less than if reconstruction had been applied to all of the original triggers.

3.1.4 Cerenkov Program

A subsequent program generated photons (using monte-carlo techniques) along each track traversing the Cerenkov counter, under each of the hypotheses that this track was an e, π, K or p. It followed these photons through the optical system of the Cerenkov counter, thus giving the expected number of photoelectrons recorded at the photomultiplier of each cell, under each hypothesis. This expected number was then compared to the actual number seen, giving a poisson probability for each hypothesis. (Normalisation was obtained from known tracks; for example: μ from ψ, π from K^o).

The results of the reconstruction and Cerenkov programs for good events were written onto data summary tapes for further analysis.

3.2 APPARATUS AND TRIGGER PERFORMANCE

3.2.1 GEANT Monte-Carlo

The performance of the WA11 apparatus and trigger was studied within the framework of the monte-carlo package "GEANT" [3.1] (Generation of Events ANd Tracks). This program performs four consecutive tasks:

(i) generation of kinematics;

(ii) generation of tracks in space;

(iii) intersection of tracks with apparatus;

(iv) digitisation (and writing of "data" tapes for subsequent analysis by the data reduction programs).

Each stage which is required has to be supplied with appropriate user routines which describe the particular experiment being studied.

3.2.2 Kinematics

Six variables are required to describe completely a muon pair (each muon has 3 components of momentum). It is natural to choose a set which contains simple variables of interest. One such choice is: $\{m, x_L, p_T, \omega, \theta, \phi\}$. The first four variables refer to the muons as a pair: m and x_L are the mass and scaled longitudinal momentum, p_T and ω are the transverse momentum and its azimuthal angle around the beam axis. The last two variables refer to just one of the muons: θ and ϕ are the polar and azimuthal angles with respect to a particular axis (defined in section 4.5).

The kinematical distributions of the muons measured in the experiment are corrected for the acceptance of the apparatus and trigger as calculated by monte-carlo studies. This could be done by generating muon pairs at each point of the 6-dimensional array of variables, and tracking them through the apparatus to see if they satisfy the trigger. Each muon pair in the data would then be weighted according to the acceptance calculated at the point of the array at which it occurred. However, this procedure would require an unreasonably large amount of computer time, and be extremely wasteful as it would populate regions of the array where there were no data.

Instead, muon pairs are generated according to models which give a realistic representation of the data. Then, the kinematical distribution in any particular variable of interest is corrected for the acceptance as a function of that variable, thus involving an integration over the acceptance as a function of the other variables. The weakness of this procedure is that the results can be model dependent, and due consideration must be given to this problem (section 3.2.4).

Two models were chosen, both of the parton-parton type, discussed in chapter 1, since these are simple to use and of obvious physical interest, as well as giving a realistic representation of the data. These models were:

(i) Valence quark-antiquark annihilation, for the ψ resonance and for the muon pair continuum.

(ii) Gluon-gluon fusion, for the ψ resonance.

A muon pair was generated by the following procedure:

(i) Partons were chosen with longitudinal momentum fractions x_1, x_2 according to the appropriate parton PDF for the beam and target. The values of m and x_L for the muon pair are then given by eqns. 1.3, 1.4 in terms of the chosen x_1, x_2 values of the partons.

(ii) An allowed value of p_T was then chosen for the muon pair from a distribution which fitted the data with $\langle p_T \rangle$ = 1.0 (1.2) GeV/c for the ψ (continuum). The ω angle was chosen from a flat distribution.

(iii) The θ, ϕ angles for one of the muons were then chosen according to an angular distribution of the form:

$$\frac{dN}{d(\cos\theta)d\phi} \sim 1 + \lambda\cos^2\theta,$$

with $\lambda = 0$ for the gluon-gluon (gg) model, and $\lambda = 1$ for the quark-antiquark ($q\bar{q}$) model.

Having thus generated a muon pair, it was possible to apply loose cuts in a short routine ("REACC") to see whether it could be rejected in this first (kinematics) stage in order to save time. The muons were required to have momentum > 4GeV/c, to have vertical projections such that they would not be outside the limits or inside the gaps of the

muon hodoscopes (allowance being made for multiple coulomb scattering) and would form an "up-down" pair. (The vertical component of momentum, being parallel to the magnetic field, would only be affected by multiple coulomb scattering during the second (tracking) stage). Only those muon pairs which passed REACC (less than half) were put through the tracking stage.

3.2.3 Tracking

Each muon pair which passed REACC was then tracked through the apparatus using routines for the magnetic field, the various media, multiple coulomb scattering, etc. The following series of cuts, which represent the muon pair trigger, was then applied:

(i) "PAP": a muon was required to give a hit in PAPILLON, the muon hodoscope furthest downstream.

(ii) "H3V": a muon was required to give a hit in the vertical H3V hodoscope.

(iii) "H3H": a muon was required to give a hit in the horizontal H3H hodoscope, the number of the counter it hit being noted.

(iv) "H1H": a muon was required to give a hit in the horizontal H1H hodoscope, and the counter it hit to correspond to the one noted for H3H.

(v) "DIAG": a pair of muons had to form a "left-right" pair (combining this with the "up-down" requirement in REACC ensured that the muons hit diagonally opposite quadrants of the muon hodoscope).

Table 3.1 contains a summary, for each model, of the losses due to each of the above criteria.

3.2.4 Acceptance, Resolution, Efficiency

The (geometrical) acceptance of the set-up as a function of m, the muon pair mass, is shown in fig 3.2. The acceptance as a function of the variables x_L, p_T and $\cos\theta$, for the ψ (gg model) and continuum ($q\bar{q}$ model), is shown in figs. 3.3 - 3.5. For any result on the properties of the muon pairs (chapter 4), the quoted error includes a contribution which reflects the change in the result produced by a change in the model used to calculate the acceptance.

By passing the monte-carlo generated muon pairs through stages (iii) and (iv) of GEANT, the experimental resolution was found to be: $\frac{\Delta m}{m} \simeq 1.2\%$, $\Delta x_L < 0.01$, $\Delta p_T < 50$ MeV/c. The overall efficiency for ψ detection, including the fast filter and reconstruction programs, was computed by mixing monte-carlo generated muon pairs with experimental data, and found to be $\simeq 70\%$ (of events accepted by the trigger)

References

3.1 R.Brun et al., CERN DD/78/2.

Tables

Figures

3.1 LOSSES DUE TO APPARATUS AND TRIGGER REQUIREMENTS.

MODEL:	QUARK-ANTIQUARK RESONANCE	QUARK-ANTIQUARK CONTINUUM	GLUON-GLUON RESONANCE
MUON PAIRS GENERATED:	50 000 (100.00%)	52 479 (100.00%)	48 661 (100.00%)
LOSSES IN:			
REACC:	33 271 (66.54%)	30 374 (57.88%)	28 093 (57.73%)
PAP:	6 649 (13.30%)	8 138 (15.51%)	7 414 (15.24%)
H3V:	16 (0.03%)	8 (0.02%)	13 (0.03%)
H3H:	279 (0.56%)	335 (0.64%)	320 (0.66%)
H1H:	1 348 (2.70%)	936 (1.78%)	1 647 (3.38%)
DIAG:	2 038 (4.08%)	1 894 (3.61%)	2 506 (5.15%)
MUON PAIRS ACCEPTED:	6 399 (12.80%)	10 794 (20.57%)	8 668 (17.81%)

3.1 DATA REDUCTION PROCEDURE.

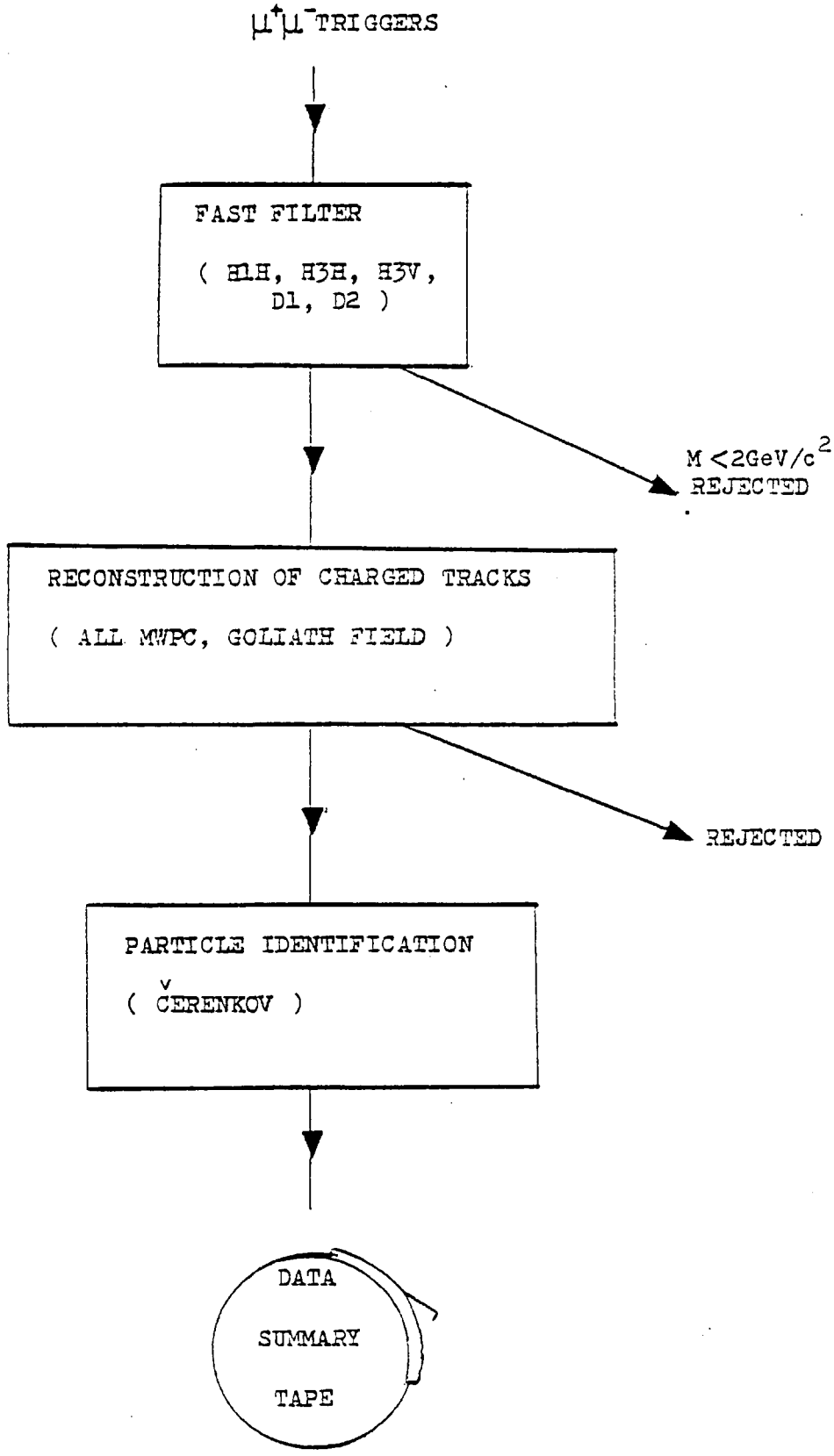

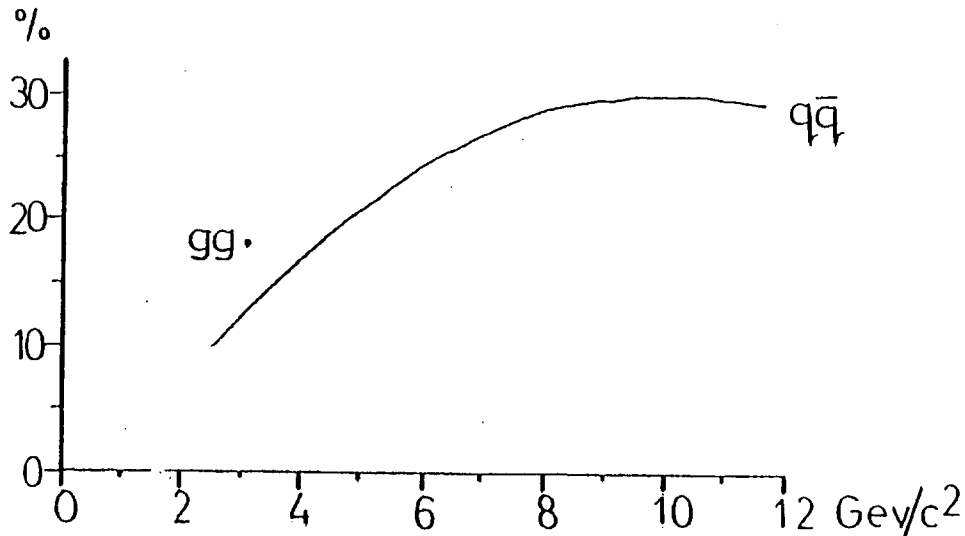

3.2

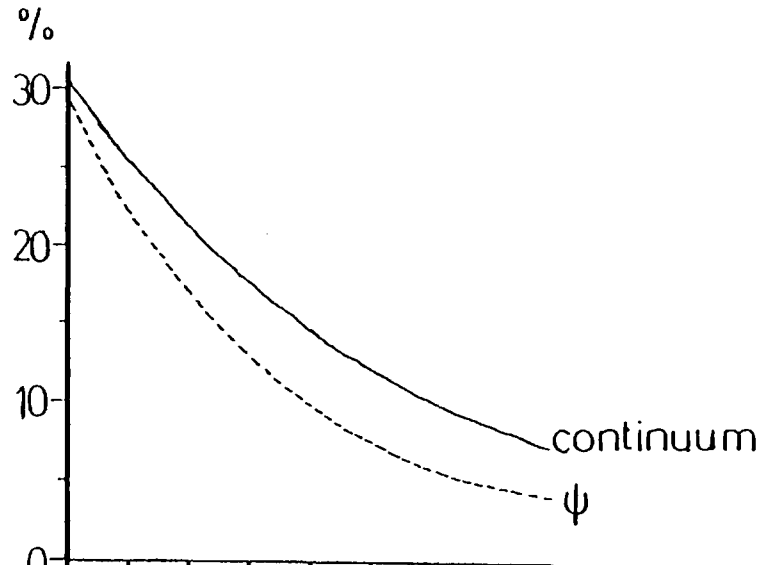

3.4

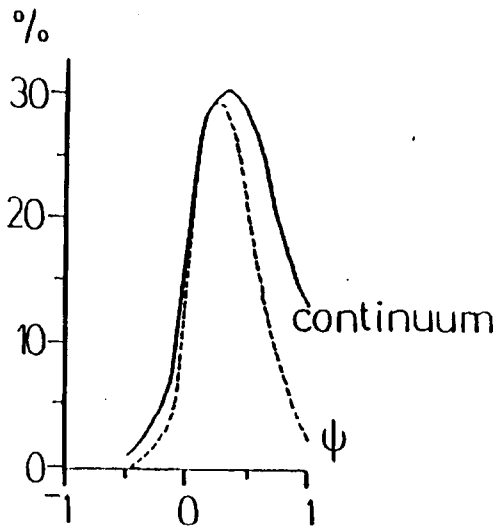

3.3

ACCEPTANCE.

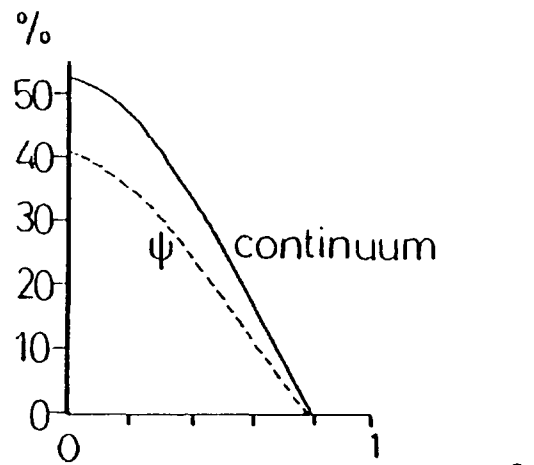

3.5

CHAPTER 4

PROPERTIES OF THE MUON PAIRS

4.0 INTRODUCTION

In this chapter, data on the kinematical distributions of the muon pairs are presented, and discussed in the context of the parton models described in chapter 1.

4.1 PRELIMINARIES

4.1.1 Data Sample

The data were taken at the WA11 experiment during 14 ten-day SPS runs between August 1979 and June 1980. From the triggers taken during this period, good events were written onto data summary tapes by the data reduction programs. Cuts were made on the quality of the muon tracks (momentum uncertainty, number of measured points, etc.) to select events with at least one pair of well measured muons originating from the main vertex and with invariant mass $\geq$ 2.5 GeV/c^2. For those events with more than two well measured muons, all possible pairs were considered. A total of 62 634 muon pairs satisfied these criteria, and these muon pairs are used in the analysis. The number of such pairs produced at the various beam momenta which were used is given in table 4.1. (Unless otherwise explicitly stated, the data from all these momenta were combined for the analysis, since the range of $\sqrt{s}$ covered was small: 18.2 - 19.3 GeV). The number of such pairs produced in various mass regions of interest between 2.5 and 11.5 GeV/c^2 is given in table 4.2.

The raw mass spectrum (that is, uncorrected for acceptance) for these muon pairs is shown in fig 4.1 (for opposite and like sign pairs separately), on a logarithmic scale showing clearly the four orders of magnitude covered between the signals of the ψ and the tail of the continuum. The raw mass spectrum for opposite sign pairs is also shown in fig 4.2, but on a linear scale. The narrow ψ signal dominates the spectrum.

4.2 MASS

The data are divided into three separate mass regions for the analysis of this section: the ψ, the ψ', and the continuum plus T regions.

4.2.1 ψ Region

The mass spectrum for the region between 2.8 and 3.4 GeV/c^2, corrected for acceptance, is shown in fig 4.3. The data in the regions 2.8-2.9 GeV/c^2 and 3.3-3.4 GeV/c^2 are fitted using an exponential which, interpolated under the ψ peak, gives an estimate of the background. This fit is also shown in fig 4.3. Then, the data minus this background are fitted using a gaussian. Although not an excellent fit, the gaussian gives a good estimate of the centre and width of the peak. The results of the fits are:

background fit: $\exp - \alpha m$; $\alpha = 2.46 \pm .05$ $(\text{GeV}/c^2)^{-1}$

resonance fit: $\exp - \frac{(m-m_\psi)^2}{2\sigma_\psi^2}$; $m_\psi = 3.104 \pm .001$ GeV/c^2, $\sigma_\psi = 38.2 \pm .2$ MeV/c^2

(The Particle Data Group tables [4.1] give $m_\psi = 3.097 \pm .001$ GeV/c^2)

The width of the peak (due entirely to mass resolution effects, since

the ψ has a decay width of only 63 KeV/c^2) demonstrates the excellent mass resolution of the apparatus $\frac{\Delta m}{m} \simeq 1.2\%$ which agrees with the monte-carlo estimate.

Special runs using an up-down trigger to collect like sign pairs (instead of the usual diagonal trigger which favours opposite sign pairs) indicated that the fraction of the background under the ψ peak due to π, K decays is $\simeq$ 40% (This was the work of other members of the collaboration). The remaining $\simeq$ 60% of the background is assumed to be due to prompt pairs produced as for the higher mass continuum. The number of ψ in the region 2.9-3.3 GeV/c^2 is 36 330 $\pm$ 720 (the error includes the statistical error and a 10% error in the estimate of background). This number of ψ is compared in section 4.2.4 to the number of ψ' and T, to obtain ratios of cross-sections for these three resonances.

4.2.2 ψ' Region

The ψ' peak emerges clearly and separately from the ψ peak, in contrast to the case of beam dump experiments where, due to multiple coulomb scattering of the muons, it appears only as a shoulder on the ψ peak. The mass spectrum for the region between 3.4 and 4.0 GeV/c^2, corrected for acceptance, is shown in fig 4.4. The data are well fitted using the sum of a gaussian and an exponential (χ^2 = 55 for 55 degrees of freedom (d.o.f)). The gaussian and exponential fits are also shown in fig 4.4. The results of the fits are:

background fit: $\exp - \alpha m$; $\alpha = 2.58 \pm .13$ $(\text{GeV}/c^2)^{-1}$

resonance fit: $\exp - \frac{(m-m_{\psi'})^2}{2\sigma^2_{\psi'}}$; $m_{\psi'} = 3.697 \pm .004$ GeV/c^2

$\sigma_{\psi'} = 43.1 \pm 3.1$ MeV/c^2

(The Particle Data Group tables [4.1] give $m_{\psi'} = 3.685 \pm .001$ GeV/c^2)

It can be seen that there is a large amount of background under the ψ' peak. The number of ψ' in the region 3.6-3.8 GeV/c^2 is 660 $\pm$ 84 (the error includes the statistical error and a 10% error in the estimate of background).

4.2.3 Continuum plus Υ Region

The mass spectrum for the region between 4.1 and 11.5 GeV/c^2, corrected for acceptance, and fitted using a single exponential (χ^2= 69 for 59 d.o.f) is shown in figure 4.5. The result of the fit is:

$$\text{continuum fit:} \quad \exp - \alpha m \; ; \; \alpha = 1.08 \pm .03 \; (\text{GeV}/c^2)^{-1}$$

The average muon pair mass is $\simeq$ 5 GeV/c^2.

The background from π, K decays, estimated from like sign pairs taken with the up-down trigger, falls off very quickly with mass, and is negligible in this region.

The small excess between 9 and 10 GeV/c^2, which is probably due to the resonances of the Υ family ($m_{\Upsilon} = 9.46$ GeV/c^2 [4.1]), corresponds to 18 $\pm$ 5 muon pairs.

4.2.4 Ratios of Cross-Sections

The ratios of cross-section times branching ratio into muon pairs for the three resonances (corrected for background and acceptance) are found to be:

$$\frac{Br(\psi' \rightarrow \mu^+\mu^-).\sigma(\psi')}{Br(\psi \rightarrow \mu^+\mu^-).\sigma(\psi)} = (1.5 \pm .2) \times 10^{-2} \quad \left(\text{giving } \frac{\sigma(\psi')}{\sigma(\psi)} = 0.13 \pm .02\right)$$

$$\frac{Br(T \to \mu^+\mu^-).\sigma(T)}{Br(\psi \to \mu^+\mu^-).\sigma(\psi)} = (2.2 \pm .5) \times 10^{-4}$$ (here T includes all the resonances of the T family between 9 and 10 GeV/c^2)

These values agree reasonably well with the other experiments at similar energies [1.20, 1.21]. However, the ratio of ψ' to ψ production at the lower energy of 39.5 GeV/c is $\frac{\sigma(\psi')}{\sigma(\psi)} \simeq 0.4$ [1.22].

The small value for the ratio of ψ' to ψ production, considering that the masses are similar when compared to $\sqrt{s}$, suggests some difference in production mechanism between the two resonances. This could be due to the fact that some ψ production occurs via intermediate χ states [1.23], whereas there are no such χ states which can decay in the same way to give a ψ'. Also, the change in this ratio from the lower to the higher energies suggests some change in production mechanism over this energy range. This is also indicated by the change in the ratio of ψ production by p to that by $\bar{p}$ (section 1.5.1). Of course, T production is expected to be highly suppressed because of the much greater mass involved.

4.3 LONGITUDINAL MOMENTUM

The (dimensionless) longitudinal momentum variable used here is $x_L \equiv \frac{p_L}{\frac{1}{2}\sqrt{s}}$, where p_L is the longitudinal momentum of the muon pair*. The x_L-distributions for the ψ and ψ' regions (2.9-3.3 GeV/c^2 and 3.6-3.8 GeV/c^2, respectively) are corrected for background by subtracting the distributions in the neighbouring mass regions (2.5-2.9 and 3.3-3.6 GeV/c^2 for the ψ, 3.3-3.6 and 3.8-4.8 for the ψ'), normalised appropriately.

---

* This variable is not the same as the other variable which is used (the Feynman variable) $x_F \equiv \frac{p_L}{p_L max}$, where $p_L max$ is the maximum longitudinal momentum which the muon pair could have. In fact, $p_L max \simeq \frac{1}{2}\sqrt{s}(1-\frac{m^2}{s})$, so that $\frac{x_L}{x_F} = 1-\frac{m^2}{s}$. This ratio varies from 0.97 at the ψ mass to 0.74 at the T mass, for a beam momentum of 185 GeV/c.

(A check on this procedure is made by using narrower mass regions for the ψ and ψ', and comparing the resulting distributions). The distributions are also corrected for acceptance. The resulting differential cross-section $\frac{d\sigma}{dx_L}$ for the ψ, ψ' and continuum alone (3.8-8.8 GeV/c^2) is shown in figs 4.6-4.8. (Insufficient statistics are available for a proper study of the Υ distribution).

One clear general feature is that all the distributions are centred about a positive non-zero value of x_L. This feature is also observed in the other experiments. In the context of a parton model, this suggests that the partons involved in the production mechanism are harder in the pion than in the nucleon, since $x_L = x_1 - x_2$. This is to be expected as the pion has fewer valence constituents than the nucleon, and hence from dimensional counting arguments, has harder parton PDF. Also, the distributions are not symmetric, even about this positive non-zero value, and fits using the common parametrisation $\frac{d\sigma}{dx_L} \sim (1 - |x_L - B|)^c$ are thus unsuccessful.

Very good fits to all the x_L - distributions are obtained using the parametrisation $\frac{d\sigma}{dx_L} \sim \frac{(1-x_1)^\alpha (1-x_2)^\beta}{x_1 + x_2}$. A fit of this form is motivated by the parton models. This can be seen by substituting $x_1 q(x_1) = A(1-x_1)^\alpha$, $x_2 q(x_2) = B(1-x_2)^\beta$ (A, B constants) in the differential cross-section formula for ψ production, eqn 1.14. Thus, for the case of the ψ(and ψ'), the functions $(1-x_1)^\alpha$, $(1-x_2)^\beta$ can be directly interpreted as the momentum distribution functions of the colliding partons from the beam and target. (The momentum distribution function is just $xq(x)$, where $q(x)$ is the probability distribution function.) This direct interpretation is not possible for the continuum case which involves an integration over the mass region; however, the parametrisation is still useful. The fitted functions are shown in figs 4.6-4.8, and the parameters of the

fits, and the values of $\langle x_L \rangle$, are given in table 4.3. (As mentioned in section 3.2.4, the quoted errors include a contribution which reflects the change in results produced by a change in the model used to calculate the acceptance).

Figs 4.9, 4.10 show the ranges of x_1, x_2 covered by the raw data in the ψ and the continuum regions. It can be seen that a good range of x_1 is covered, but that the range of x_2 is rather limited ($x_2 \lesssim 0.4$), making the determination of the momentum distribution function for the target $(1-x_2)^{\beta}$, less reliable.

Another feature is that the x_L-distribution for the ψ is much narrower than for the continuum (this can be seen by comparing the values of the exponents α, β). This feature is also observed in the CIP experiment [1.21]. An attempt to fit the ψ x_L-distribution using the valence quark and antiquark PDF measured by NA3 for the continuum [1.5] is shown in fig 4.11. Clearly the fitted function is much too wide (χ^2 = 800 for 24 d.o.f). This suggests that the partons involved in the ψ production mechanism have much more restricted momentum distributions than those involved in the continuum production; the possibilities being gluons or charmed quarks in the sea. The most likely interpretation is that, at these higher energies, ψ production involves a large proportion of gluon-gluon fusion,(the main arguments against the charmed quark possibility are given in section 1.5.1) However, at the lower energy, 39.5 GeV/c, the shape of the x_L-distribution is found to vary smoothly as a function of mass, including the ψ [1.7], suggesting that ψ production involves a large proportion of quark-anti-quark annihilation at this lower energy. These interpretations would be consistent with the results on the ratio of ψ production by protons to that by antiprotons (section 1.5.1).

With this gluon-gluon fusion interpretation for the higher energies, α, β are the exponents of the gluon PDF for the beam, target. From dimensional counting arguments the values expected for these exponents are $\alpha = 3$ for the pion, and $\beta = 5$ for the nucleon. An analysis of ψ production by real and virtual photons in terms of a photon-gluon fusion model gives $\beta \simeq 5$ for the exponent of the gluon PDF for the nucleon [4.2], and an analysis of ψ production in pN and πN collisions gives $\alpha \simeq 3$ and $\beta \simeq 5$ or 6 [4.2]. The CDHS group, analysing the scaling violation in their neutrino data, find $\beta = 5.6$ [4.3]. The value in table 4.3 of $\beta = 6.9 \pm .7$ is slightly higher than that obtained in these other analyses, (however the rather limited range of x_2 covered, makes its determination less reliable, and this discrepancy is probably not significant), while the value of $\alpha = 2.5 \pm .1$ is in good agreement.

4.4 TRANSVERSE MOMENTUM

The p_T- distributions are corrected for background and acceptance as in the case of the x_L-distributions. The resulting differential cross-section $\frac{1}{p_T} \frac{d\sigma}{dp_T}$ is shown for the ψ, ψ' and continuum in figs 4.12-4.14.

The distributions were first fitted using a simple gaussian form: $\frac{1}{p_T} \frac{d\sigma}{dp_T} \sim \exp(-bp_T^2)$. This parametrisation provides a reasonable fit to the data for the lower p_T values, but then falls away too quickly. This feature is also observed in the NA3 experiment [1.20]. The parameters of the fits are given in table 4.4. Much better fits are obtained with the parametrisation: $\frac{1}{p_T} \frac{d\sigma}{dp_T} \sim (1+(\frac{p_T}{B})^2)^{-C}$ which can cope well with the whole range of p_T. The parameters of these fits are given in table 4.4, and the fitted functions are shown in figs 4.12-4.14

The small dip towards $p_T = 0$ for the continuum data is not understood. It is already evident in the raw distributions and is probably not a result of an incorrect acceptance calculation. It becomes more significant as the mass range increases from 3.8-4.8 GeV/c^2 to 4.8-8.8GeV/c^2. NA3 study $\frac{1}{p_T}\frac{d\sigma}{dp_T}$ for the continuum in various mass regions (4.1-5, 5-6, 6-8.5 GeV/c^2) and here too there is a flattening off and eventually a small dip towards $p_T = 0$ as the mass range increases [1.5].

The values of $\langle p_T \rangle$ and $\langle p_T^2 \rangle$ are given in table 4.5. Similar values are obtained in the other experiments at these energies. If the p_T of the muon pair is due entirely to the(independent) sum of the intrinsic k_T of the partons, then $\langle p_T^2 \rangle = \langle k_{T_1}^2 \rangle + \langle k_{T_2}^2 \rangle$. Assuming equal gaussian distributions for both k_T gives $\langle k_T \rangle$ = 750-850 MeV/c ($\langle k_T \rangle = \frac{1}{2}\sqrt{\pi \langle k_T^2 \rangle}$ for a gaussian distribution). These values are much larger than might be expected from the simple estimates mentioned in section 1.2.4. Other contributions to this p_T may come from the effect of any partons produced in the final state of the subprocess, recoiling against the muon pair, as mentioned in section 1.3.2. (A ψ produced via, for example, a $\chi(3.55)$, may also have a contribution to its p_T, from the decay to $\psi\gamma$, of up to 0.4 GeV/c).

4.5 ANGULAR DISTRIBUTIONS

The angular distribution of a muon in the parton-parton CM frame gives information on the production mechanism of the muon pair. Unfortunately, if the partons have some intrinsic transverse momentum, then it is only possible to estimate the original parton-parton axis from the initial hadron directions. One method is to use the beam direction ("Gottfried-Jackson (GJ)axis") and another is to use the axis which bisects the beam and reverse of the target direction ("Collins-

Soper (CS) axis"). These axes and their corresponding angles are shown in fig 4.15. In fig 4.16, where ($\cos\theta_{CS} - \cos\theta_{GJ}$) is plotted as a function of the muon pair p_T, it can be seen how the agreement between these two estimates improves as the p_T of the muon pair decreases. In the context of a parton model, the Collins-Soper axis is the most natural choice, as it treats each parton equally on average, and it is this axis and its corresponding angle which are used in the analysis here.

The corrected angular distribution for the ψ, ψ' and continuum is shown as a function of $|\cos\theta_{CS}|$ in figs 4.17-4.19. The ψ, ψ' distributions are reasonably well fitted using a flat function, while the continuum is reasonably well fitted using the function $1+\cos^2\theta_{CS}$. These features (for the ψ and continuum) are observed in the other experiments. The most important point is the difference between these two shapes; the continuum distribution being consistent with the quark-antiquark DY mechanism, while the ψ, ψ' distributions clearly require some other mechanism which leads to an essentially isotropic decay (such as gluon-gluon fusion, or production via an intermediate χ state).

No deviation from a flat azimuthal angular ϕ_{CS} distribution is found for the ψ, ψ' or continuum.

4.6 SUMMARY

The main results from the data on the properties of the muon pairs, and their interpretation in terms of the models are:

(i) The small value for the ratio of ψ' to ψ production. There is a difference in production mechanism, perhaps explained by some ψ production occurring via intermediate χ states.

(ii) The narrowness of the ψ x_L-distribution. A large proportion of ψ production at the higher energies occurs via gluon-gluon fusion, and the momentum distribution functions of the gluons can thus be estimated for the pion and the nucleon.

(iii) The large values of $\langle p_T \rangle$. Perhaps there is a contribution to the p_T of the muon pair from its recoil against some parton produced in the subprocess.

(iv) The difference between the angular distributions. The continuum angular distribution is compatible with the DY quark-antiquark mechanism, while those of the ψ, ψ' require some mechanism which leads to isotropic decay, perhaps gluon-gluon fusion or production via an intermediate χ state.

References

4.1 Particle Data Group, Rev. Mod. Phys. 52 (1980).

4.2 V.Barger, W.Keung, R.Phillips, Phys. Lett. 91B (1980) 253,
Z. Physik C6 (1980) 169.

4.3 A.Savoy-Navarro, Paper submitted to: Int. Conf. on Neutrinos,
Bergen (1979).

Tables

Figures

4.1 NUMBER OF MUON PAIRS AT VARIOUS BEAM MOMENTA.

BEAM MOMENTUM GeV/c	NUMBER OF MUON PAIRS
175	4 635
185	16 032
192.5	26 549
195	12 020
197.5	3 398
TOTAL	62 634

4.2 NUMBER OF MUON PAIRS IN VARIOUS MASS REGIONS.

MASS REGION GeV/c^2	NUMBER OF MUON PAIRS	
2.5 - 2.9	13 477	
2.9 - 3.3	43 232	
3.3 - 3.6	2 095	
3.6 - 3.8	1 407	OPPOSITE SIGN
3.8 - 4.8	1 439	
4.8 - 8.8	674	
8.8 -11.5	46	
2.5 -11.5	264	LIKE SIGN
TOTAL	62 634	

4.3 PARAMETERS OF FITS TO x_L DISTRIBUTIONS; VALUES OF $\langle x_L \rangle$.

MASS REGION GeV/c^2	α	β	χ^2/d.o.f.	$\langle x_L \rangle$
ψ (2.9-3.3)	2.5±.1	6.9±.7	15/22	0.14±.01
ψ' (3.6-3.8)	2.1±.5	4.2±2.0	22/19	0.11±.03
CONTINUUM (3.8-8.8)	1.8±.2	4.2±1.0	30/24	0.15±.02

4.4 PARAMETERS OF FITS TO p_T DISTRIBUTIONS.

MASS REGION GeV/c^2	b (GeV/c)$^{-2}$	χ^2/d.o.f.	B GeV/c	C	χ^2/d.o.f.
ψ (2.9-3.3)	0.74±.02	96/37	2.5±.2	6.3±.8	14/36
ψ' (3.6-3.8)	0.81±.08	20/27	1.9±.8	4.0±2.5	18/26
CONTINUUM (3.8-8.8)	0.62±.03	51/37	3.1±.5	7.1±2.0	43/36

4.5 VALUES OF $\langle p_T \rangle$, $\langle p_T^2 \rangle$.

MASS REGION GeV/c^2	$\langle p_T \rangle$ GeV/c	$\langle p_T^2 \rangle$ (GeV/c)^2
ψ (2.9-3.3)	1.05±.01	1.49±.01
ψ' (3.6-3.8)	1.09±.05	1.69±.05
CONTINUUM (3.8-8.8)	1.17±.03	1.83±.03

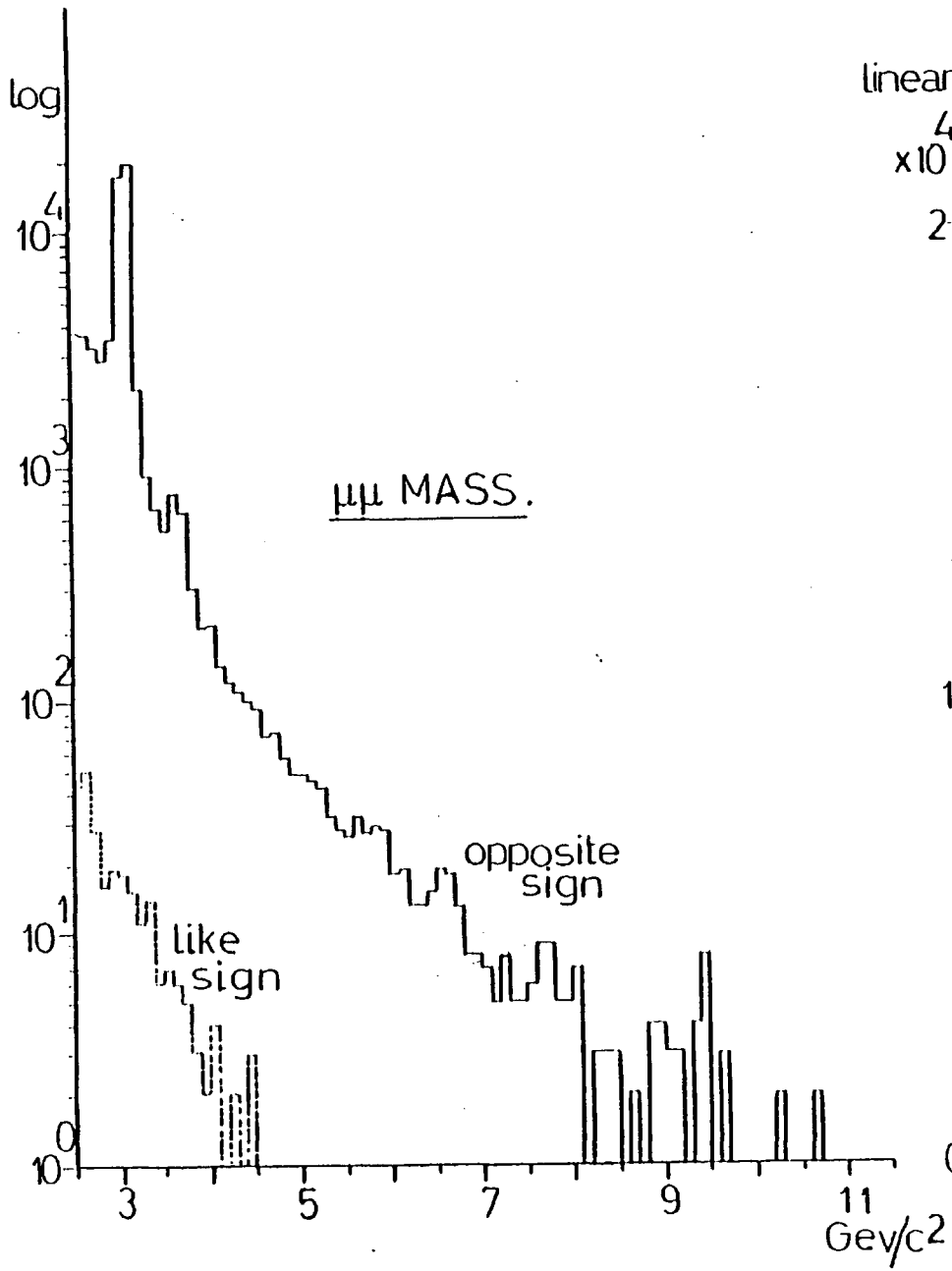
log
10^4
10^3
10^2
10^1
10^0
μμ MASS.
opposite sign
like sign
3
5
7
9
11
Gev/c²

4.1

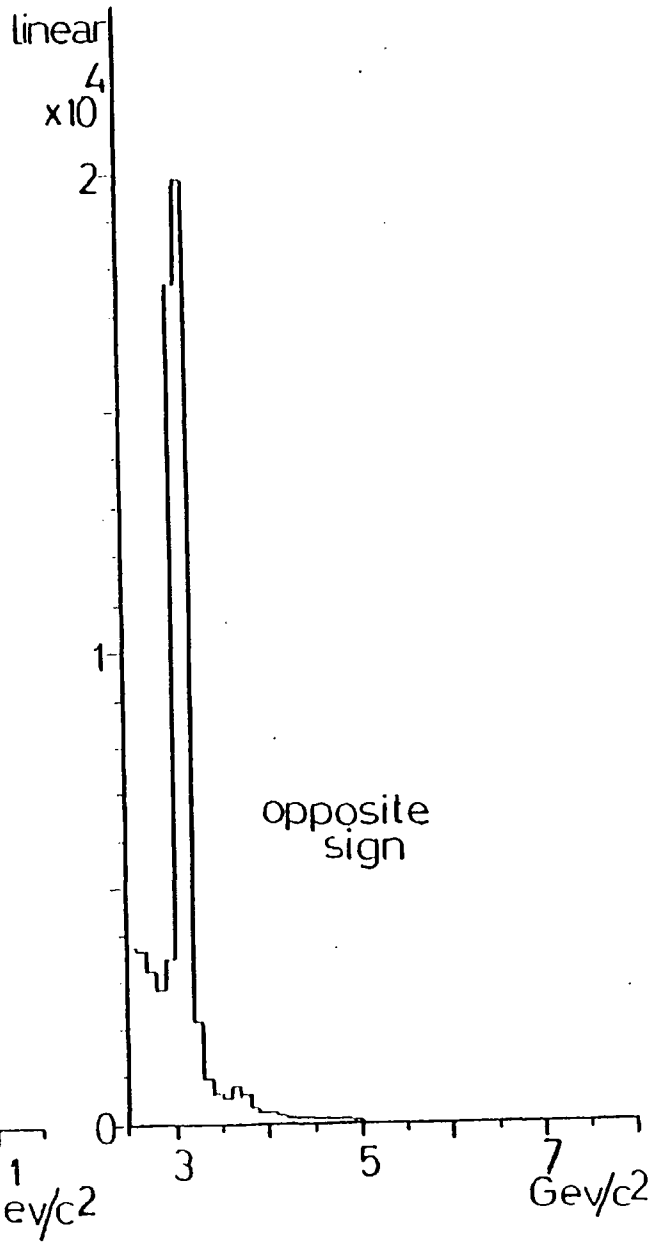
linear
x10⁴
2
1
0
opposite sign
3
5
7
Gev/c²

4.2

$\mu^+\mu^-$ MASS.

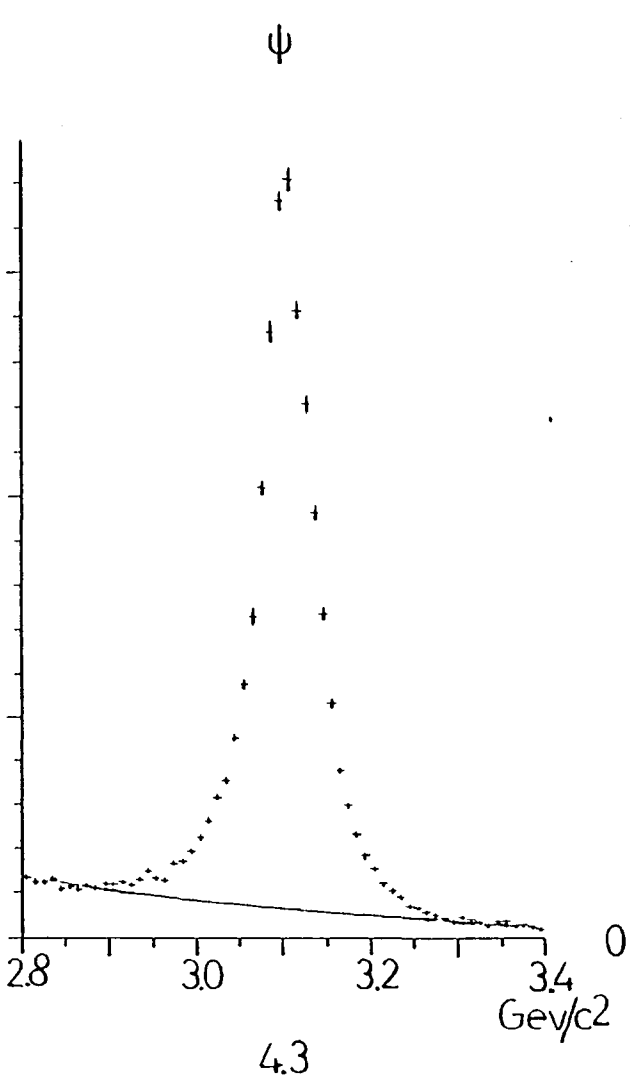

4.3

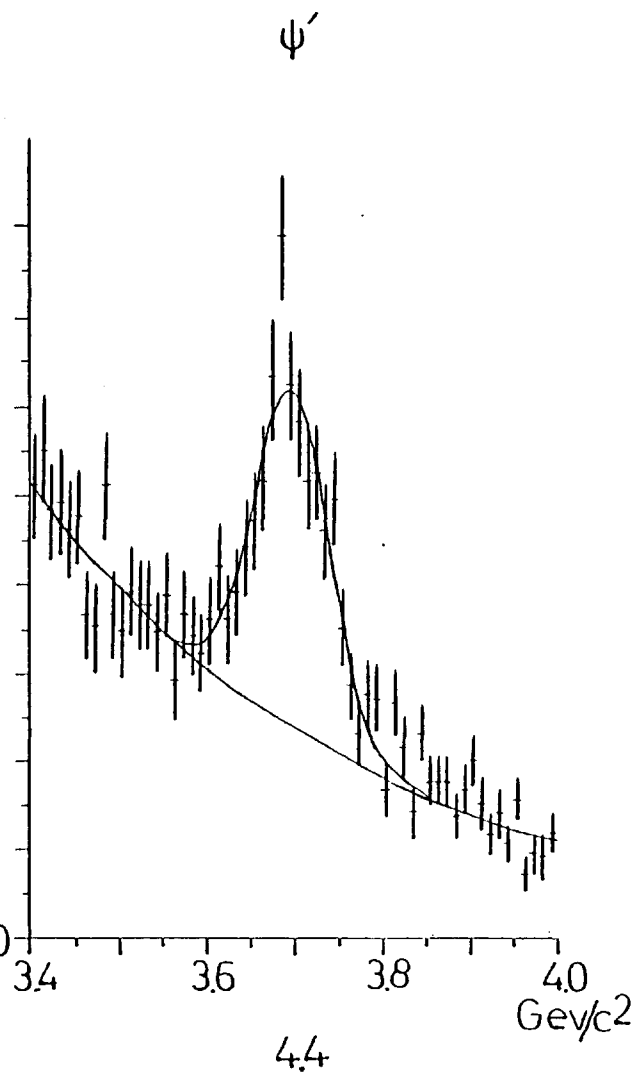

4.4

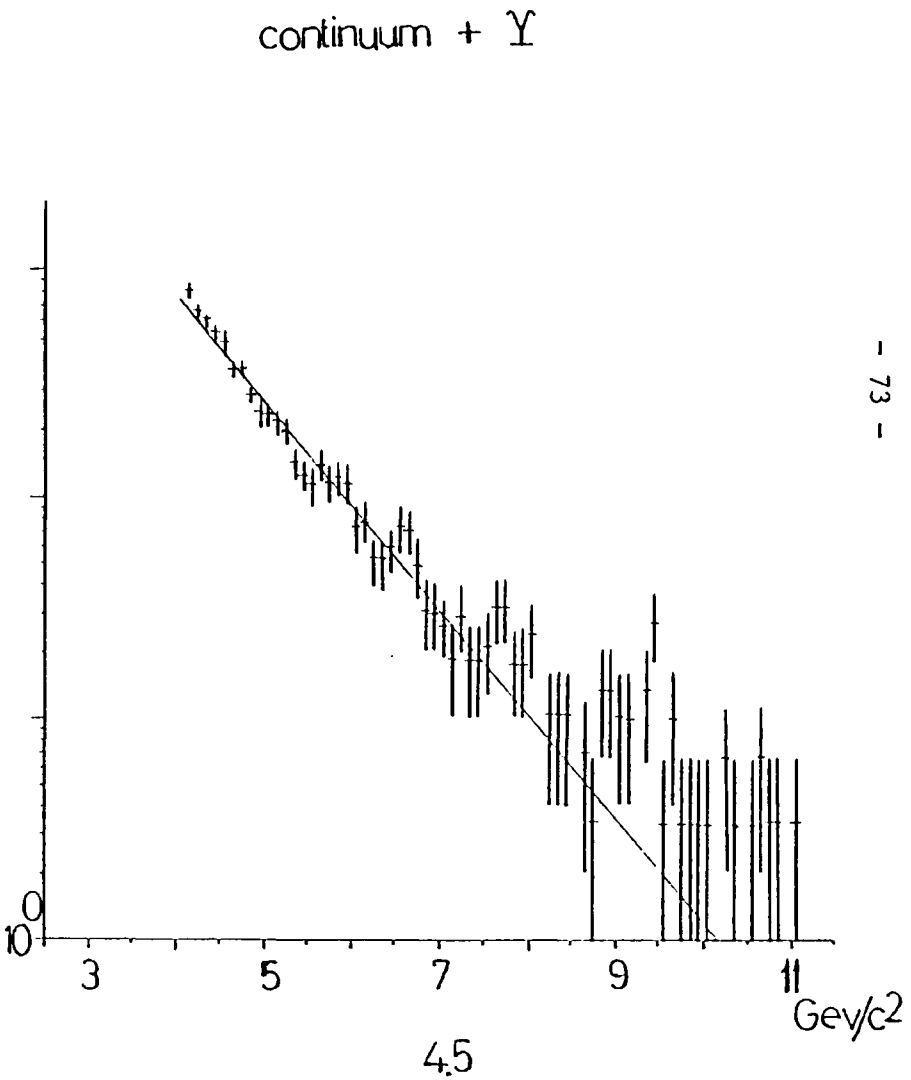

4.5

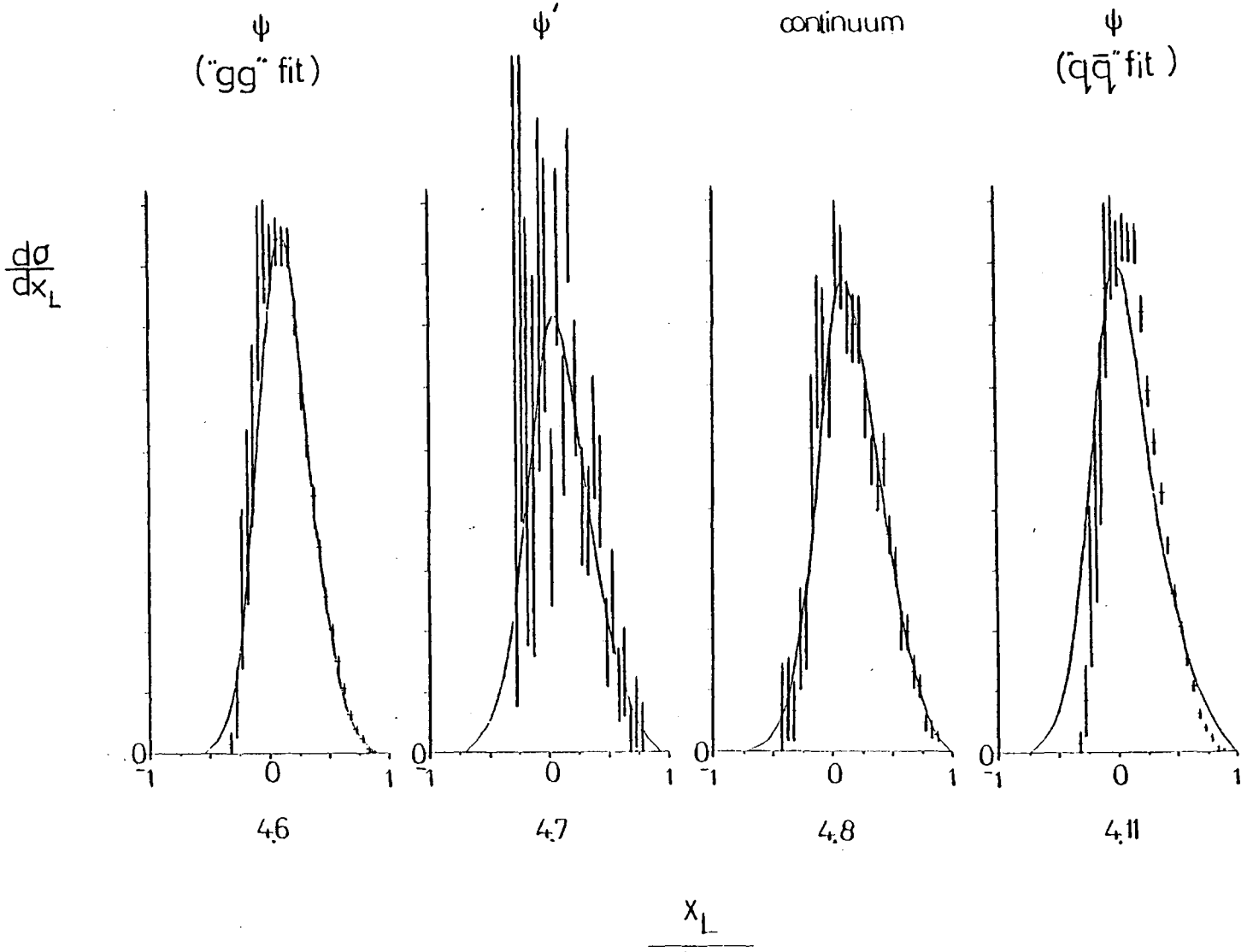
ψ
("gg" fit)
ψ'
continuum
ψ
("qq̄" fit)
dσ/dx_L
0
-1
0
1
4.6
4.7
4.8
4.11
x_L

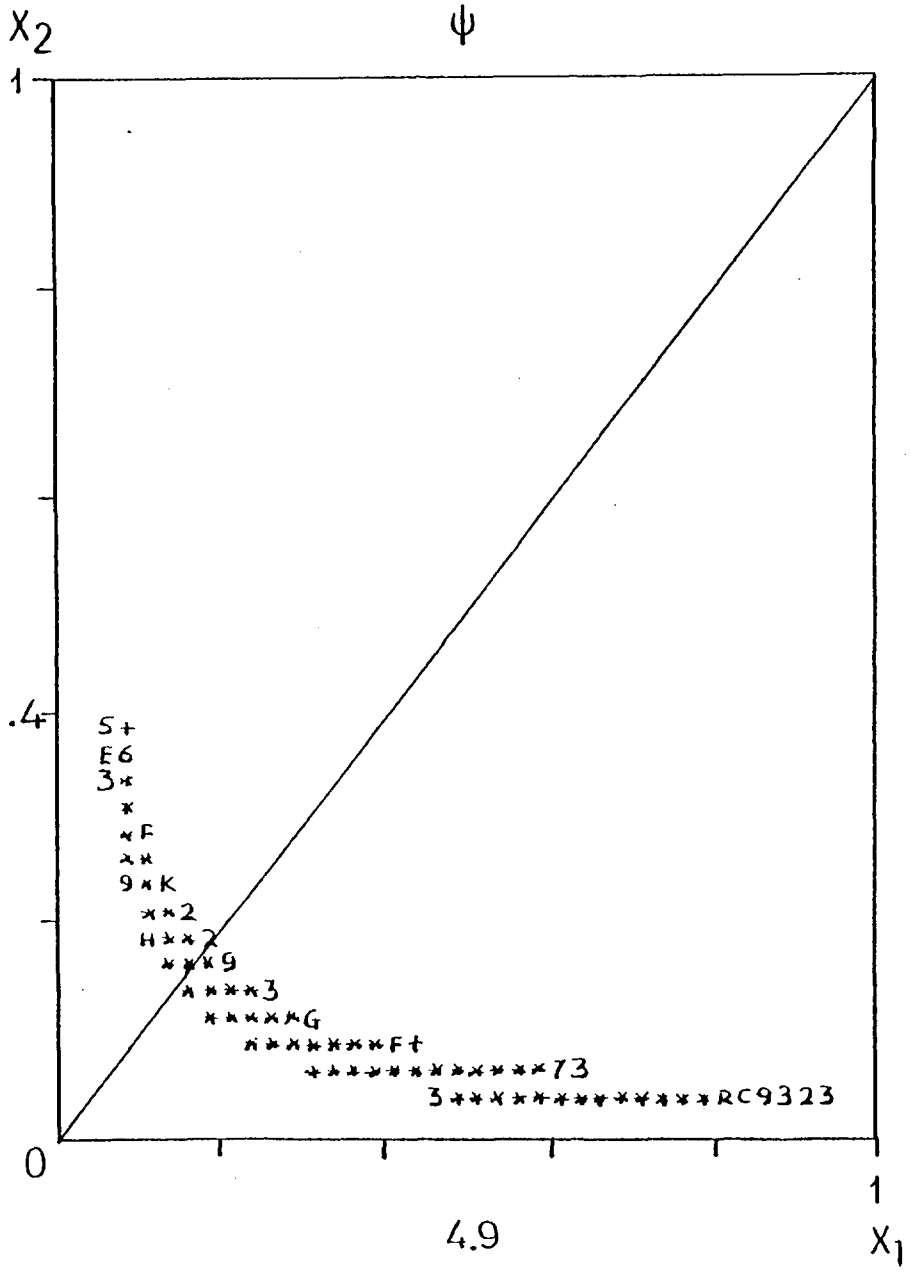

4.9

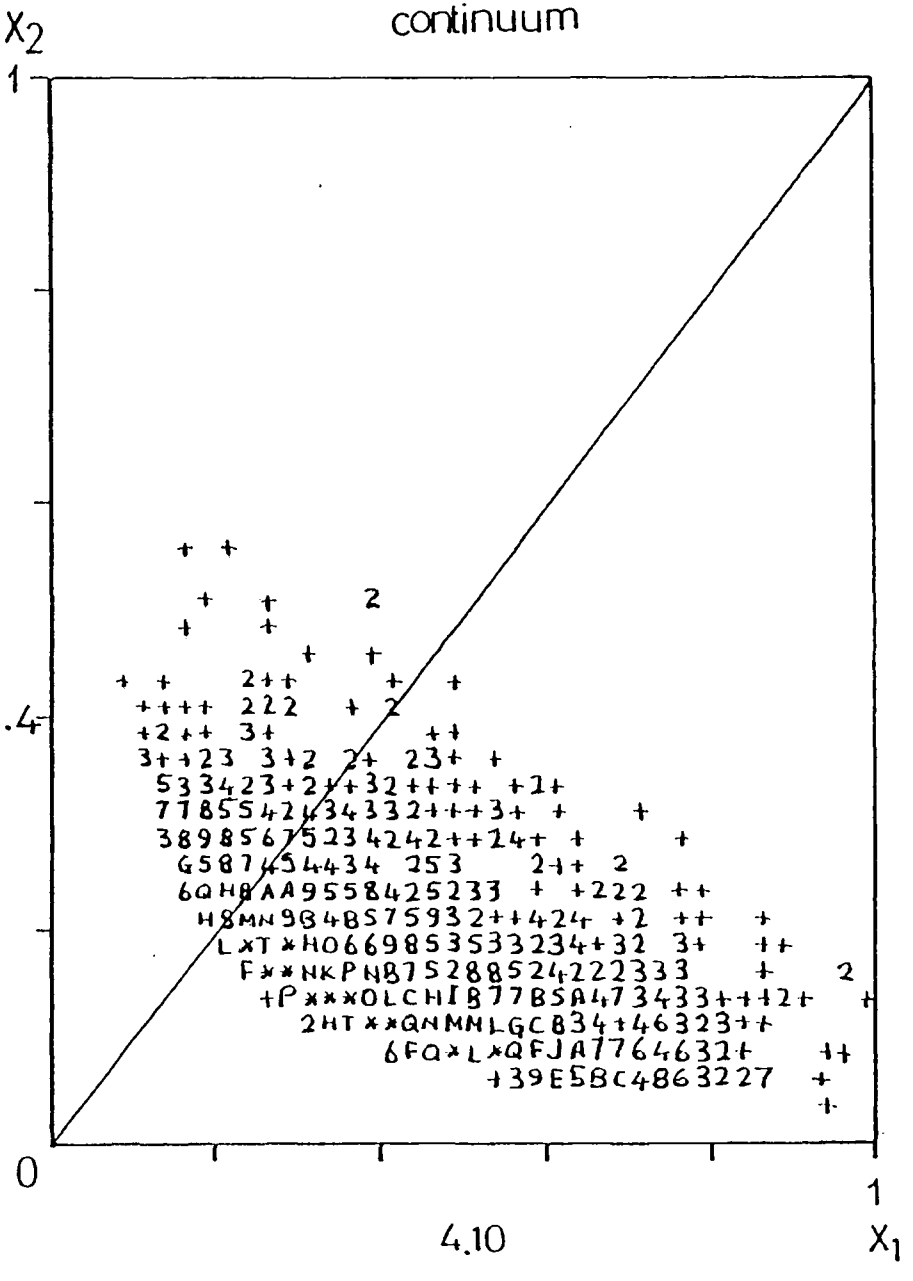

4.10

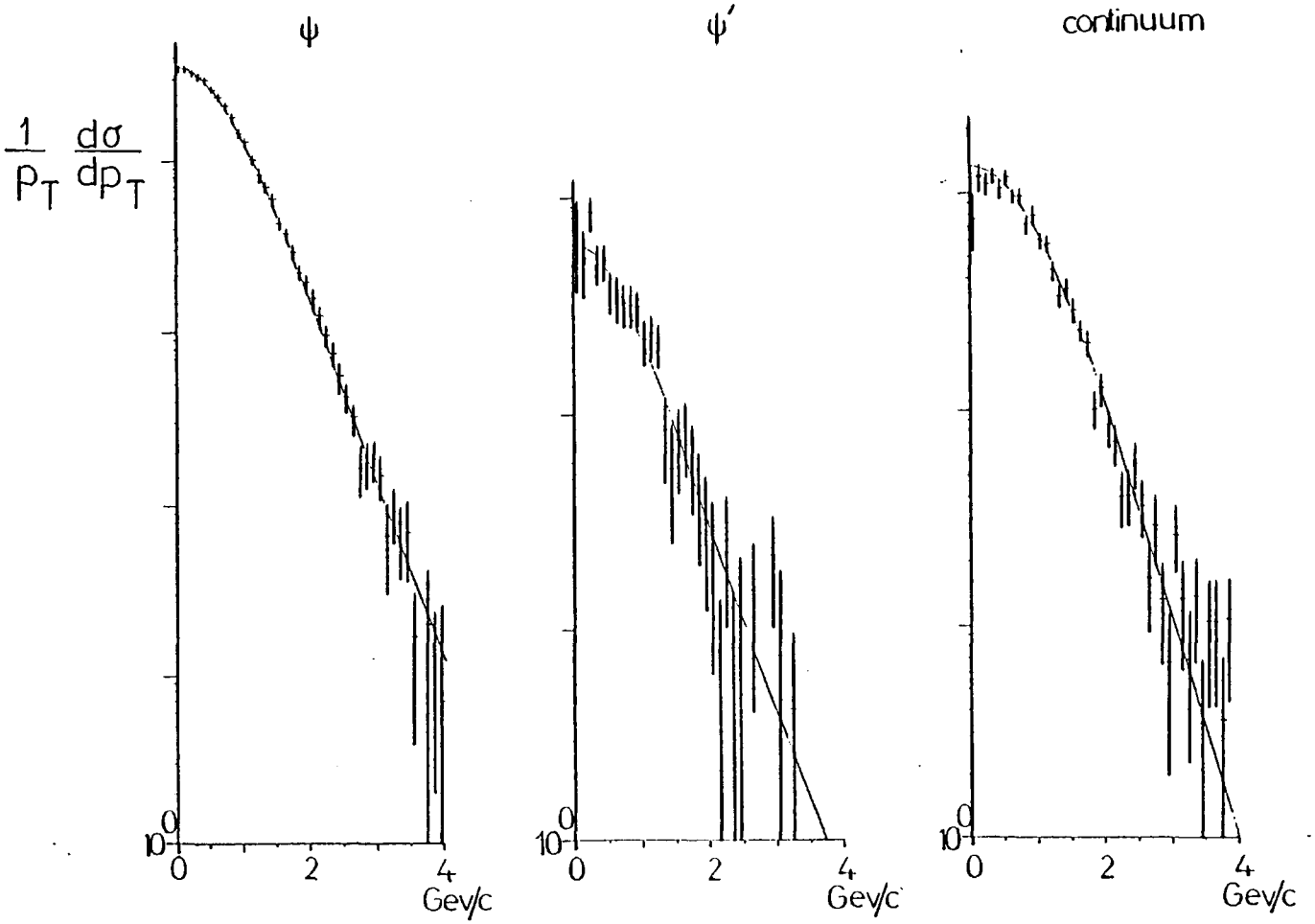
ψ
ψ′
continuum
1/P_T dσ/dp_T
10^0
0
2
4
Gev/c
4.12
4.13
4.14
P_T

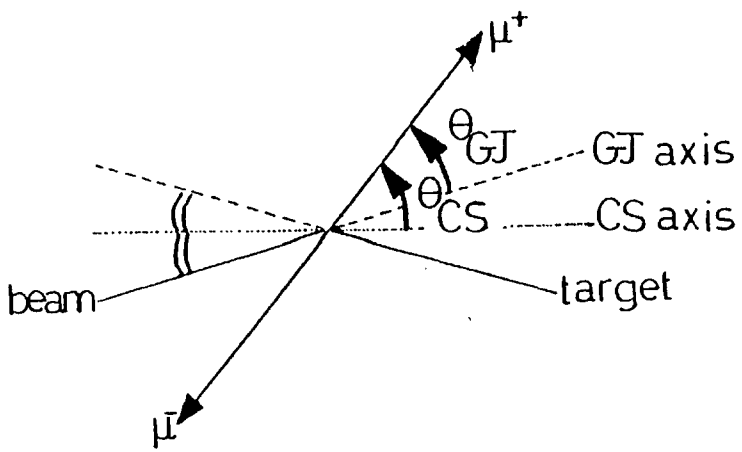
μ+
θGJ
GJ axis
θCS
CS axis
beam
target
μ̄

4.15

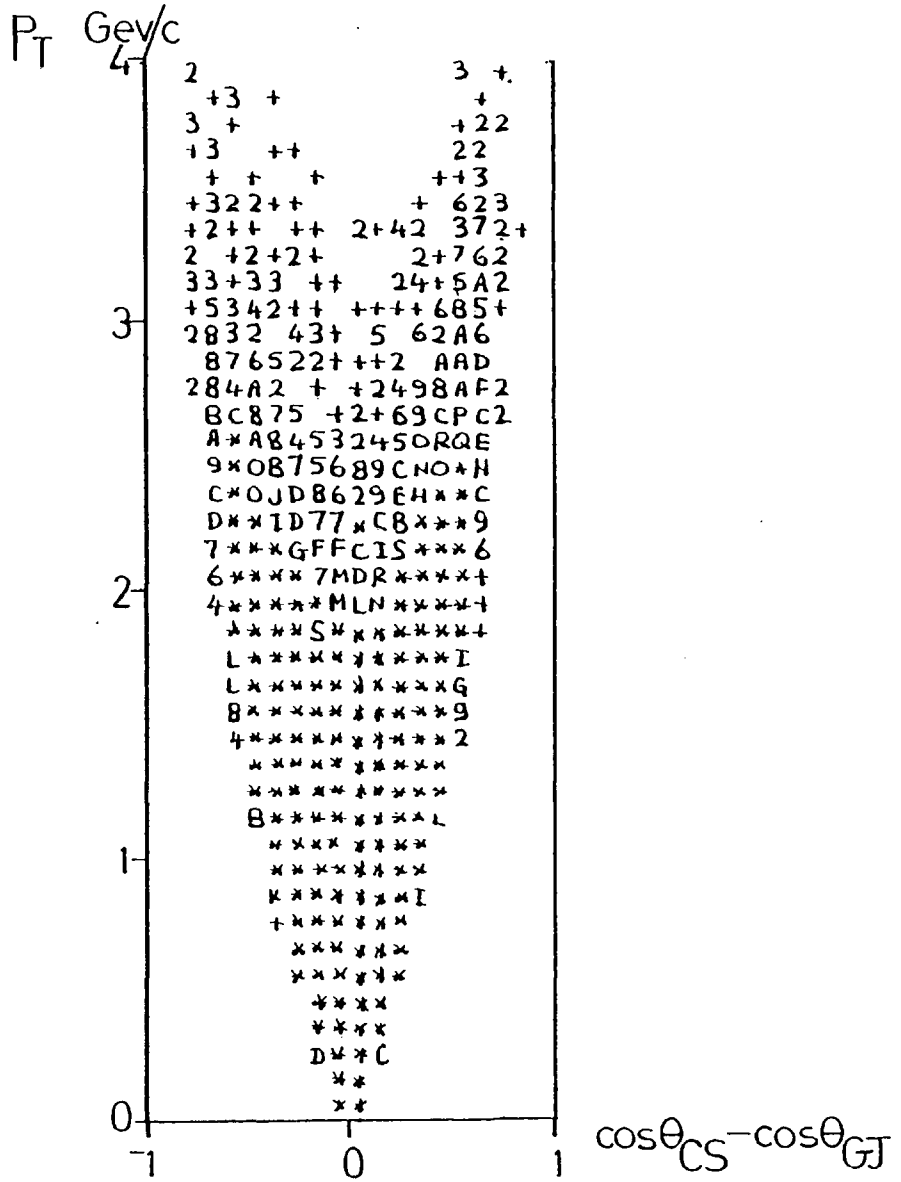
PT Gev/c
4
3
2
1
0
-1
0
1
cosθCS−cosθGJ

4.16

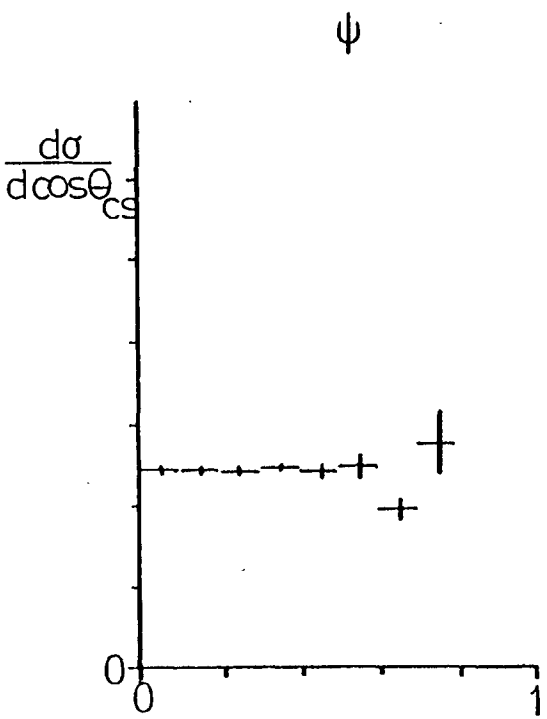

4.17

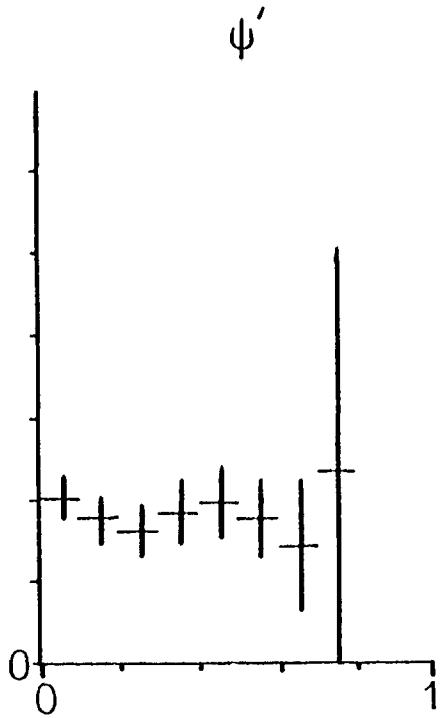

4.18

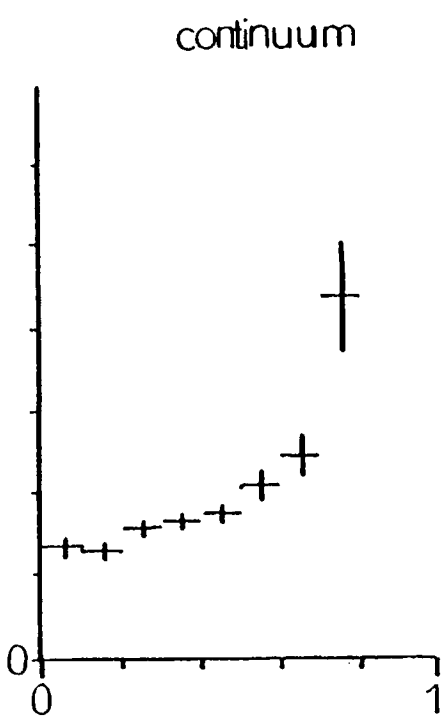

4.19

$|\cos\theta_{CS}|$

CHAPTER 5

PROPERTIES OF THE ASSOCIATED HADRONS

5.0 INTRODUCTION

In this chapter, data on the multiplicity, kinematical distributions and quantum numbers of the hadrons produced in association with the muon pairs are presented. Emphasis is given to the forward direction for reasons discussed later (section 5.1.5). The data are discussed in the context of the parton models which were described in chapter 1 and used in the discussion of the properties of the muon pairs in chapter 4.

5.1 PRELIMINARIES

5.1.1 Monte-Carlo

The parton model monte-carlos (section 3.2), used in the study of the properties of the muon pairs, were adapted to include the generation of associated hadrons. The average number of charged particles $\langle n \rangle$, produced in ordinary $\pi^- p$ interactions, with beam momentum between 50 and 205 GeV/c, has been measured in bubble chamber experiments and fitted [5.1] with the formula:

$$\langle n \rangle = 2.02 \ (\sqrt{s})^{0.461} \qquad (\sqrt{s} \text{ in GeV}) \qquad (5.1)$$

This formula was used to determine the average number of charged particles $\langle n \rangle$ to be generated in the monte-carlo, by calculating the appropriate $\sqrt{s}$ available, once the muon pair had been generated. (In fact, all particles generated were pions). The number of pions actually generated in a given event was then chosen from a poisson

distribution with mean 1.5 x <n> (the factor 1.5 was used to allow for the generation of neutrals). This number of pions (π^+, π^-, π^o with equal probability) was then generated with momenta distributed according to the remaining available phase-space (conserving four-momentum).

Each charged pion generated at this kinematics stage was then tracked through the apparatus and required to be detected in a minimum number of chambers (this meant being within the outer limits, but outside the beam-killer zone (section 2.2.3)). Neutral pions, although possibly detected in the calorimeter, are not used in this analysis of the data. The beam-killers were lined up so as to follow the (negative) beam trajectory through the magnetic spectrometer and this resulted in a difference in acceptance for high momentum positive and negative pions in the forward direction. (Unless otherwise explicitly stated, "forward" and "backward" refer to the πN centre of mass (CM) frame). This was the only loss in acceptance in the forward direction. The losses in the backward direction were more serious, just due to the smaller solid angle covered there by the spectrometer. The acceptance was $\simeq$ 100% for charged pions with CM rapidity y_{CM}, between -0.5 and +1.5, but fell to < 10% for y_{CM} <-1.6 and y_{CM} >+3.0.

Corrections for acceptance as a function of y_{CM} and q_T (the transverse momentum of the pions) could be applied during the analysis if required. Most of the results presented later refer to a comparison of the hadrons accompanying the production of ψ with those accompanying continuum muon pairs, and any such corrections are applied in a similar way to each case. Alternatively, the data can be compared directly with the monte-carlo events in which the muon pair was accepted.

5.1.2 DIF Data

The data are compared with ordinary hadronic interactions at a beam momentum of 192.5 GeV/c, recorded in the same set-up, but with the DIF trigger (section 2.3.1).

5.1.3 Data Sample

For this analysis of the associated hadrons, those events with just one pair of well measured muons of opposite sign (and invariant mass between 2.5 and 8.8 GeV/c^2) are used, so that the four-momentum available for the hadrons is just the total minus that taken by the one muon pair (as in the monte-carlo). The number of such events in each of the various mass regions is given in table 5.1.

5.1.4 Nuclear Effects

The pion-nucleon interactions discussed here took place in a beryllium target, and so the secondary particles produced could reinteract with the other nucleons of the nucleus. A recent review which compares hadron-nucleon and hadron-nucleus interactions [5.2] showed that this is more of a problem for the hadrons which are slow in the laboratory frame (backward in the πN CM frame) than for the fast hadrons (forward).

5.1.5 What to Look For

The data discussed in chapters 1 and 4 on the properties of the muon pairs suggest that, at the energies of this experiment, a large proportion of ψ production occurs via gluon-gluon (gg) fusion, while continuum pair production occurs via valence quark-antiquark ($q\bar{q}$) annihilation. These two production mechanisms are illustrated in

figs 5.1, 5.2. The "spectator" partons (those not directly involved in the muon pair production mechanism) are included in these illustrations as they are involved in the production of the associated hadrons. The bulk of ordinary hadronic interactions at these energies is assumed to occur via collisions of "wee" partons, (quarks and gluons with small values of x).

In ψ production via gg fusion (fig 5.1) both of the valence quarks $d,\bar{u}$ in the pion are spectators and continue to travel forward, essentially along the original beam direction, somehow rearranging themselves ("fragmenting") into the observed hadrons. In continuum pair production via valence $q\bar{q}$ annihilation (fig 5.2) the d quark is the only valence quark which fragments in the forward direction. (This also applies for those ψ produced via valence $q\bar{q}$ annihilation). In all cases, the sea quarks and gluons are also involved in the production of associated hadrons, and since they carry a substantial fraction of the momentum, cannot be neglected.

Similar arguments apply for the backward direction, but due to the poorer acceptance, the larger nuclear effects, and the more complicated fragmenting system (because there is an extra valence quark, and the struck nucleon could be a proton or a neutron), emphasis is given to the fragmentation in the forward direction.

The difference between the systems which fragment in the forward direction for each process, may be observed in several ways:

(i) Colour-octet (ψ via gg) versus colour-triplet (continuum via $q\bar{q}$). The multiplicity in the case of the colour-octet system may be a factor $\frac{9}{4}$ higher than in the case of the colour-triplet, due to the larger coupling to this former system of the soft gluons which materialise into hadrons [5.3].

(ii) Two valence quarks (ψ via gg) versus one valence quark (continuum via $q\bar{q}$). There may be softer longitudinal momentum distributions for the hadrons in the case of the two valence quark system, since the momentum is already divided between these two partons before fragmentation. Perhaps there may also be a difference in the transverse momentum distributions.

(iii) Charge = -1 (ψ via gg) versus charge = $-\frac{1}{3}$ (continuum via $q\bar{q}$). There may be a greater excess of negative over positive hadrons in the case of the charge = -1 system [5.4]. Both fragmenting systems have strangeness = 0.

5.2 MULTIPLICITY

The average total number of charged hadrons produced at the main vertex $\langle n \rangle_{TOTAL}$, for the ψ, continuum and DIF data, and for the ψ and continuum monte-carlos, is given in table 5.2. The average number of forward charged hadrons $\langle n \rangle_{FORWARD}$ for each process is also given. Unless otherwise explicitly stated all hadrons are assumed to be pions for the calculation of kinematical variables. A few points should be noted concerning these multiplicities.

(i) The values given are not corrected for acceptance. The average acceptance correction factor to be applied to the data in the forward direction is small ($\simeq$ 1.1), while in the backward direction it is much larger ($\simeq$ 1.4) due to the poorer acceptance.

(ii) In the data and monte-carlos the massive muon pairs are produced with $\langle x_L \rangle > 0$. This means that, in order to conserve four-momentum, there is more phase-space available for the associated hadrons in the backward direction than in the forward direction.

In the monte-carlos, the ratio of the number of pions generated in the backward direction to that in the forward direction is ≈ 1.4, just due to this fact.

(iii) The formula (eqn. 5.1) used to determine the average number of charged particles to be generated in the monte-carlos was derived from $\pi^- p$ interactions measured in bubble chamber experiments. In the WA11 data however, the nuclear effects in the beryllium target may produce a slightly higher multiplicity (more important in the backward direction).

(iv) In $K^- p$ interactions at 110 GeV/c measured in a bubble chamber experiment [5.5], it was found that $\langle n \rangle_{FORWARD} \simeq 1.2 \langle n \rangle_{BACKWARD}$, so that even when points (i) - (iii) are taken into consideration it is still not expected that $\langle n \rangle_{FORWARD} = \frac{1}{2}\langle n \rangle_{TOTAL}$.

Table 5.2 shows that the multiplicity is lowest for the continuum, higher for the ψ, and highest for the DIF data. The values for the data are slightly higher than for the monte-carlo.

The average number of secondary V-ZERO vertices $\langle n \rangle_{V\text{-}ZERO}$ (from decays of neutrals) for the ψ, continuum and DIF data is also given in table 5.2. These values follow the trend of the charged multiplicities so that the ratio $\langle n \rangle_{V\text{-}ZERO} / \langle n \rangle_{TOTAL}$ is the same (to within $\pm$ 5%) for each process.

Are the different values of $\langle n \rangle_{TOTAL}$ (and $\langle n \rangle_{FORWARD}$) for the various processes simply explained by the amount of energy available for the production of hadrons? To answer this question, the multiplicity is considered as a function of the new variable $\sqrt{s}_{HAD}$. This s_{HAD} is the square of the four-momentum obtained by subtracting the muon pair four-momentum from the total πN four-momentum, (giving the four-momentum available for the production of hadrons). For the DIF data, $\sqrt{s}_{HAD} \equiv \sqrt{s}$.

In the πN CM frame the total πN four-momentum P^μ is:

$$P^\mu = (\sqrt{s}\ , 0, \underline{0}) \qquad (5.2)$$

and the muon pair four-momentum Q^μ is:

$$Q^\mu = (\sqrt{\tfrac{1}{4}sx_L^2 + p_T^2 + m^2},\ \tfrac{1}{2}\sqrt{s}x_L,\ \underline{p}_T) \qquad (5.3)$$

so that:

$$S_{HAD} \equiv (P^\mu - Q^\mu)^2$$

$$= s\ (1 + \frac{m^2}{s} - \sqrt{x_L^2 + 4(m^2+p_T^2)/s}) \qquad (5.4)$$

The average amount of energy available for the production of hadrons is smallest for the continuum ($\langle\sqrt{s}_{HAD}\rangle$ = 12.8GeV), larger for the ψ ($\langle\sqrt{s}_{HAD}\rangle$ = 14.6 GeV), and largest for the DIF data ($\sqrt{s}$ = 19.0 GeV), although there is a very large range of overlap between individual values due to the large ranges of m, x_L and p_T covered by the data.

In figs 5.3, 5.4 $\langle n\rangle_{TOTAL}$ (and $\langle n\rangle_{FORWARD}$) are shown as functions of $\sqrt{s}_{HAD}$ for the ψ and continuum data. There is excellent agreement between multiplicities for the two processes over the large range of $\sqrt{s}_{HAD}$. The values for the DIF data (also shown) follow the same trend. Similarly in figs 5.5, 5.6 $\langle n\rangle_{TOTAL}$ (and $\langle n\rangle_{FORWARD}$) are shown for the ψ and continuum monte-carlos. As already noted, the values for the data are slightly higher than for the monte-carlo, but show a very similar trend.

Thus, it seems that the various multiplicities are well explained simply by the amount of energy $\sqrt{s}_{HAD}$ available for the production of hadrons, and show no evidence for a difference between fragmentation of a colour-octet and a colour-triplet system.

5.3 KINEMATICAL DISTRIBUTIONS

5.3.1 Longitudinal Momentum

In figs 5.7, 5.8 the centre of mass rapidity y_{CM} distributions for negative and positive hadrons are shown for the ψ, continuum and DIF data. A few points should be noted concerning all the longitudinal momentum distributions discussed in this section:

(i) The distributions are corrected for acceptance as a function of the q_T and y_{CM} of the hadrons, for y_{CM} between -1.6 and +3.0. Outside this range the corrections are too large and unreliable. (The maximum possible rapidity for pions is $|y_{CM}^{MAX}| \simeq \ln\frac{\sqrt{s}}{m_\pi} \simeq 4.9$, for a beam momentum of 185 GeV/c).

(ii) The distributions are normalised to have total contents = 1, so that it is only their shapes which are being compared, not the absolute values, since the multiplicities are already known to be different (section 5.2). (For example, $\frac{1}{N_+}\frac{dN_+}{dy_{CM}}$ is shown for positive hadrons).

(iii) Error bars are shown only for the continuum data (where the statistics are lowest). As mentioned in section 5.1.5, it is the forward direction which is of most interest in this analysis.

For the forward negative hadrons (fig 5.7), the distributions for the ψ and continuum hadrons are similar, while that for the DIF hadrons is rather harder. For the forward positive hadrons (fig 5.8), the distribution of the DIF hadrons is again the hardest, but now that of the continuum hadrons is slightly harder than that of the ψ hadrons. Since the muon pair takes on average more of the original beam momentum for the continuum than for the ψ ($\langle x_1 \rangle \simeq 0.4$, 0.3 respectively), then just from kinematical considerations it is expected that the longitudinal

momentum distributions of the hadrons should be harder for the ψ than for the continuum (and of course hardest for the DIF data). The x_L-distributions for the data, ($x_L \equiv \frac{p_L}{\frac{1}{2}\sqrt{s}}$, where p_L is the longitudinal momentum of the hadrons in the CM frame) exhibit similar features.

In order to compare the longitudinal momentum distributions after removing any simple kinematical effects due to the muon pair, two new variables are used:

(i) X_{HAD}: The longitudinal momentum of the hadron in the hadron system CM frame $p_{L_{HAD}}$, scaled by (half) the invariant mass of the hadron system $\sqrt{s}_{HAD}$. (This definition is similar to that of x_L, but is now with respect to the hadron system, rather than the πN system).

$$X_{HAD} \equiv \frac{p_{L_{HAD}}}{\frac{1}{2}\sqrt{s}_{HAD}} \qquad (5.5)$$

(For the DIF data, $X_{HAD} \equiv x_L$)

(ii) Z_{HAD}: The longitudinal momentum of the hadron in the πN CM frame p_L, divided by that longitudinal momentum of the beam remaining for the production of hadrons, (defined only for the forward direction).

$$Z_{HAD} \equiv \frac{p_L}{\frac{1}{2}\sqrt{s}(1-x_L)} = \frac{x_L}{1-x_L} \qquad (5.6)$$

(For the DIF data, $Z_{HAD} \equiv x_L$)

In figs 5.9, 5.10 the X_{HAD} distributions for negative and positive hadrons are shown. For the negative hadrons (fig 5.9) the ψ and DIF distributions are similar, while that of the continuum is slightly harder. For the positive hadrons (fig 5.10) this feature is the same. In figs 5.11, 5.12 the Z_{HAD} distributions for negative and positive hadrons

are shown. Again, the distributions for the continuum hadrons are slightly harder than for the ψ hadrons.

Thus, it seems that the longitudinal momentum distributions produced by the fragmentation of the single valence quark system are slightly harder than those produced by the fragmentation of the two valence quarks system.

5.3.2 Transverse Momentum

The distributions of the transverse momentum q_T of the hadrons with respect to the beam axis are very similar for the ψ, continuum and DIF data. All the distributions have an average value $\langle q_T \rangle \simeq 385$MeV/c (to within $\pm$ 5MeV/c), while individual values of q_T extend up to about 10 times this average value.

The longitudinal momentum of the beam remaining for the production of hadrons is $\frac{1}{2}\sqrt{s}(1-x_1)$, which has the average values: 6.5, 5.6, 9.5 GeV/c for the ψ, continuum and DIF data,respectively. Average values for the transverse momentum of hadrons, of 300-400 MeV/c seem to be universal for all hadronic fragmentation systems measured at this momentum scale.

The transverse momentum of the hadrons is discussed in more detail in chapter 6.

5.4 QUANTUM NUMBERS

5.4.1 Charge

The longitudinal momentum distributions for each process are different for negative and positive hadrons. By subtracting the

distribution for negative hadrons from that for positive hadrons, the charge Q distribution is obtained. In fig 5.13, the charge distribution as a function of y_{CM} is shown for the ψ data (where the statistics are highest). The charge distributions for the other processes have similar features. A few points should be noted concerning the charge distributions discussed in this section:

(i) The distributions are corrected for acceptance, as in section 5.3.1.

(ii) The distributions are normalised by dividing by the total number of events, so that the sum of the entries in the distribution gives the average charge per event. (That is,

$$\frac{dQ}{dy_{CM}} = \frac{1}{N_{EVTS}} \left(\frac{dN^+}{dy_{CM}} - \frac{dN^-}{dy_{CM}}\right) \text{ is shown).}$$

The general features of all the distributions are: an excess of negative hadrons in the forward direction leading to a negative charge, the converse in the backward direction, and a crossover at $y_{CM} \simeq 0$. The rise in positive charge in the backward direction is much more rapid than in $\pi^- p$ collisions observed in bubble chamber (H_2) experiments, presumably as a result of the nuclear effects. Again it is the forward direction which is of most interest in this analysis.

The sum of the entries for $y_{CM} > 0$ gives the average charge per event measured in the forward direction $\langle Q \rangle_{FORWARD}$. There are several complications when trying to relate this value to the charge of the original forward fragmenting system.

The case of ordinary hadronic interactions is first discussed. At extreme energies where the interactions are via wee parton collisions, the charges carried by the beam and target should remain in their

respective fragmentation regions, not extending into the neutral central region. By taking the sum (difference) of the charge distributions in $\pi^+ p$ and $\pi^- p$ interactions, the target (beam) fragmentation region can be studied separately. In $\pi^{\pm} p$ interactions at 100 GeV/c it was found in this way [5.6] that both regions extend past $y_{CM} = 0$ by about 2units of rapidity, and there is no neutral central region. The crossover at $y_{CM} \simeq 0$ is just due to the cancellation of the overlapping distributions, which happen to be equal and opposite at this point. The overlap decreases as $\sqrt{s}$ increases; values for $\langle Q \rangle_{FORWARD}$ in $\pi^- p$ (and $K^- p$) interactions [5.7] changing from $\simeq -0.55$ at $\sqrt{s} = 10$GeV to $\simeq -0.70$ at $\sqrt{s} = 20$ GeV, and as a function of $(\sqrt{s})^{-1}$ tending to -1.00 as $\sqrt{s} \to \infty$, (see fig 5.14 which is taken from ref [5.7]).

The case of ψ production via gluon-gluon (gg) fusion should be similar to that of ordinary hadronic interactions via wee parton collisions, except for the different amounts of energy available for the hadrons.

The case of continuum production via quark-antiquark ($q\bar{q}$) annihilation is discussed in the context of the Feynman-Field (FF) model for quark fragmentation [5.8]. The basic idea is that when a quark "a" emerges from an interaction with a large momentum, it creates a colour-field between itself and the other interaction products in which a new quark-antiquark pair "$b\bar{b}$" is formed. Quark "a" then combines with antiquark "$\bar{b}$" to form a meson "$a\bar{b}$", leaving quark "b" to fragment in a similar manner, but with the appropriately reduced momentum. Finally, quark "z" from the last pair "$z\bar{z}$" of the chain, combines with an anti-quark from the fragmentation process of the other interaction products. In continuum pair production via $u\bar{u}$ annihilation, the fragmenting system in the forward direction involves the remaining valence d (= down) quark. Suppose this d quark fragments as in the FF model. When making the

experimental cut at $y_{CM} = 0$ to select hadrons from the fragmentation of the d quark, the final quark "z" of the chain is omitted and its charge "leaks" into the backward direction. The average charge measured for the hadrons in the forward direction is then: $e_d - \langle e_z \rangle$. Suppose that the new quark-antiquark pairs "$b\bar{b}$", ..., "$z\bar{z}$" are: $u\bar{u}$ with probability γ_u, $d\bar{d}$ with probability γ_d, and $s\bar{s}$ with probability γ_s, and that $\gamma_u = \gamma_d \equiv \gamma$ (so that $\gamma_s = 1-2\gamma$). Estimates from K/π ratios measured in various processes suggest $\gamma \simeq 0.40 \rightarrow 0.44$ ($\gamma_s \simeq 0.20 \rightarrow 0.12$) so that the average charge measured from the fragmentation of a d quark is expected to be $\langle Q \rangle_{d-FRAG} \simeq (-0.40) \rightarrow (-0.44)$. In deep inelastic $\bar{\nu}N$ scattering, the fragmentation of a d quark can be studied [5.9]. The average charge in the d quark fragmentation region as a function of W^{-1} (where W is the hadronic CM energy, equivalent to $\sqrt{s}_{HAD}$ of section 5.2) tends to -0.44 as $W \rightarrow \infty$. (See fig 5.15, which is taken from ref [5.9]).

Another complication is that the acceptance correction in the forward direction only extends to $y_{CM} = + 3.0$, whereas $+y_{CM}^{MAX} \simeq + 4.9$. Also, there may be some (small) nuclear effects in the forward direction.

The values of $\langle Q \rangle_{FORWARD}$ for the ψ, continuum and DIF data are given in table 5.3. These values have been corrected for acceptance (geometry) and efficiency (track reconstruction), and include an extrapolation of the charge distribution up to $+y_{CM}^{MAX}$. (This correction for efficiency and extrapolation was the work of other members of the collaboration).

For the DIF data at $\sqrt{s} = 19.0$ GeV, $\langle Q \rangle_{FORWARD} = -0.75$. For comparison, $\langle Q \rangle_{FORWARD}$ as a function of $(\sqrt{s})^{-1}$ in ordinary $\pi^- p$ interactions measured in bubble chamber experiments [5.7] gives a value $\simeq - 0.70$ at this energy (see fig 5.14). For the continuum data with $\langle \sqrt{s}_{HAD} \rangle = 12.8$GeV,

$\langle Q \rangle_{FORWARD} = -0.35$. For comparison, $\langle Q \rangle_{d\text{-}FRAG}$ as a function of W^{-1} in deep inelastic $\bar{\nu}N$ interactions measured in a bubble chamber experiment [5.9] gives a value $\simeq -0.38$ at this energy (see fig 5.15). The corresponding values in table 5.3 are in reasonable agreement with these values (which have been estimated, with errors $\simeq \pm .05$, from the figures taken from these references).

For the ψ data, $\langle \sqrt{s}_{HAD} \rangle = 14.6$ GeV, and the corresponding average charge values at this energy are $\langle Q \rangle_{FORWARD} \simeq -0.65$ in ordinary $\pi^- p$ interactions and $\langle Q \rangle_{d\text{-}FRAG} \simeq -0.39$ in deep inelastic $\bar{\nu}N$ interactions. The measured value in table 5.3 ($\langle Q \rangle_{FORWARD} = -0.52$) lies half-way between these two values. Thus, if a fraction α of ψ production occurs via gg fusion (assuming the fragmentation is similar to that in ordinary $\pi^- N$ interactions) and the remaining fraction $1-\alpha$ occurs via $q\bar{q}$ annihilation (assuming the fragmentation is similar to that in deep inelastic $\bar{\nu}N$ interactions), the above average charge values suggest that $\alpha \simeq 0.5$. This value of α has a rather large error ($\simeq \pm .3$); nevertheless it does at least suggest that both production mechanisms are involved, and is an interesting new technique.

In fig 5.16 the charge distribution as a function of y_{CM} is shown separately for those ψ with $x_L < 0$ and those with $x_L > 0.4$. As the x_L of the ψ changes from $x_L < 0$ to $x_L > 0$, the crossover point (the point where the overlapping beam and target fragmentation regions cancel) shifts from $y_{CM} > 0$ to $y_{CM} < 0$. This reflects the fact that the longitudinal momentum of the ψ is balanced by that of the hadrons.

5.4.2 Strangeness

Charged and neutral strange particles are detected in the WA11 experiment as follows:

(i) Charged kaons. The Cerenkov counter information and special Cerenkov program allow separation of K^- (and $\bar{p}$) from π^-, and K^+ (and p) from π^+, in the laboratory momentum range: 5-25 GeV/c.

(ii) Neutral kaons and lambdas. The invariant mass spectrum for V-ZERO under each of the hypotheses: $K^o \to \pi^+\pi^-$, $\Lambda \to \pi^- p$, $\bar{\Lambda} \to \pi^+\bar{p}$ is shown in figs 5.17-5.19. The acceptance for V-ZERO varies with the distance from production to decay vertex, since close decays are likely to be "absorbed" into the production vertex by the pattern recognition program. The validity of the corrections applied to the number of successful fits to each hypothesis, was checked by observing an exponential decay with the correct mean life.

The average number of each type of strange particle $\langle n \rangle_{STRANGE}$ for each process is given in table 5.4 (the Cerenkov information is not available for the DIF data). To allow for the different amounts of energy available for the production of hadrons in each process, this average number is then divided by $\langle n \rangle_{TOTAL}$ for that process. The resulting values are equal (to within $\pm$ 10%) for each process. This result is also true for just the forward hadrons.

Thus it seems that there is no significant difference between the fraction of strange particles produced in each process. This also indicates that there is no excess charm (which decays to strangeness) in ψ production compared to continuum production.

5.5 SUMMARY

The main results from the data on the properties of the hadrons associated with ψ and continuum muon pairs and ordinary hadronic

interactions, and their interpretation in terms of the various models are:

(i) The multiplicities for the various processes are well explained simply by the amount of energy $\sqrt{s}_{HAD}$ available for the production of the hadrons.

(ii) After the removal of simple kinematical effects due to the muon pair, the longitudinal momentum distributions (in X_{HAD}, Z_{HAD}) are similar for the ψ and DIF hadrons, while slightly harder for the continuum hadrons, perhaps as a result of the different nature of the fragmenting system.

(iii) The fragmenting systems for the various processes all produce hadrons with very similar transverse momentum distributions, with an average value $\langle q_T \rangle \simeq 385$ MeV/c.

(iv) The average charges in the forward direction are consistent with the result that the continuum production occurs via quark-antiquark annihilation, while ψ production occurs via a mixture of gluon-gluon fusion and quark-antiquark annihilation.

(v) The fractions of strange particles produced in the various processes are similar.

References

5.1 D.Fong et al., Nucl. Phys. B102 (1976) 386.

5.2 M.Faessler, CERN EP 81-42.

5.3 S.Brodsky, J.Gunion, Phys. Rev. Lett. 37 (1976) 402.

5.4 S.Brodsky, N.Weiss, Phys. Rev. D16 (1977) 2325.

5.5 R.Gottgens et al., CERN EP 0043R (1980).

5.6 J.Whitmore et al., Phys. Rev. D16 (1977) 3137.

5.7 R.Gottgens et al., Z. Physik C9 (1981) 17.

5.8 R.Field, R.Feynman, Nucl. Phys. B136 (1978) 1.

5.9 J.Berge et al., Nucl. Phys. B184 (1981) 13.

Tables

Figures

5.1 NUMBER OF MUON PAIR PLUS ASSOCIATED HADRON EVENTS IN VARIOUS MASS REGIONS.

MASS REGION GeV/c^2	NUMBER OF EVENTS
2.5 - 2.9	11 596
2.9 - 3.3	40 142
3.3 - 3.8	3 145
3.8 - 8.8	1 913
TOTAL	56 796

5.2 VALUES OF $\langle n \rangle_{TOTAL}$, $\langle n \rangle_{FORWARD}$, $\langle n \rangle_{V\text{-}ZERO}$.

	PROCESS	$\langle n \rangle_{TOTAL}$	$\langle n \rangle_{FORWARD}$	$\langle n \rangle_{V\text{-}ZERO}$
DATA	ψ	6.36	3.59	0.327
	CONTINUUM	5.75	3.12	0.308
	DIF	7.09	4.20	0.350
MONTE-CARLO	ψ	5.77	2.95	-----
	CONTINUUM	5.10	2.38	-----

5.3 VALUES OF $\langle Q \rangle_{FORWARD}$.

PROCESS	$\langle Q \rangle_{FORWARD}$
ψ	-0.52
CONTINUUM	-0.35
DIF	-0.75

5.4 VALUES OF $\langle n \rangle_{STRANGE}$.

PROCESS	K^-	K^+	K^0	Λ	$\bar{\Lambda}$
ψ	0.116	0.172	0.087	0.035	0.027
CONTINUUM	0.105	0.175	0.089	0.030	0.023
DIF	-----	-----	0.093	0.040	0.038

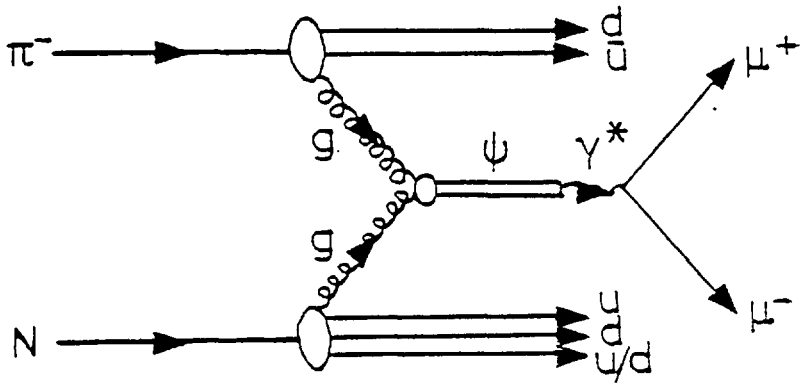

5.1 ψ PRODUCTION VIA
GLUON-GLUON FUSION.

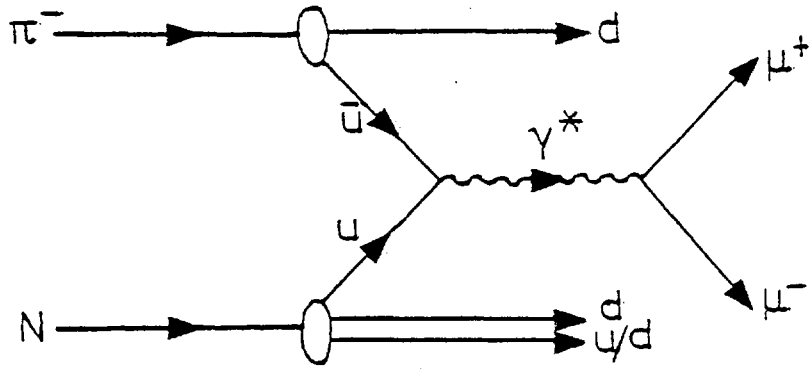

5.2 CONTINUUM PAIR PRODUCTION VIA
VALENCE QUARK-ANTIQUARK ANNIHILATION.

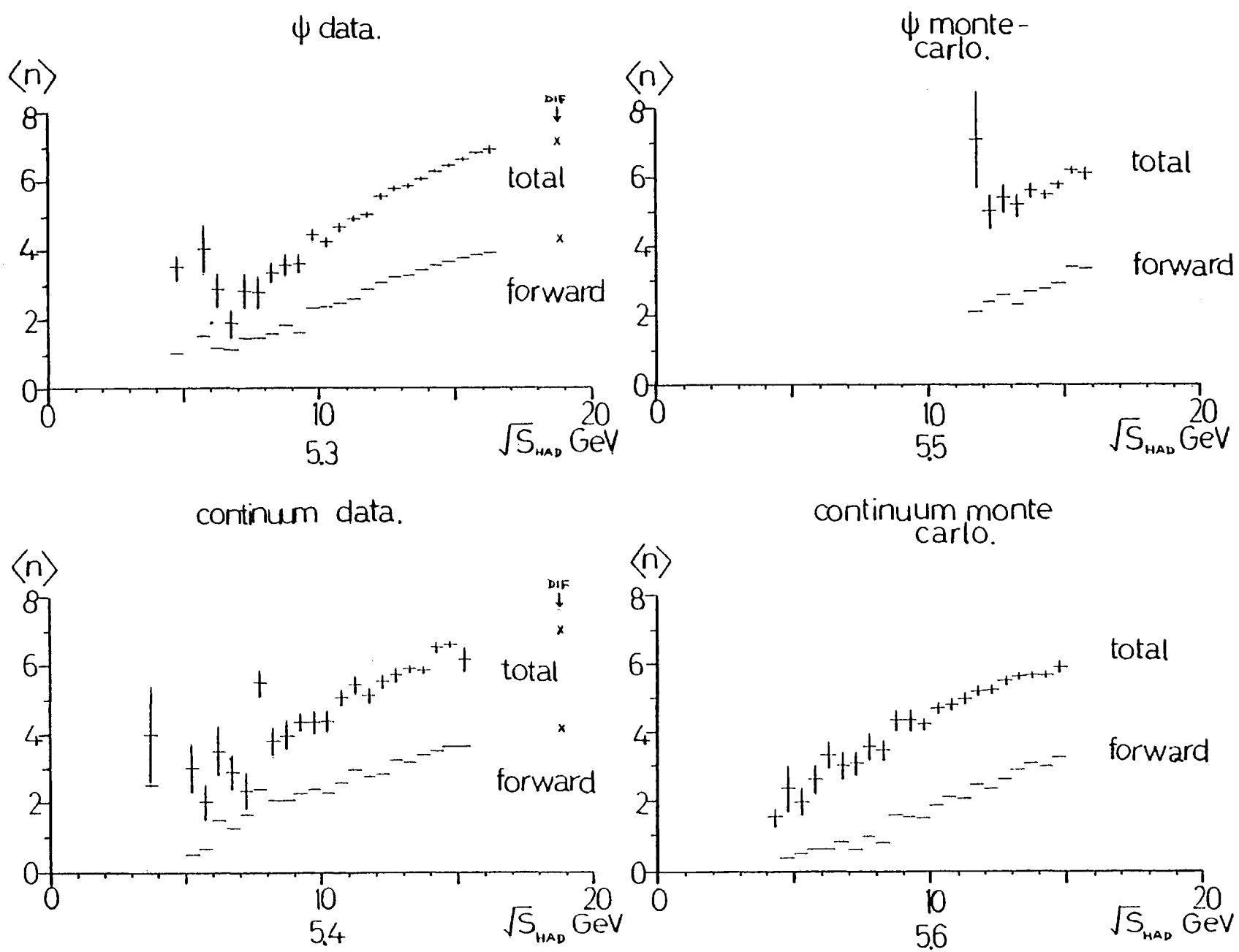
ψ data.
⟨n⟩
DIF
total
forward
0
2
4
6
8
0
10
20
5.3
$\sqrt{S}_{HAD}$ GeV
ψ monte-carlo.
⟨n⟩
total
forward
0
2
4
6
8
0
10
20
5.5
$\sqrt{S}_{HAD}$ GeV
continuum data.
⟨n⟩
DIF
total
forward
0
2
4
6
8
0
10
20
5.4
$\sqrt{S}_{HAD}$ GeV
continuum monte carlo.
⟨n⟩
total
forward
0
2
4
6
8
0
10
20
5.6
$\sqrt{S}_{HAD}$ GeV

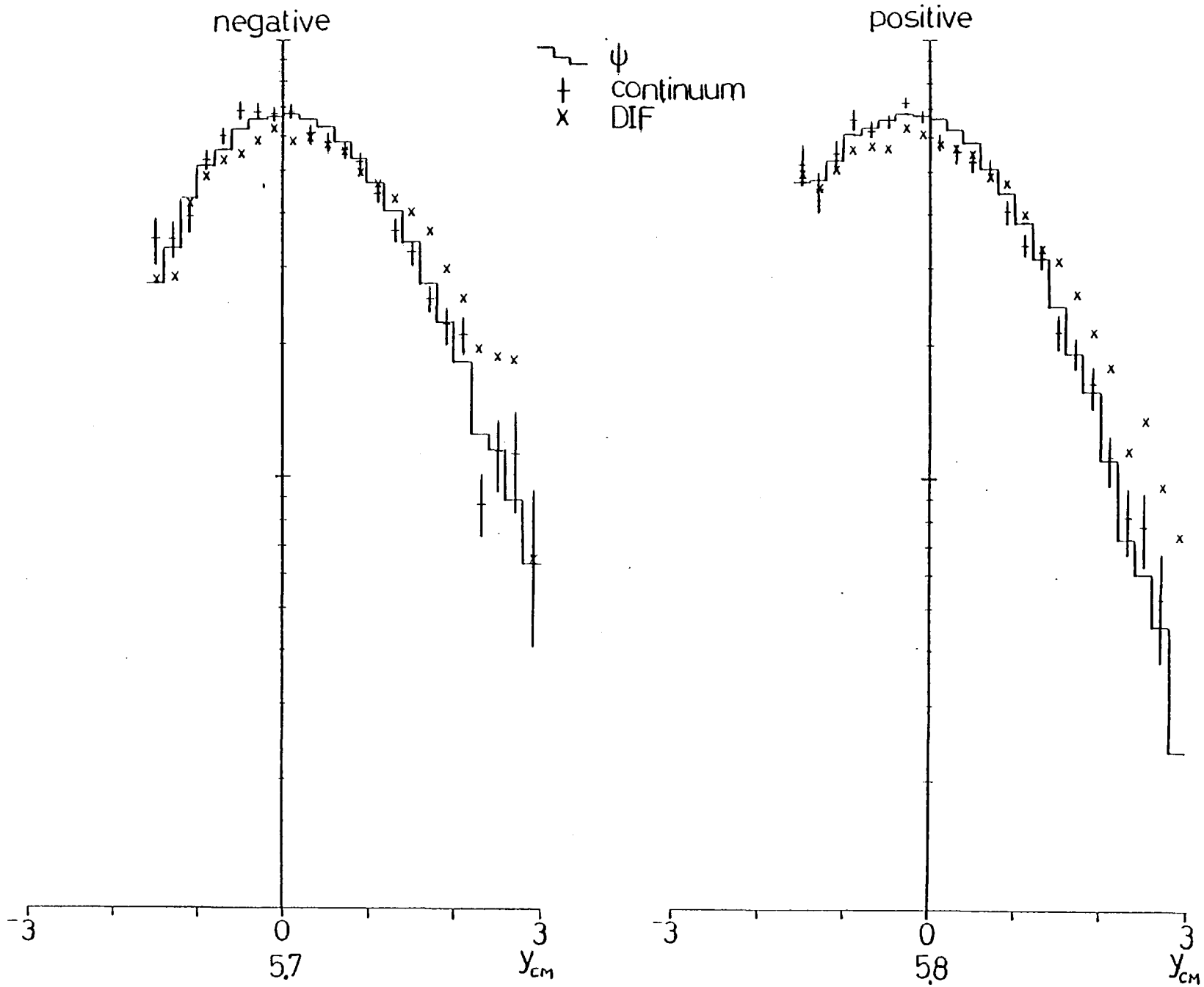
negative
positive
ψ
continuum
DIF
-3
0
3
5.7
5.8
y_{cm}

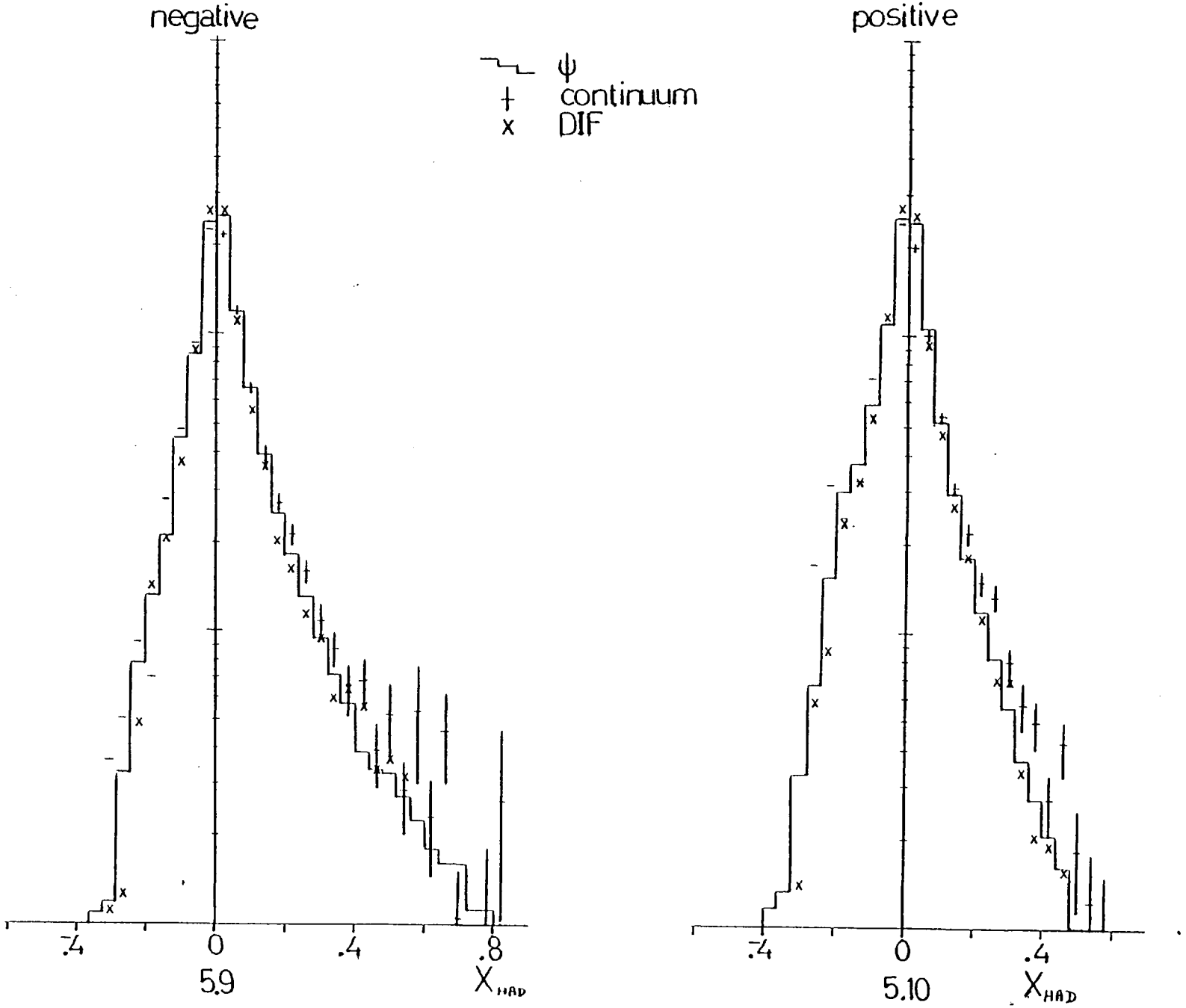
negative
ψ
continuum
DIF
-.4
0
.4
.8
5.9
X HAD
positive
-.4
0
.4
5.10
X HAD

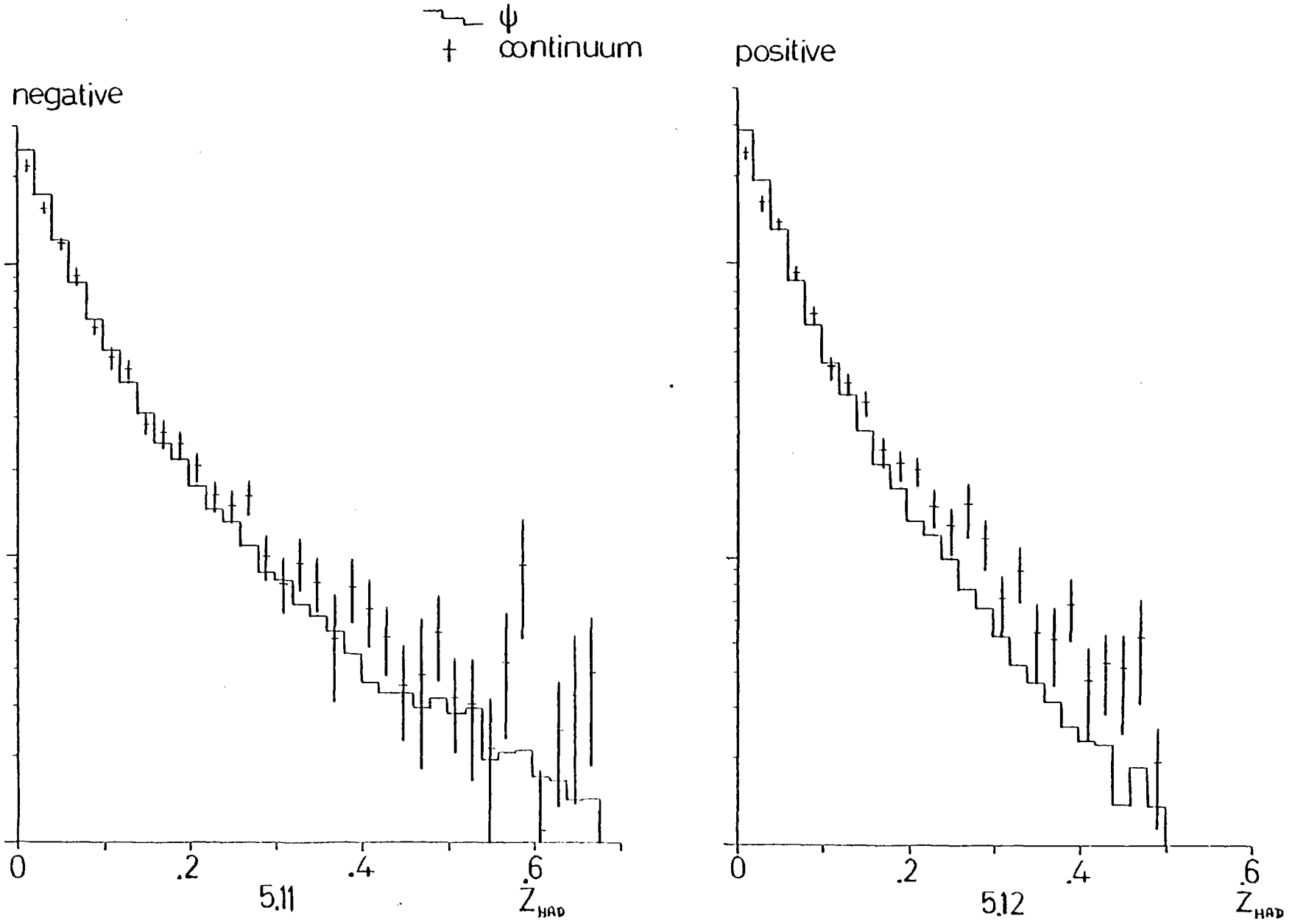

5.11 5.12

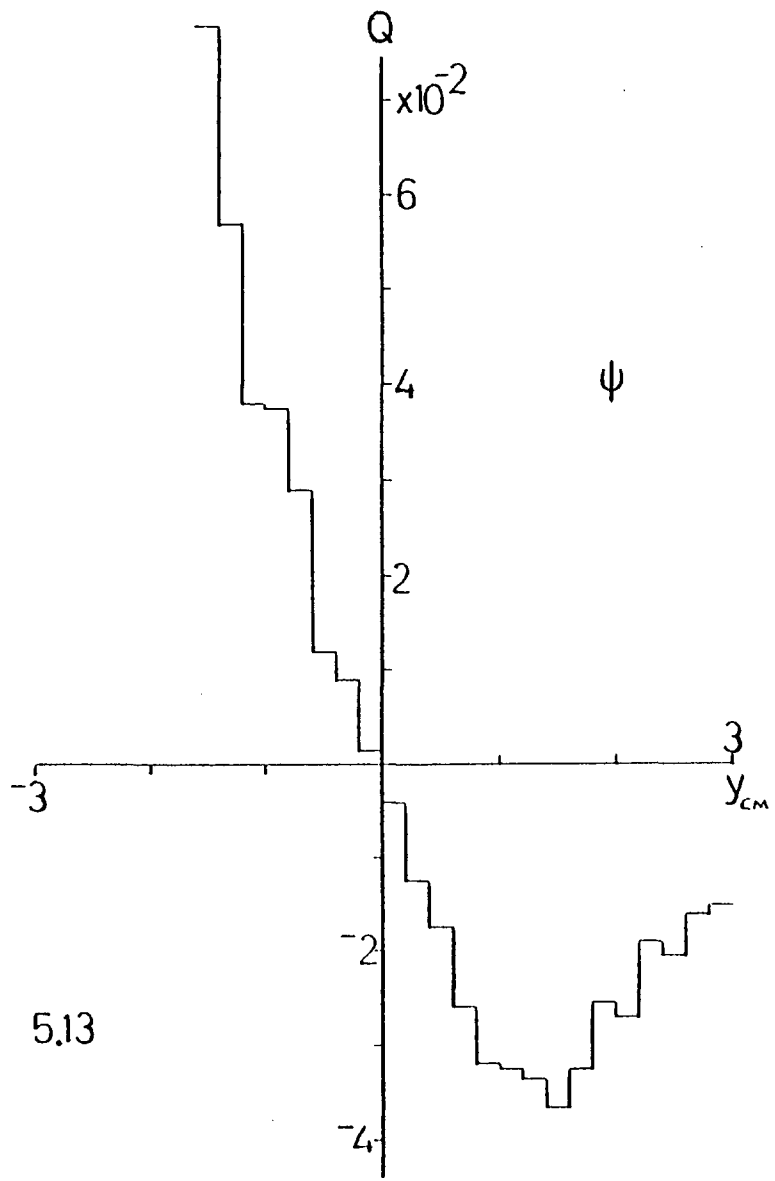

5.13

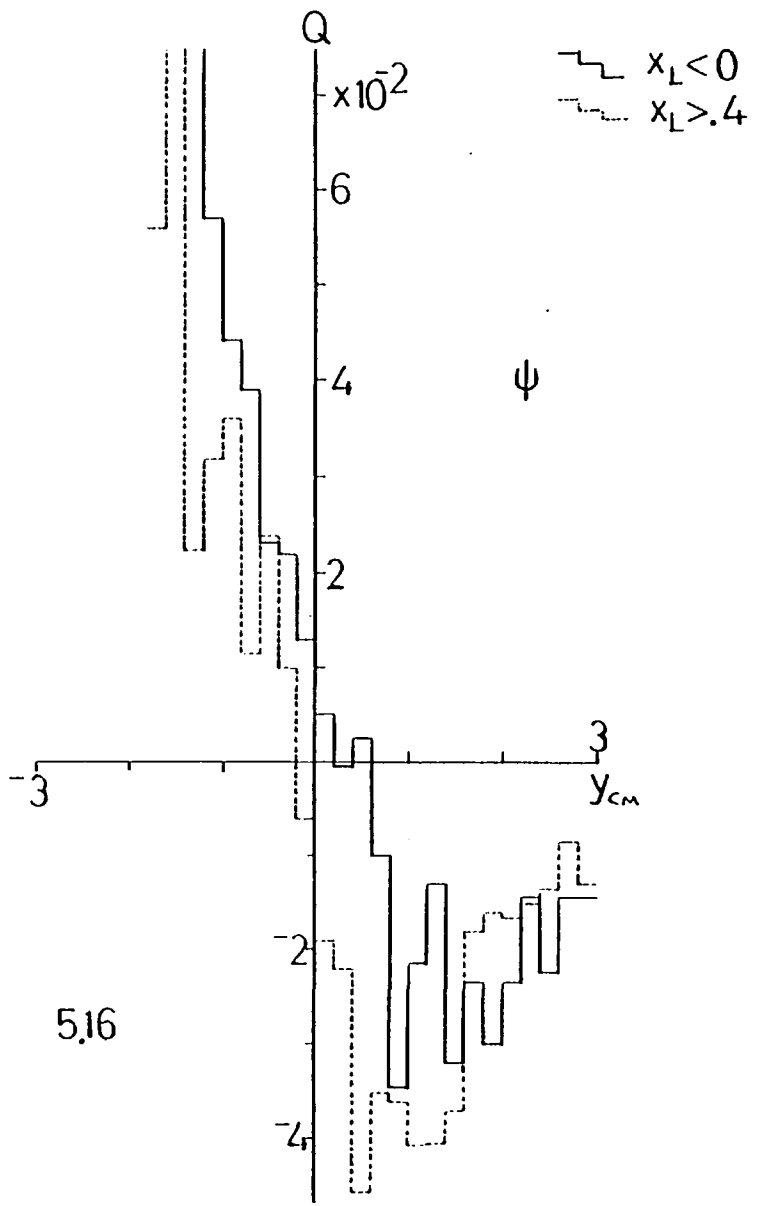

5.16

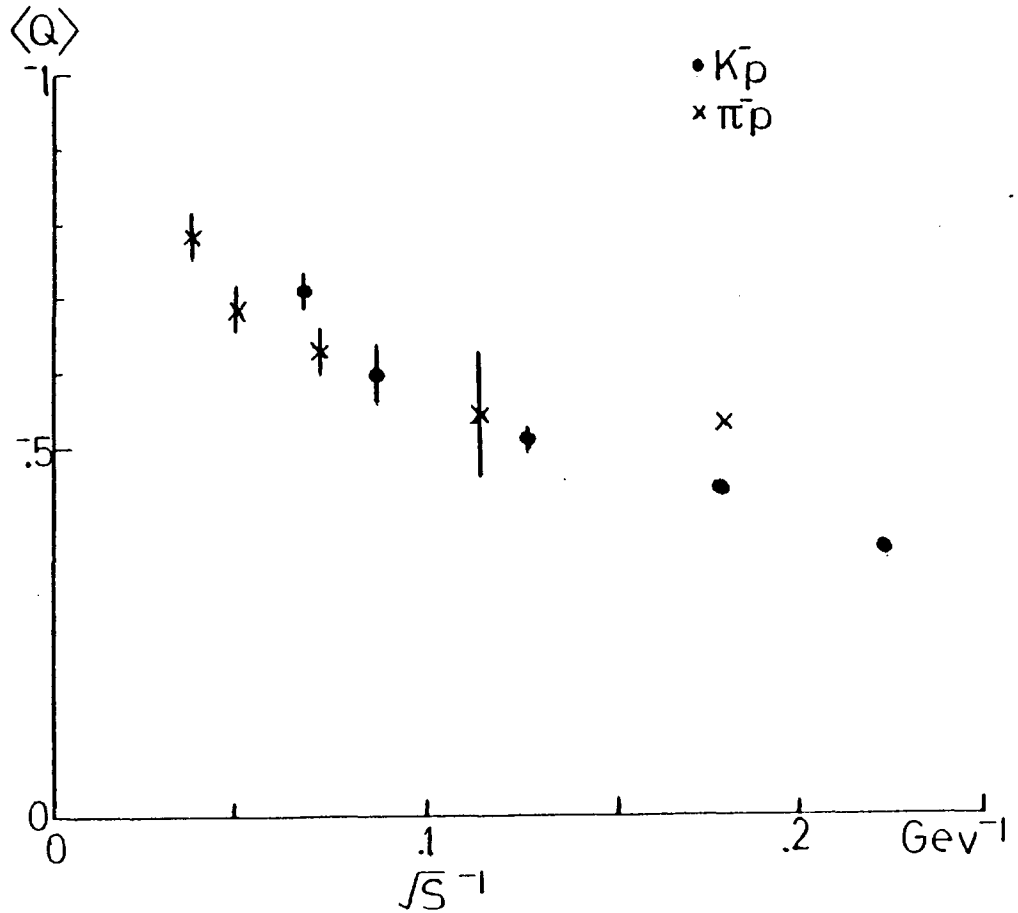

5.14

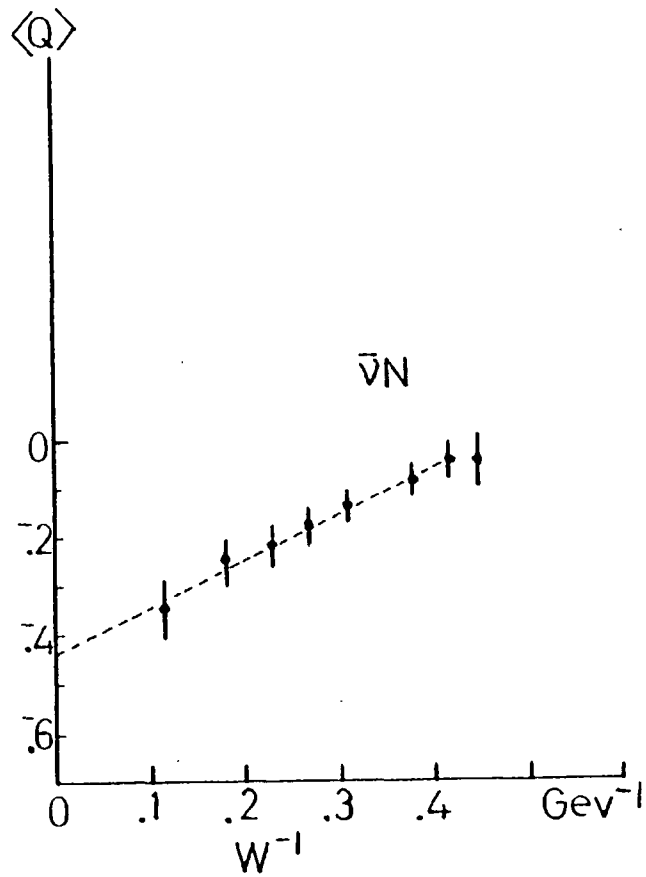

5.15

V-ZERO INVARIANT MASS SPECTRA,
UNDER VARIOUS HYPOTHESES.

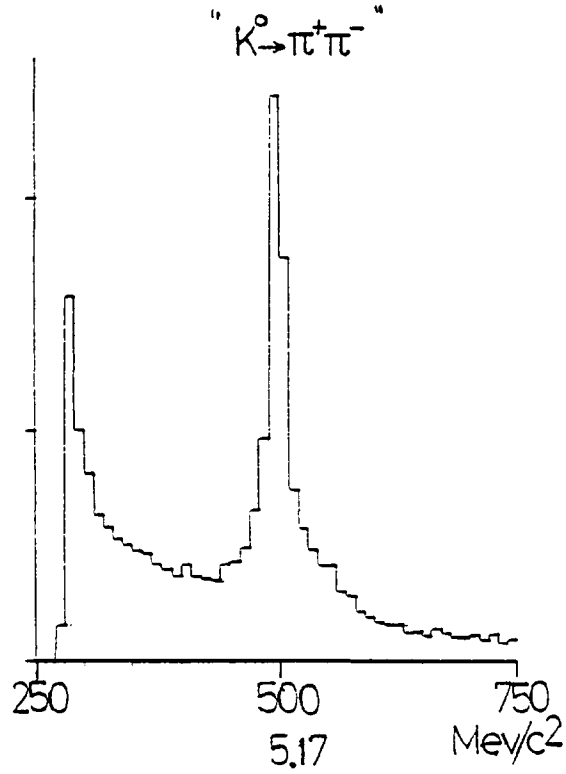

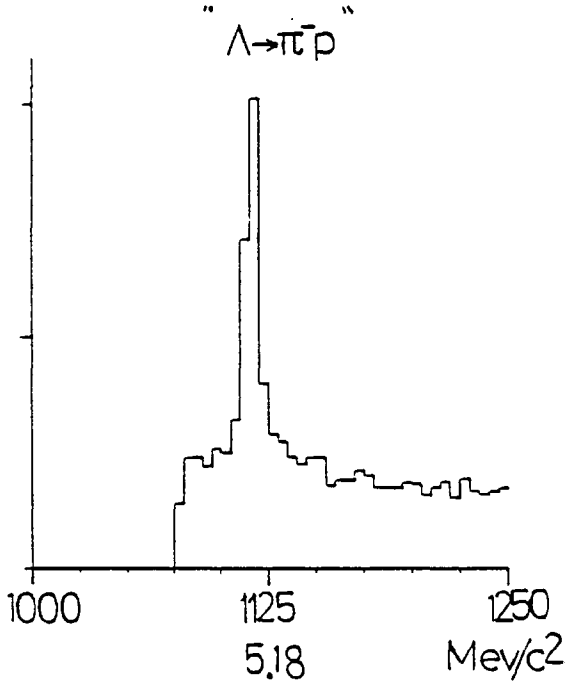

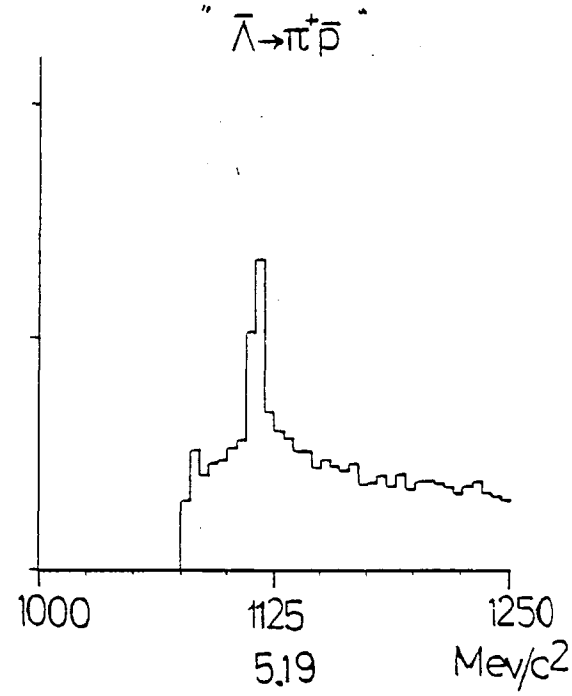

CHAPTER 6

EVENT STRUCTURE

6.0 INTRODUCTION

In this chapter, the structure of the events is studied with reference to the transverse momentum of the muon pairs, in order to investigate the origin of this transverse momentum.

6.1 PRELIMINARIES

6.1.1 Data Sample

For this analysis, the data sample is the same as that of chapter 5; that is, those events with just one pair of well measured muons of opposite sign plus associated hadrons. However, the data are now studied with reference to the transverse momentum of the muon pairs. The number of such events in various transverse momentum regions between 0 and 4 GeV/c is given in table 6.1 for the ψ and continuum data separately.

6.1.2 What to Look For

The general features of the parton models for the production of a muon pair with small transverse momentum p_T are illustrated in fig 6.1, and the resulting event structure is illustrated in fig 6.2. The configuration of the beam and target fragments around the beam axis should be similar to that in the bulk of ordinary high energy hadron collisions, and have a similar average value of transverse momentum with respect to this axis; that is, $\langle q_T \rangle \simeq 350$ MeV/c. For the production

of a muon pair with large p_T, contributions to this p_T may come from the intrinsic k_T of the partons, or the recoil of a parton produced in the subprocess. In both cases, the p_T of the muon pair must be balanced by the other final state particles.

The general features of the former case are illustrated in fig 6.3, and the resulting event structure is illustrated in fig 6.4. The p_T is thus balanced by the beam and target spectator partons, and later by their fragments. The configuration of the beam and target fragments in these events should now reflect the larger values of k_T required.

The general features of the latter case are illustrated in fig 6.5, and the resulting event structure is illustrated in fig 6.6. The p_T is thus balanced by the recoil parton, and later by its fragments. The configuration of beam and target fragments should now be similar to that in the small p_T case. However, there are now the fragments of the recoil parton. These fragments should have a configuration similar to that observed in other processes for "jets" from the fragmentation of partons; that is, have a limited transverse momentum with respect to the recoil parton direction.

The above illustrations and discussion are rather simplified. In fact, both sources of p_T may contribute in a particular event, and their effects overlap. Also, there is always the problem of identifying which particles belong to each of the fragmenting systems. It is already known that slow beam and target fragments overlap (section 5.4.1), and these probably also overlap with any slow recoil parton fragments.

The structure of the events (that is, the number and configuration of hadrons with respect to the various axes), is now studied in the context of the above illustrations and discussion.

6.2 MULTIPLICITY

In chapter 5, where all transverse momenta for the muon pairs were considered together, it was seen that the various multiplicities are well explained simply by the amount of energy $\sqrt{s}_{HAD}$ available for the production of hadrons. The expression for s_{HAD} (equation 5.4) contains a p_T dependence, such that the larger the value of p_T the smaller the value of s_{HAD}. For the ψ and continuum monte-carlos, the average multiplicity $\langle n \rangle_{TOTAL}$ falls slightly as p_T increases, as expected since s_{HAD} decreases. In figs 6.7, 6.8, $\langle n \rangle_{TOTAL}$ is shown as a function of p_T for the ψ and continuum data, and it is seen to rise, similarly in each case, as p_T increases. The expression for s_{HAD} also contains x_L, m, s dependences, and the variation of $\langle n \rangle_{TOTAL}$ with each of these variables separately is as expected just from the variation of s_{HAD} with that variable.

Thus, an interesting feature of the production of a muon pair with a larger p_T is that, despite the smaller amount of energy remaining, it is accompanied by a rise in the multiplicity.

6.3 TRANSVERSE MOMENTUM PLANE

In this section, the event structure is studied in the transverse momentum plane, whose normal is the beam axis. In this plane, it is the transverse structure of the event which is emphasised, rather than the forward/backward structure discussed in chapter 5. A hadron is described by its azimuthal angle ϕ around the beam axis with respect to the muon pair, and its transverse momentum q_T with respect to the beam axis. These variables are illustrated in fig 6.9. "Same"("away")-side hadrons are then defined to be those with values of $|\phi|$ between

0° and 90° (90° and 180°), as illustrated in fig 6.9. (These definitions of same/away-side hadrons are thus independent of the longitudinal momentum x_L of the muon pair).

Suppose all the associated final state particles were detected and their momenta measured exactly, then the sum of their transverse momenta $\underline{Q}_T = \Sigma \underline{q}_T$, would be equal and opposite to the muon pair $\underline{p}_T$ (to conserve four-momentum). If $\underline{\Phi}$ is the azimuthal angle around the beam axis of $\underline{Q}_T$ with respect to $\underline{p}_T$, then in this ideal case, $|\underline{\Phi}| = 180^{\circ}$. The observed $\underline{\Phi}$-distribution is shown in fig 6.10 for the ψ data with p_T between 2 and 4 GeV/c. It can be seen that the balance between $\underline{Q}_T$ (for those final state particles which are observed) and $\underline{p}_T$ is reasonably good.

The ϕ-distribution for the hadrons (normalised by dividing by the total number of events) is shown in figs 6.11, 6.12 for the ψ and continuum data, for each of the various p_T regions. For the lowest p_T region ($p_T < 0.5$ GeV/c), the ϕ-distributions are almost flat as expected, (and as illustrated in fig 6.2). As the p_T increases, however, the number of hadrons on the same-side falls slightly, while the number on the away-side rises, and peaks towards $|\phi| = 180^{\circ}$; that is, directly opposite the muon pair. These general features are similar for the ψ and continuum data. In section 6.2 it was seen that $\langle n \rangle_{TOTAL}$ for the data rises as p_T increases; it can now be seen that this rise is a result of the rise on the away-side being larger than the fall on the same-side. A similar effect was found in the associated charged particle multiplicities for high p_T (3-8 GeV/c) π° and γ events, measured at the CERN ISR [6.1]. The multiplicity on the same-side was found to be roughly constant, while that on the away-side rises as the p_T of the trigger increases. For the ψ and continuum monte-carlos, there is a similar fall on the same-side but a smaller rise on the

away-side; this results in the observed slight fall in $\langle n \rangle_{TOTAL}$ as p_T increases.

$\langle q_T \rangle$ as a function of $|\phi|$ is shown in figs 6.13, 6.14 for the ψ and continuum hadrons, for each of the various p_T regions. For the lowest p_T region, the distributions are almost flat with $\langle q_T \rangle \simeq 360$ MeV/c, as expected (and as illustrated in fig 6.2). As the p_T increases however, the $\langle q_T \rangle$ on the same-side stays roughly constant, while on the away-side it increases and peaks directly opposite the muon pair, with a value $\langle q_T \rangle \simeq 500$ MeV/c. These general features are similar for the ψ and continuum data. (The value $\langle q_T \rangle \simeq$ 385 MeV/c given in section 5.3.2 is an average over all the various p_T regions and ϕ values).

Thus, as the p_T of the muon pair increases, it is balanced by a rise in the number of hadrons on the away-side and also by an increase in the average transverse momentum of these away-side hadrons.

6.4 HADRON CONFIGURATION

In this section, the three-dimensional structure of the events in the πN CM frame is studied to see whether, in the larger p_T events, it resembles either of figs 6.4 or 6.6; in particular to see whether there is any evidence of a jet of hadrons opposite the muon pair. If the p_T of the muon pair is balanced by such a jet of hadrons, this jet and the muon pair will be roughly back-to-back; (they are back-to-back in the parton-parton CM frame). Thus, events are selected in which the muon pair is within 30^o of perpendicular to the beam axis, so that the separation between any recoil parton fragments and beam/target fragments is improved, (this separation is optimal for the muon pair

at 90° to the beam axis as illustrated in fig 6.6). Then, events are selected in which n_{AWAY}, which is the number of away-side hadrons with transverse momentum $q_T > q_T^{CUT}$, is ≥ 2. This q_T cut removes smaller transverse momentum beam/target fragments (and any slow recoil parton fragments) emphasising the difference between the configurations illustrated in figs 6.4, 6.6. The values of q_T^{CUT} used are : 360 MeV/c (the average value of q_T in the low p_T events), 500 MeV/c (the average value of q_T opposite the muon pair in the larger p_T events).

Do the larger q_T hadrons, remaining after the q_T cut, resemble a jet opposite the muon pair? To help answer this question, the momenta of these larger q_T hadrons are summed, and their resultant used to define a "hadron axis". Then, the average momentum of these hadrons parallel ($< q >_{DOT}$) and perpendicular ($< q >_{CROSS}$) to the hadron axis is measured.

The values of $<n>_{AWAY}$, $<q>_{DOT}$, $<q>_{CROSS}$ for the ψ data with q_T^{CUT} = 360 MeV/c, are given in table 6.2. (The values are similar for the continuum data, but the statistics are rather poor). The value of $<q>_{DOT}$ increases with p_T, reflecting the increase in $<q_T>$ with p_T; while $<q>_{CROSS}$ increases slightly with p_T, with values > 500 MeV/c. The average (half) opening angle of the hadrons with respect to the hadron axis is estimated from these values of $<q>_{DOT}$, $<q>_{CROSS}$ to be $\simeq 40^{\circ}$, for $2 < p_T < 4$ GeV/c.

The above values are to be compared with those measured in e^+e^-, where there is good evidence for 2-jet structure from the fragmentation of a quark-antiquark pair. The most important evidence for 2-jet structure comes from the $\sim 1 + \cos^2\theta$ angular distribution of a jet with respect to the e^+e^- annihilation axis. Of course, in this process there are no beam/target fragments to be removed. The average momentum of charged

particles is measured parallel and perpendicular to the "jet axis" (usually the "thrust" or "sphericity" axis is used). For $2 < \frac{1}{2}E_{CM}^{e^+e^-} < 4$ GeV (the appropriate energy range for comparison with $2 < p_T < 4$ GeV/c), the average values of momentum parallel and perpendicular to the jet axis are found to be ≃ 400 MeV/c increasing to ≃ 600 MeV/c, and ≃ 250 MeV/c increasing to ≃ 300 MeV/c, respectively [6.2]. The average total charged multiplicity in e^+e^- rises from ≃ 4 to ≃ 5 over this energy range. The values estimated for the average (half) opening angle in e^+e^- 2-jet events are 33^o at $\frac{1}{2}E_{CM} = 2.5$GeV, decreasing to 28^o at $\frac{1}{2}E_{CM} = 4.7$ GeV [6.2].

It seems that, for these values of p_T, the away-side hadrons are not as well collimated as the hadrons in e^+e^- 2-jet events; there is no evidence that they resemble a jet, even with the more severe $q_T^{CUT} = 500$ MeV/c. The possibility that some or all of the p_T of the muon pair is balanced by a recoil parton, which does not, however, produce an observable jet, is not excluded. Clearly, larger values of p_T would be desirable to improve the separation of any recoil parton fragments from beam/target fragments.

Values of $\langle k_T \rangle$ have recently been estimated in several hard-scattering processes. As mentioned in section 1.3.2, even with the QCD contribution to p_T, large values of $\langle k_T \rangle$ are still required to fit the lepton pair p_T data [1.12]. For example, a study of muon pair data in pN collisions at 200, 300, 400 GeV/c gave $\langle k_T \rangle$ ≃ 800 MeV/c [6.3]. Studies of the transverse momentum structure of hadrons in deep inelastic muon scattering data [6.4], and deep inelastic antineutrino scattering data [6.5] gave $\langle k_T \rangle$ ≃ 700 MeV/c and $\langle k_T \rangle$ ≃ 600 MeV/c, respectively. Thus, although the values $\langle k_T \rangle$ = 750-850 MeV/c (section 4.4), which would be required if the p_T of the muon pair were due entirely to the intrinsic k_T of the partons, are much larger than the simple estimates

(section 1.2.4), they are only slightly larger than the estimates from other hard-scattering processes.

Finally, for a few selected events containing a muon pair with $p_T > 3$ GeV/c and $n_{AWAY} = 5$ (with $q_T^{CUT} = 360$ MeV/c), the configuration (in the πN CM) of the muon pair, hadron axis and away-side hadrons is plotted. In figs 6.15-6.17 the muon pairs are from ψ decay, while in figs 6.18, 6.19 they are continuum pairs. (The X-axis is parallel to the beam, and the Z-axis is parallel to the magnetic field; that is, vertically upwards).

6.5 SUMMARY

The main results from this study of the event structure are:

(i) The production of a muon pair with larger transverse momentum p_T is accompanied by a rise in the multiplicity.

(ii) On the same-side (as the muon pair), the multiplicity falls slightly as p_T increases, and the average transverse momentum of these same-side hadrons stays roughly constant. On the away-side, the multiplicity rises faster (leading to the overall rise in the multiplicity), and the average transverse momentum of these away-side hadrons also increases, thus balancing the muon pair p_T.

(iii) There is no evidence that the larger transverse momentum away-side hadrons resemble a jet from the fragmentation of a recoil parton; although values of $p_T \gtrsim 5$ GeV/c would probably be required to see such an effect.

(iv) The hadrons accompanying ψ and the continuum muon pairs have similar features.

6.6 OUTLOOK

There are still many interesting areas of lepton pair production to be explored. For the continuum, these areas are currently centred around the departures from the basic Drell-Yan parton model, as predicted by QCD. A comparison of the Q^2-dependence of the parton PDF measured in LPP and DILS, and a study of the absolute normalisation K-factor, are required over a large kinematical range. The search for jets of hadrons balancing lepton pairs with large transverse momentum is also an interesting new area. For the case of resonance production, it is important to clarify the role of the intermediate χ states in ψ production, and then to extend the whole analysis to T production. The search for the Z^o and any bound states of new heavier quarks is clearly an exciting new area.

No single experiment will answer all the remaining questions. Rather, a patient study of the lepton pairs and associated particles in various lepton pair production experiments, and a comparison with other hard-scattering processes, will be required.

References

6.1 M.Diakonou et al., Phys. Lett. 91B (1980) 301.

6.2 Ch.Berger et al., Phys. Lett. 78B (1978) 176.

6.3 A.Ito et al., Phys. Rev. D23 (1981) 604.

6.4 J.Aubert et al., Phys. Lett. 95B (1980) 306.

6.5 J.Berge et al., FNAL 81/30-EXP.

Tables

Figures

6.1 NUMBER OF MUON PAIR PLUS ASSOCIATED HADRON EVENTS IN VARIOUS p_T REGIONS.

p_T REGION GeV/c	NUMBER OF EVENTS ψ	CONTINUUM
0.- .5	10 639	354
.5- 1.	15 943	707
1.- 2.	12 140	726
2.- 3.	1 334	103
3.- 4.	86	23
TOTAL	40 142	1 913

6.2 VALUES OF $\langle n \rangle_{AWAY}$, $\langle q \rangle_{DOT}$, $\langle q \rangle_{CROSS}$.

p_T REGION GeV/c	$\langle n \rangle_{AWAY}$	$\langle q \rangle_{DOT}$ MeV/c	$\langle q \rangle_{CROSS}$ MeV/c
0.- .5	2.78	576	505
.5- 1.	2.88	576	511
1.- 2.	3.03	613	538
2.- 4.	3.16	631	533

(q_T^{CUT}=360 MeV/c)

PARTON MODEL

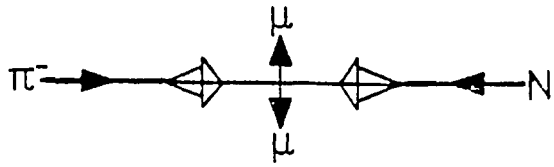

6.1

EVENT STRUCTURE

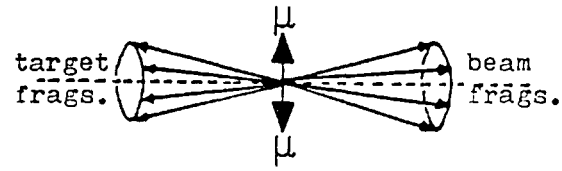

6.2

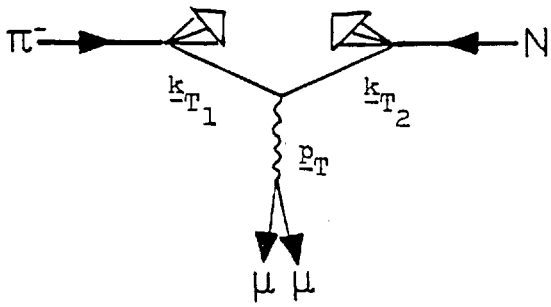

6.3

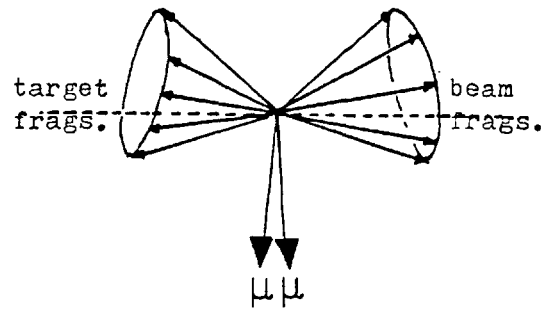

6.4

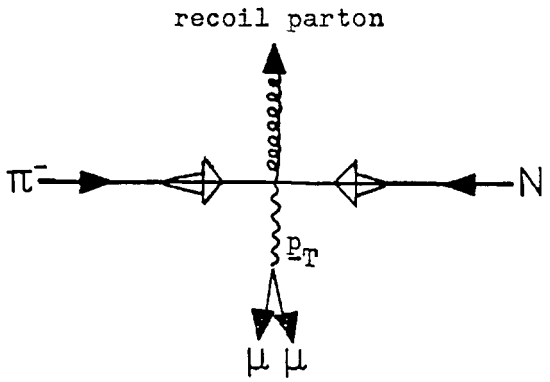

6.5

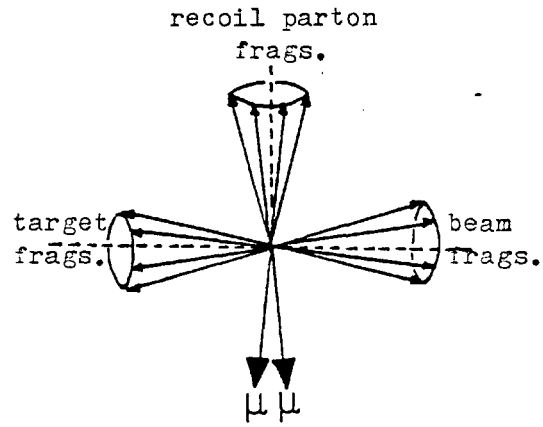

6.6

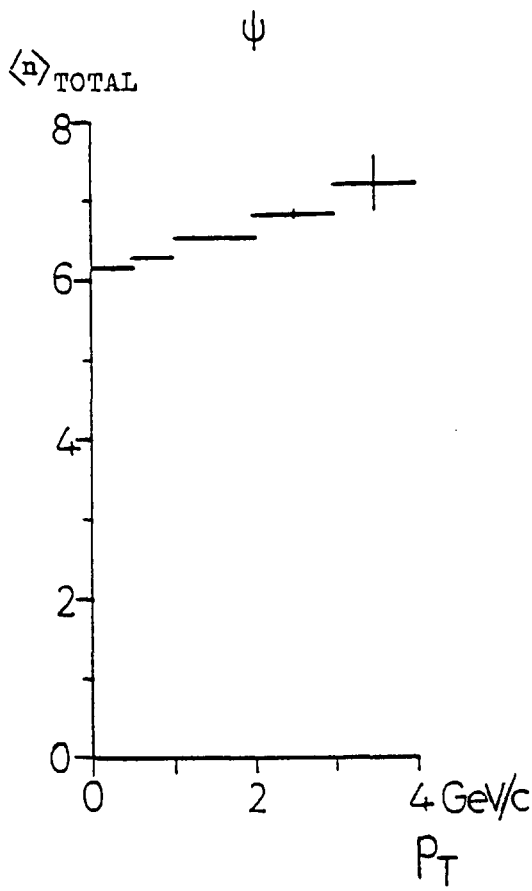
ψ
⟨n⟩TOTAL
8
6
4
2
0
0
2
4 GeV/c
PT

6.7

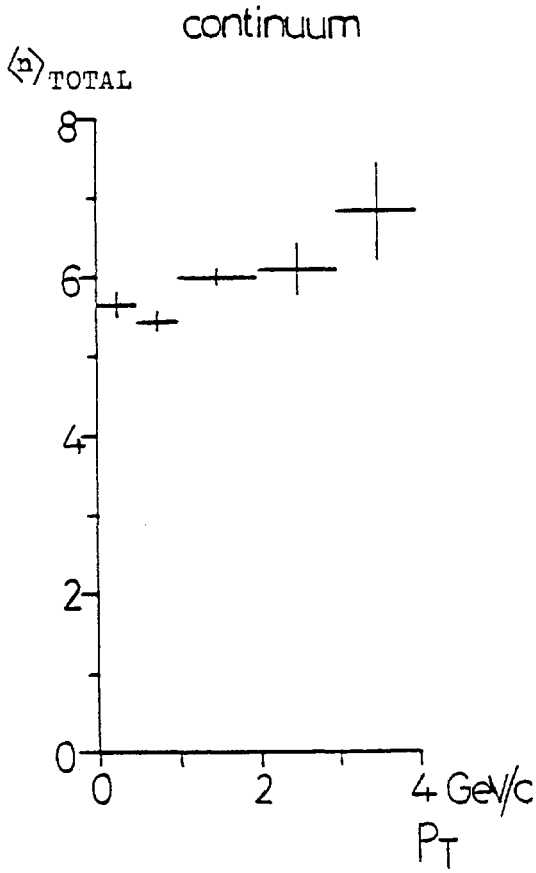
continuum
⟨n⟩TOTAL
8
6
4
2
0
0
2
4 GeV/c
PT

6.8

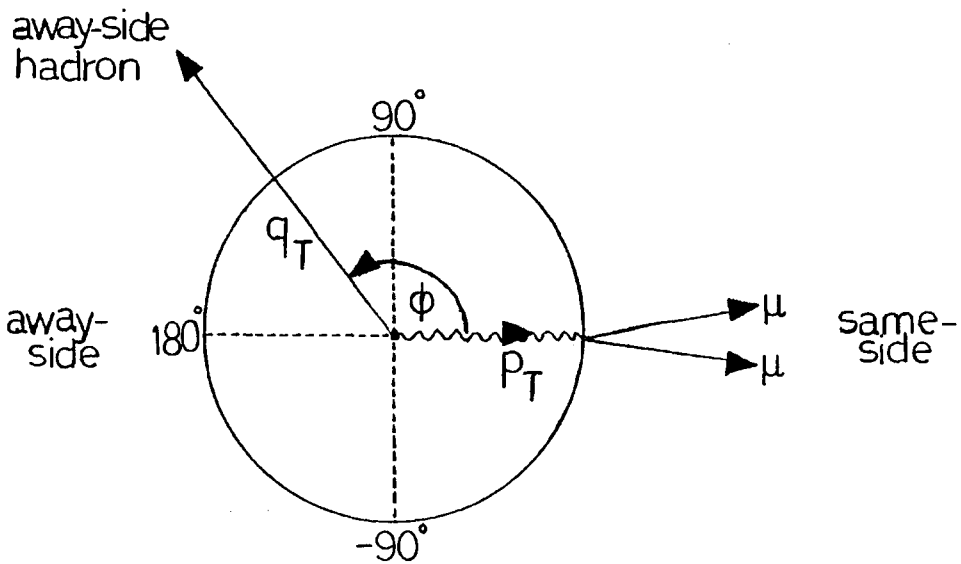

6.9 Transverse Momentum Plane.

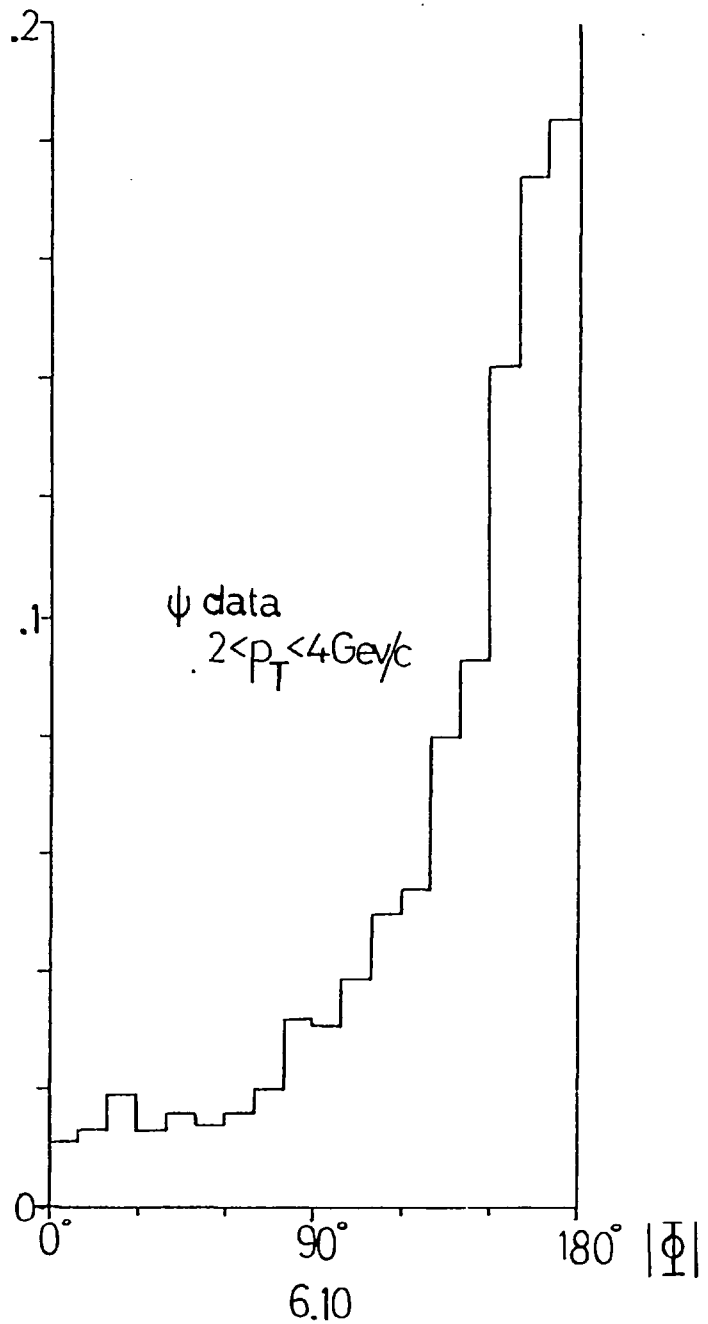

6.10

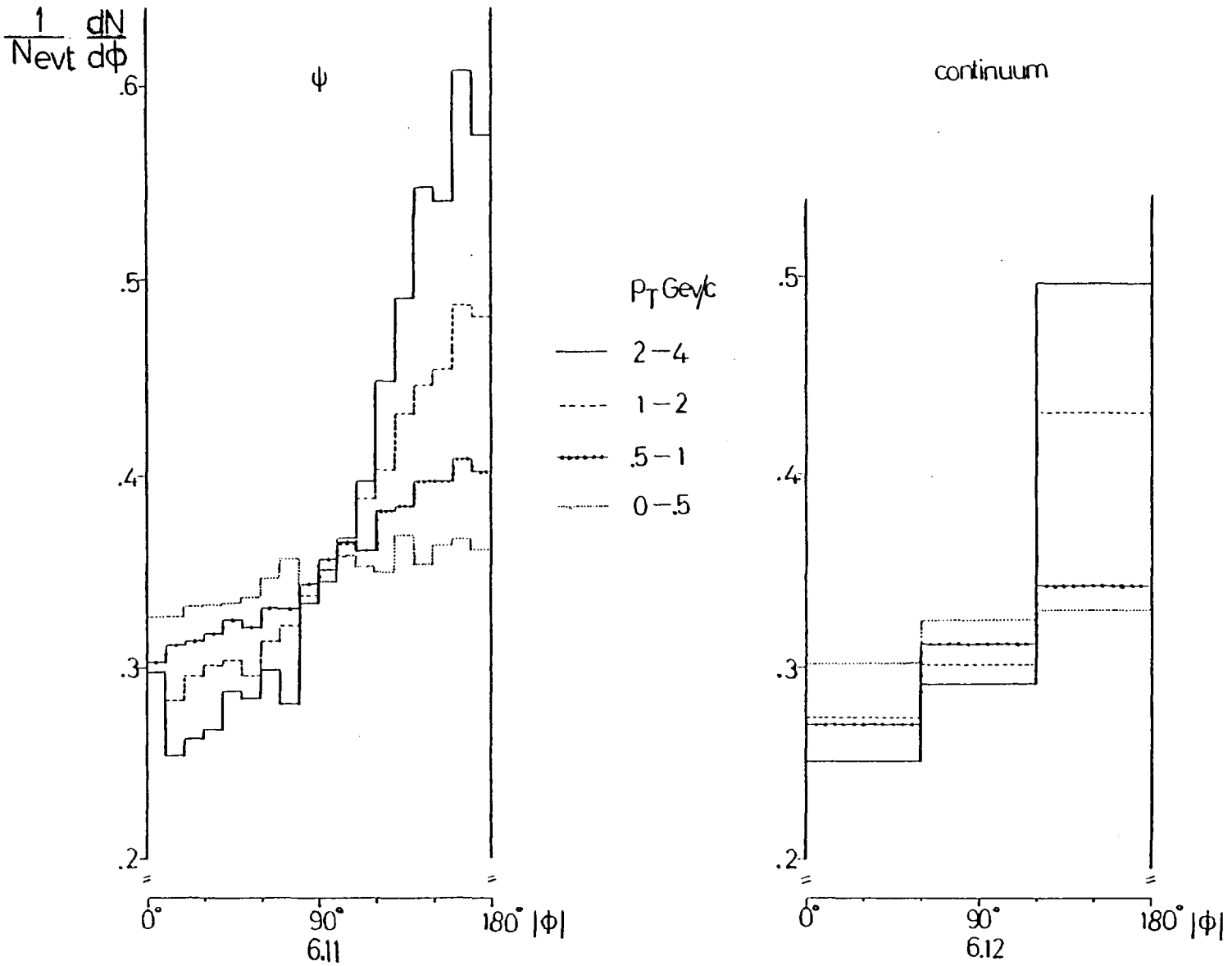
1/Nevt dN/dφ
ψ
.6
.5
.4
.3
.2
0°
90°
180° |φ|
P_T Gev/c
2−4
1−2
.5−1
0−.5
continuum
.5
.4
.3
.2
0°
90°
180° |φ|

6.11

6.12

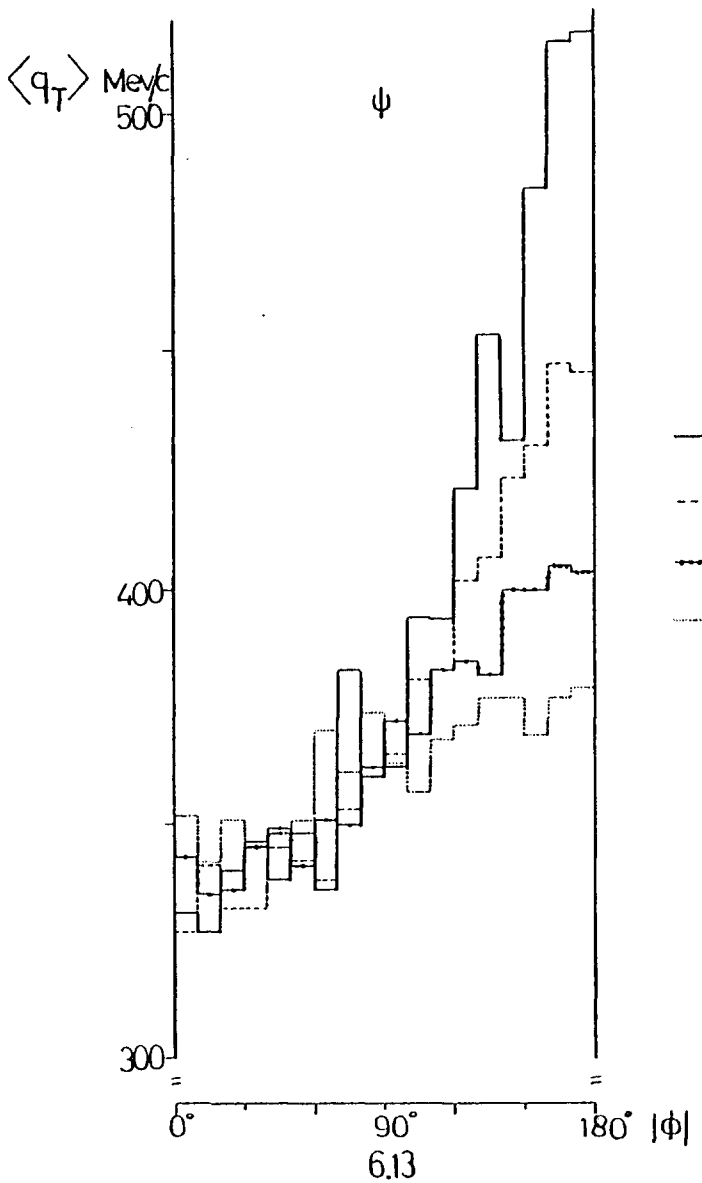
⟨qT⟩ Mev/c
500
400
300
ψ
PT Gev/c
2–4
1–2
.5–1
0–.5
0°
90°
180° |φ|

6.13

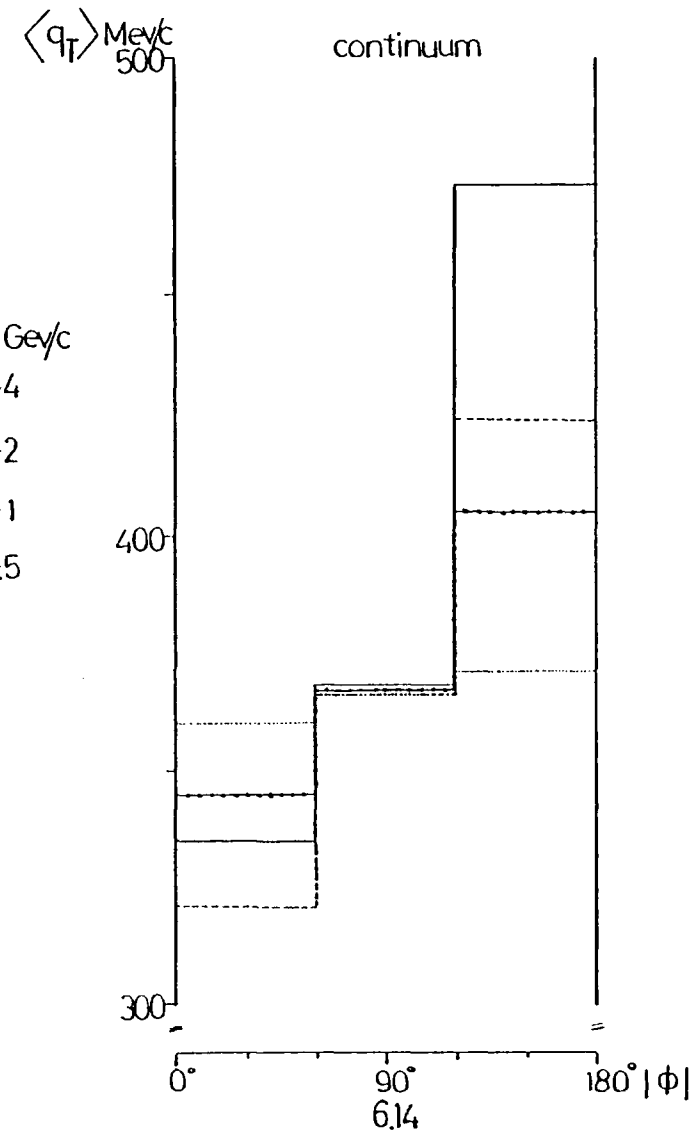
⟨qT⟩ Mev/c
500
400
300
continuum
0°
90°
180° |φ|

6.14

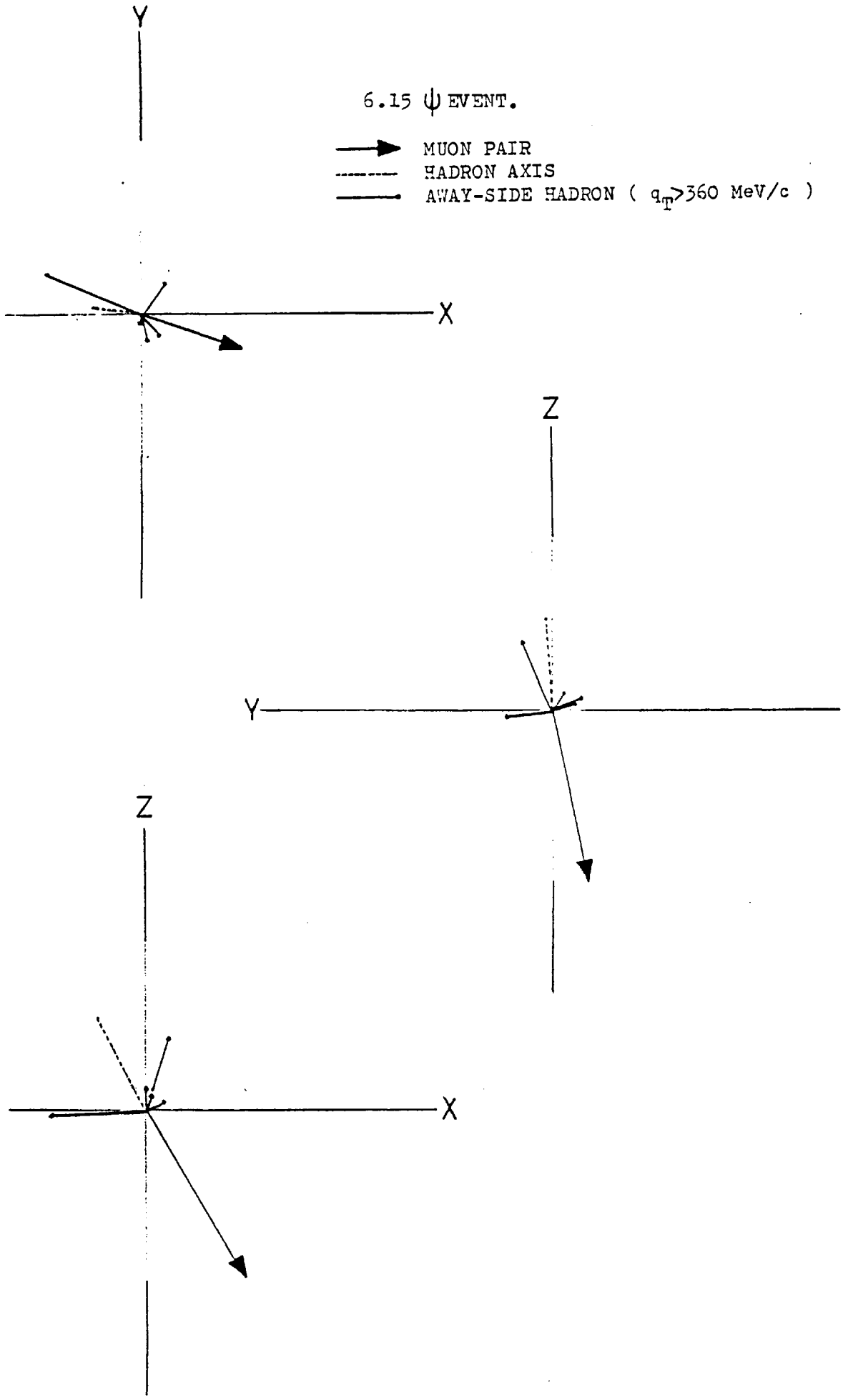

6.15 ψ EVENT.

MUON PAIR
HADRON AXIS
AWAY-SIDE HADRON (q_T>360 MeV/c)

6.16 ψ EVENT.

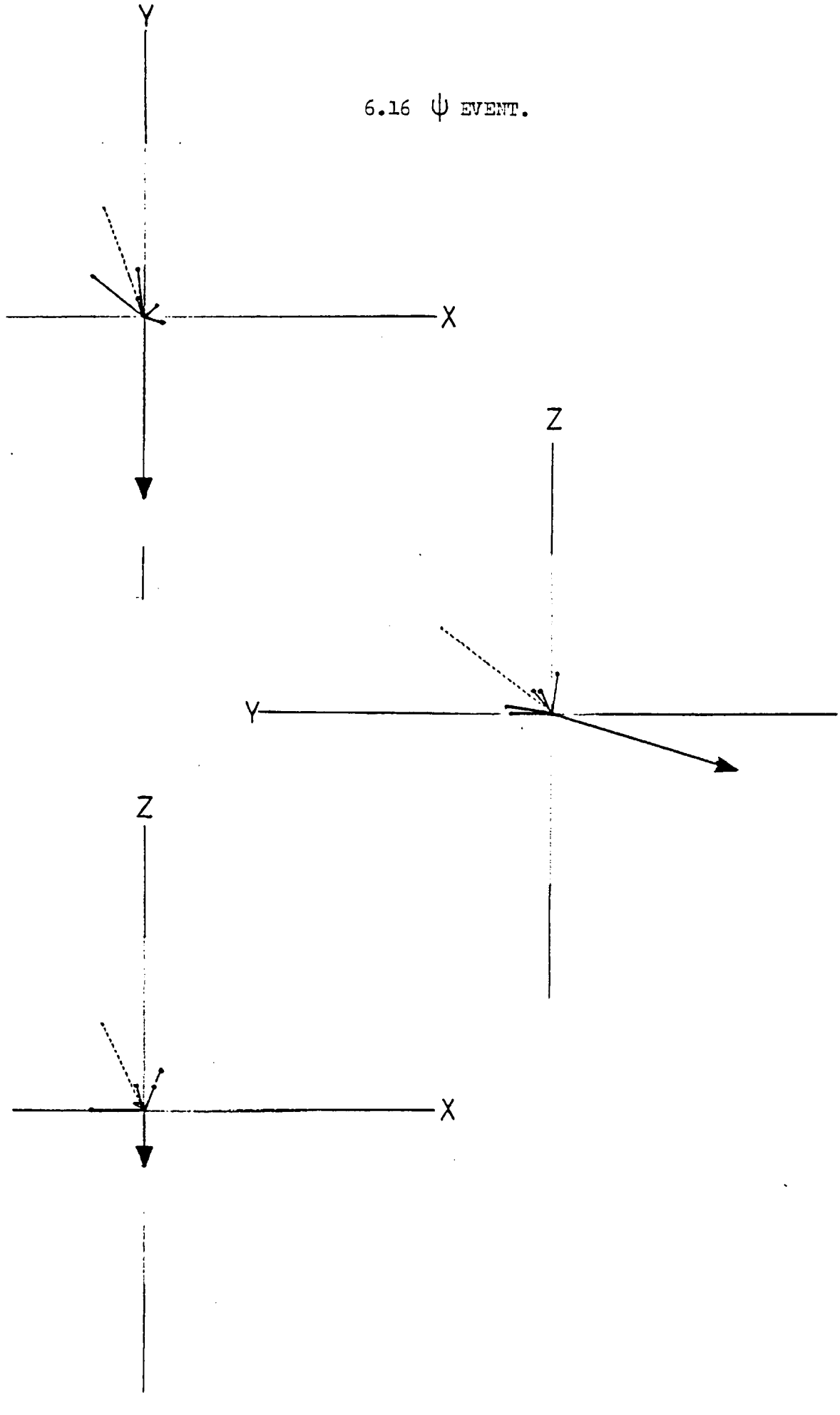

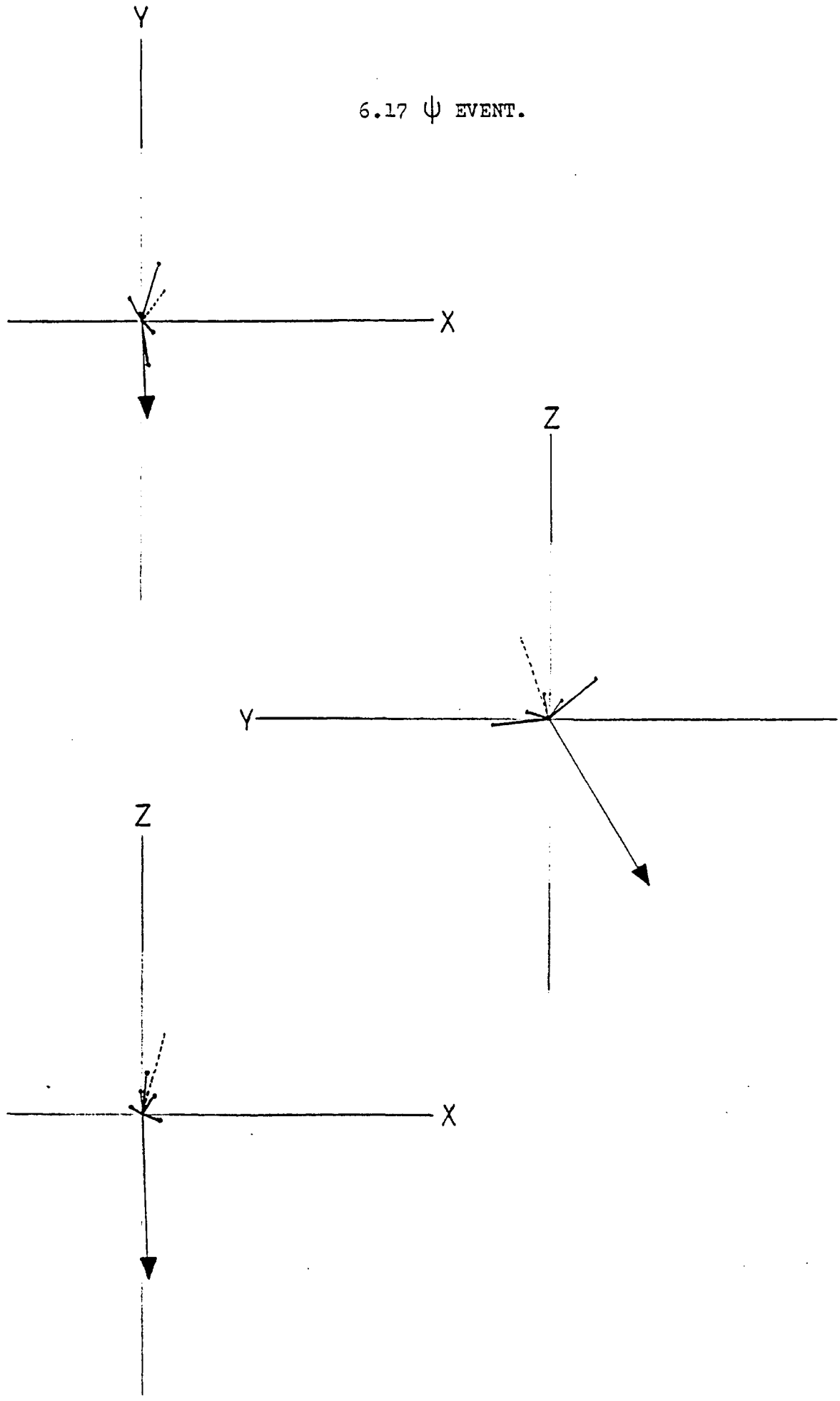

6.17 ψ EVENT.

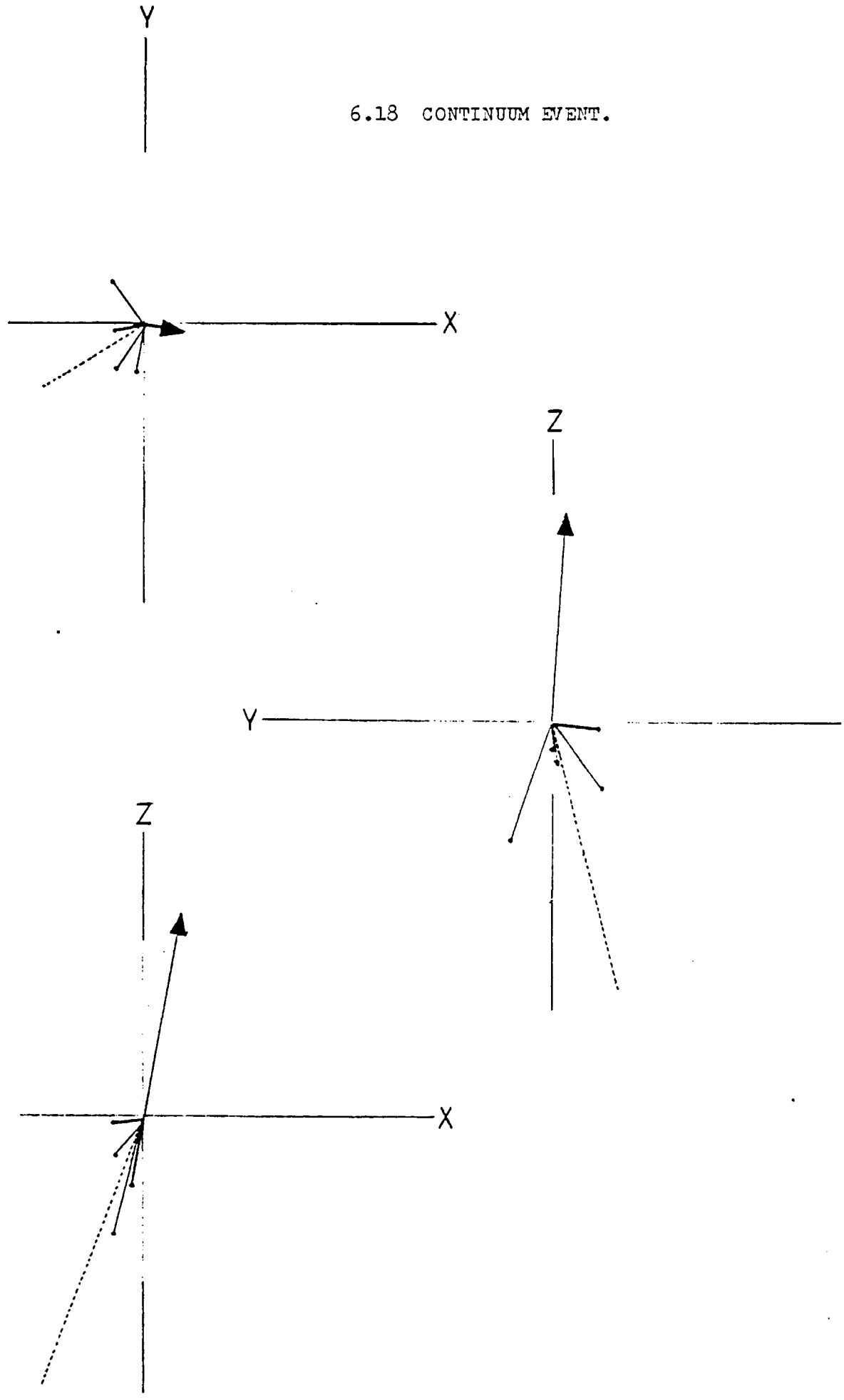

6.18 CONTINUUM EVENT.

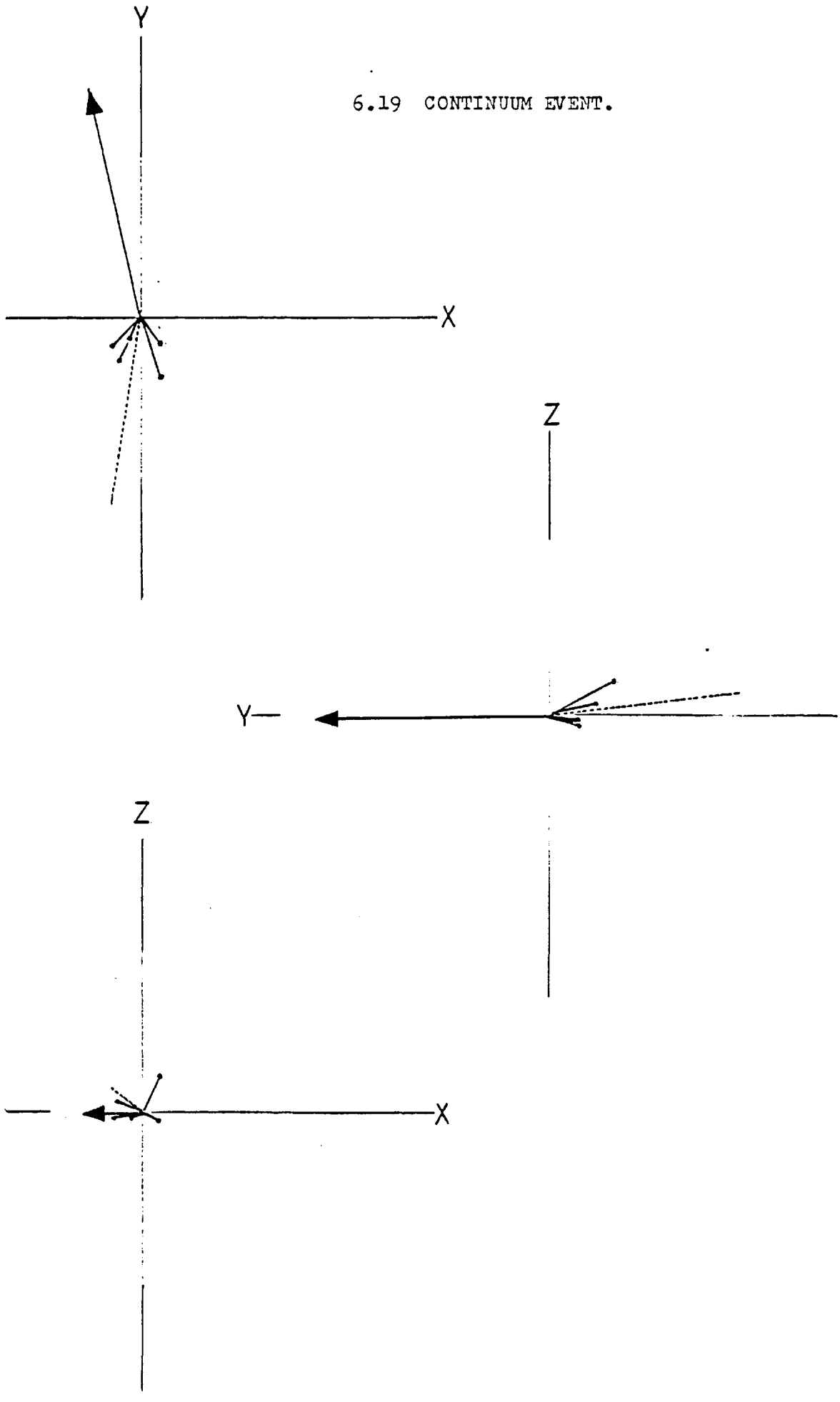

6.19 CONTINUUM EVENT.

Acknowledgements

I would like to thank the following people for their help during my period of research:

My family and Jill for support and encouragement.

D.Websdale, my supervisor, for guidance and advice throughout my work.

All members of the WA11 collaboration, especially R.Barate, B.Pietrzyk, G.McEwen, and also W.Cameron,for assistance during the production of my thesis.

Professor I.Butterworth for the opportunity of working in the High Energy Nuclear Physics group at Imperial College.

The Science Research Council for financial support.

J.Coghill for typing my thesis.